DISS. ETH NO. 21613

Towards the treatment of moving targets with scanned proton beams: Experimental verification of motion mitigation techniques with Gantry 2 at PSI

A dissertation submitted to

ETH ZURICH

for the degree of

DOCTOR OF SCIENCES

presented by

ANDREAS SCHÄTTI

born on June 22, 1986

citizen of Dürnten (ZH)

accepted on the recommendation of

Prof Dr Antony Lomax (examiner)

Prof Dr Klaus Kirch (co-examiner)

Dr Christian Graeff (co-examiner)

2013

Abstract

Many cancer patients receive radiotherapy at some stage of treatment. In radiotherapy, the patient is irradiated with high-energy X-ray radiation. In the past few years, proton therapy has gained in popularity, as it is in principle able to cause the same damage to tumours as with X-ray radiation, while reducing damage to the surrounding healthy tissue. While many of the recently established proton therapy centres are equipped with the technology for providing modern, scanned proton therapy, treatment sites are still restricted to tumours with small or no motion during treatment, such as tumours in the brain, skull base and spine. Several methods have been proposed to allow treatment of mobile tumours. Extensive simulations have been run with the general conclusion that such treatments are possible. Less work has been done on the question whether these conclusions are reflected in experiments. The aim of this thesis is to provide answers to this question.

Two motion mitigation methods have been studied: *re-scanning* and *gating*. In re-scanning, motion effects are averaged by applying a treatment plan several times per fraction. The idea of gating is to suspend treatment if the tumour is too much out of its planned position. Both methods have been investigated in a homogeneous phantom. Variations in the dose distributions due to changes in the range of the proton beam are thus not incorporated.

In *discrete* scanning, dose delivery is paused while re-positioning the proton beam on a discrete grid of dose delivery positions (*spots*). By choosing the right re-scanning method, motion of up to 1 cm peak-to-peak amplitude could be mitigated. For this purpose, a scanning system with fast energy modulation is required. The performance of gating depended not only on the amplitude of the residual motion but also on the target volume and the motion trajectory. Gating was only an effective technique to alleviate motion effects for a spherical target and regular motion. However, by combining gating and re-scanning, homogeneous dose distributions could be achieved.

Since re-scanning and gating increase treatment time, a faster scanning technique, *continuous* scanning, has been investigated as well. The beam is switched off only for energy changes. It could be shown that this method delivers dose distributions comparable to discrete spot scanning. Motion mitigation by re-scanning was at least as effective as with discrete spot scanning and did not depend on the target volume.

Continuous line scanning was employed to mimic passive scattering proton therapy with a scanning system. To this end, highly re-scanned plans were applied with a collimator and compensator. Motion of up to 1 cm could be alleviated. The intent of this approach is to offer both this *simulated scattering* and scanning proton therapy with a single system. Benefits include less neutron contamination and better conformity of the dose distributions.

Zusammenfassung

Viele Krebspatienten erhalten Strahlentherapie als Teil ihrer Behandlung. Dabei wird oft hochenergetische Röntgenstrahlung eingesetzt. Die Protonentherapie hat in letzter Zeit viel an Popularität gewonnen, weil sie im Prinzip das gesunde Gewebe besser schont, während die Tumore so gut bekämpft werden können wie mit Röntgenstrahlung.

Viele der neuen Zentren für Protonentherapie sind mit moderner Technologie für gescannte Protonentherapie ausgerüstet, doch werden vor allem die traditionellen Indikationen mit wenig oder keiner Bewegung wie Gehirn, Schädelbasis oder Wirbelsäule behandelt.

Mehrere Methoden sind vorgeschlagen worden, um auch bewegliche Tumore zu bestrahlen. Umfangreiche Simulationen haben ergeben, dass dies tatsächlich möglich sei. Die Frage, ob dieser Schluss auch experimentell bestätigt werden kann, wurde noch nicht umfassend beantwortet. Die vorliegende Arbeit versucht, Antworten auf diese Frage zu geben.

Zwei Methoden zur Verringerung der Bewegungseffekte, *Rescanning* und *Gating*, wurden untersucht. Bei Rescanning werden Bewegungseffekte dadurch ausgeschmiert, dass das Zielvolumen mehrmals abgescannt wird. Bei Gating wird die Bestrahlung unterbrochen, wenn sich der Tumor zu weit von der geplanten Position befindet. Beide Methoden wurden in einer homogenen Geometrie überprüft. Daher konnten die Effekte einer variierenden Reichweite der Protonen nicht berücksichtigt werden.

Bei *diskretem* Scanning wird nicht bestrahlt, während der Protonenstrahl auf dem diskreten Gitter der Strahlpositionen (*Spots*) neu positioniert wird. Mit Rescanning konnte so Bewegung von bis zu 1 cm Spitze-Spitze-Amplitude kompensiert werden. Dafür ist jedoch eine schnelle Anpassung der Energie erforderlich. Die Effektivität von Gating hängt nicht nur von der Amplitude der verbleibenden Bewegung ab, sondern auch vom Zielvolumen und der Trajektorie der Bewegung. Gating war nur für ein sphärisches Volumen und eine regelmässige Bewegung effektiv. Durch die Kombination von Gating und Rescanning konnten homogene Dosisverteilungen erreicht werden.

Da die Behandlungszeit durch Rescanning und Gating verlängert wird, wurde auch eine schnellere Scantechnik untersucht, *kontinuierliches* Scanning. Dabei wird der Strahl nur für Energiewechsel unterbrochen. Es konnte gezeigt werden, dass die resultierenden Dosisverteilungen mit diskretem Scanning vergleichbar sind. Die Kompensation von Bewegungseffekten durch Rescanning war mindestens so effektiv wie mit diskretem Scanning und hing nicht vom Zielvolumen ab.

Kontinuierliches Scanning wurde auch dazu benutzt, herkömmliche, gestreute Protonentherapie mit einem System für Scanning zu imitieren. Dafür wurde ein Bestrahlungsplan mit hohem Rescanning mit Kollimator und Kompensator appliziert. Bewegung von bis zu 1 cm konnte so kompensiert werden. Der Zweck dieses Ansatzes ist es, sowohl diese *simulierte gestreute* als auch gescannte Protonentherapie mit einem einzigen System anbieten zu können. Die Vorteile sind weniger Neutronenkontamination des Strahles und bessere Konformität der Dosisverteilungen.

Acknowledgements

First and foremost I should like to thank Eros Pedroni for his outstanding lifetime achievement. He has pushed back the frontiers of proton therapy and blazed the track of spot scanning. He has always shared his concerns, visions and immense knowledge of the field of proton therapy. Without him, I would not have got the chance to do a PhD in medical physics in such a pioneering environment and in such close proximity to home.

I am grateful to have had the possibility to work in such a great team of many world experts in their area. Thanks go to my supervisors, Tony Lomax and David Meer, I had the right guidance at the many crossroads one encounters on the road to the PhD. They were never at a loss of ideas of what to do next.

I should like to thank Silvan Zenklusen for spending many hours introducing me to his work, which was the essential springboard of this thesis.

Without Monika Žákova, measurements on long evenings and on week-ends would have been much less agreeable. I am also grateful for her guidance and participating in the essential process of bouncing around ideas.

Thanks also go to Sairos Safai, who helped me understand multiple Coulomb scattering and quenching and was always open to discussions.

Technical support granted by Hans-Ueli Stäuble, Benno Rohrer and, quite generally, PSI as a whole, was outstanding.

I was very happy being part of this research group. Students, PhDs and post-docs were very resourceful, helpful and fun. Thanks go to Antje Knopf and Francesca Albertini for the organisation of so many social events and dinners, to Gabriel Meier for sharing my enthusiasm in swimming in the Aare and the many vivid discussions about any topic at hand, and to Ye Zhang for taking part in my suffering from the climatic extrema in the famous student's container, which in the meantime has sadly and suddenly passed away.

I am most indebted to Iryna Alexandrovna Ozerianska for going with me through the ups and downs of my PhD, always encouraging, always taking care of my soul.

My most cordial thanks go to my family for supporting me in every step of my life and providing a regenerating place at the sun, aloof of the dreadful fog that generally covers PSI in autumn.

Contents

1. Introduction

Proton therapy has experienced a surge in new treatment centres [1]. It offers advantages over radiotherapy in terms of integral dose and conformity. To fully exploit these advantages, more progress is needed [2, 3]. At the end of this process, the widespread substitution of advanced radiotherapy, such as *intensity-modulated radiotherapy* (IMRT) and tomotherapy, might become reality [4]. In figure 1.1 a plan with *intensity-modulated proton therapy* (IMPT) is contrasted with three different IMRT plans. The lower integral dose of the proton plan is evident.

Charged particles heavier than protons provide even sharper beams. Due to their mass, they scatter less in material. The disadvantage of heavy ions is the increased size and cost of the beam delivery system, especially for a rotating gantry.

Many of the new proton therapy centres offer both conventional passive, scattering and modern active, scanning technologies. A major problem of scanning is the presence of organ motion which interferes with the dynamic dose delivery. At the moment, this modality is used mostly for treatment sites where there is little motion, such as the brain and the spinal chord. Several methods to limit the impact of motion on the dose distributions or to limit motion itself have been devised.

At the Centre of Proton Therapy (CPT), located at the Paul Scherrer Institute (PSI), the future motion mitigation strategy is to use re-scanning for moderate motion and combine it with gating for large motion amplitudes. In addition, we envision breath-hold together with slow tracking. One possibility to do this is to check the tumour position before irradiation in each breath-hold by taking a single X-ray image in the direction of the beam (*beam's eye view*). Alternatively, the irradiation could be triggered by a measurement of the external motion, with updates of the correlation model between internal tumour motion and external motion by X-ray imaging.

The prime aim of this thesis was the experimental validation of the short-term motion mitigation strategy of PSI, i.e., re-scanning and gating. To this end, dosimetry tools suited to this task have been developed. Different scanning and re-scanning approaches have been compared with respect to their efficiency in reducing motion effects.

In section 1.1, the basics of proton therapy physics are outlined. The different technologies of proton therapy are introduced in section 1.2, and section 1.3 covers the proton therapy project at PSI. A review on the problem of organ motion in ion therapy is given in section 2, and techniques of mitigating this problem are presented in section 3. A description of the simulation, treatment planning and measurement process follows in section 4. Section 5 reports on the results on re-scanning with discrete spot scanning. Gating and its combination with re-scanning are treated in section 6, while the results of continuous line scanning are presented in section 7. The thesis is concluded in section 8 by offering an outlook to what research could follow up on this thesis.

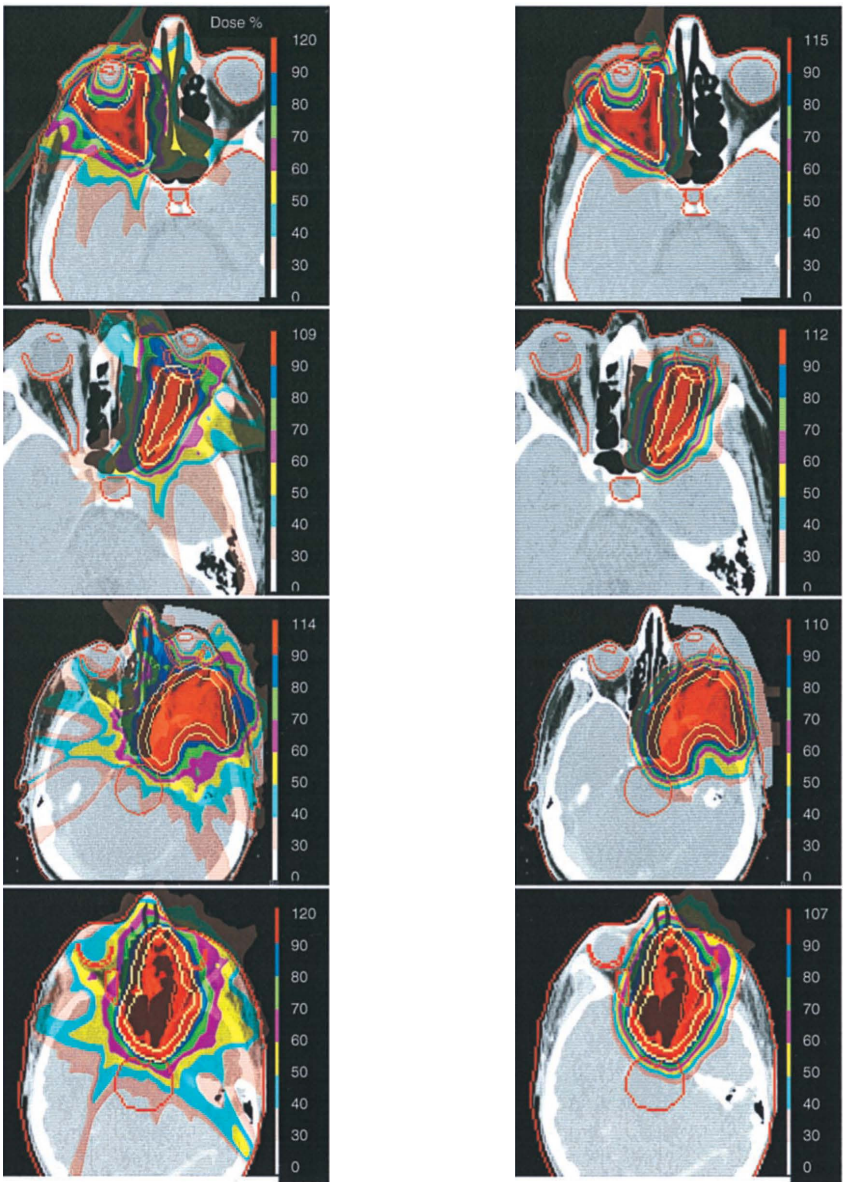

(a) (b)

Figure 1.1.: Dose distributions in the transverse plane for (a) IMRT and (b) IMPT. From top to bottom, plans for a lymphoma of the right orbit, a meningioma of the left optic nerve, a sphenoidal ridge meningioma protruding into the left orbit, and a left paraorbital pediatric rhabdomyosarcoma are compared. Image and caption courtesy of [5].

1.1. Physics of proton therapy

In radiotherapy, the goal is to transport energy into the body and deposit it in the cancerous cells to cause cell death. At the same time, part of that energy is deposited along the entry and exit path of the beam in normal tissues. Not only are many of them killed but damaged cells may also mutate instead and give rise to secondary cancer. In other words, the treatment of the primary cancer may cause secondary cancer.

When a *photon* penetrates matter, such as the human body, it has a certain probability of interacting with the medium. Most of the time, this interaction is Compton scattering. The photon transfers a certain amount of its energy to a bound electron and is deflected in the process. The number of photons in the forward direction decreases with depth and so does the deposited energy, which can be modelled as an exponential function of penetration depth. The electrons are scattered mainly in the forward direction. This means that at the entrance of the photon beam into the medium, there is a build-up of deposited energy with depth. At a certain depth of the order of some centimetres, depending on the beam energy, the maximum energy deposit is reached. At larger depths, as described above, the exponential decay of the deposited dose sets in. As a result, the radiation field extends to infinity along the beam axis. This sounds like a horrible idea to treat patients with deep-seated tumours. As a remedy, the tumour is irradiated from many different directions, so that the tumour is always irradiated but the surrounding healthy tissue is only exposed to a fraction of the energy.

The energy deposited per volume of a medium depends also on the density of the medium. In the human body, densities can be classified into those for water-like soft tissue, bone, and fully or partly gaseous volumes such as nasal cavities, intestinal gas bubbles or lung tissue.

The concept of energy is replaced by the concept of absorbed dose in radiotherapy. Absorbed dose is the energy per unit mass absorbed by a medium and measured in units named after 20th century British physicist and radio-biologist Louis Harold Gray. The units are defined as $1\,{}^{\mathrm{J}}/_{\mathrm{kg}} = 1\,\mathrm{Gy}$.

Better physical properties of dose deposition favour proton beams over photon beams for radiotherapy. In *proton* therapy, the main process of energy transfer to the medium is ionisation of atoms by Coulomb scattering. The protons lose a small amount of energy in each of the many collisions, which is transferred to the bound electron involved in the interaction. In turn, the now free electron travels a short distance and damages cell structures on its way, most importantly the DNA, or generates more free electrons by ionisation. The major part of the biological damage due to proton irradiation is due to the electrons, not the protons. In the case that the DNA is broken along each of its two strands and reparation fails, the cell most certainly will not survive the next cell division or, with a much lower probability, a mutation in the DNA will occur. For each interaction between a free electron and a molecule of the DNA there is only a single-strand break, which is repaired efficiently by the cell. Therefore, two electrons need to cause a single-strand break each to the same DNA in short succession to kill the cell. Details are explained elsewhere [6].

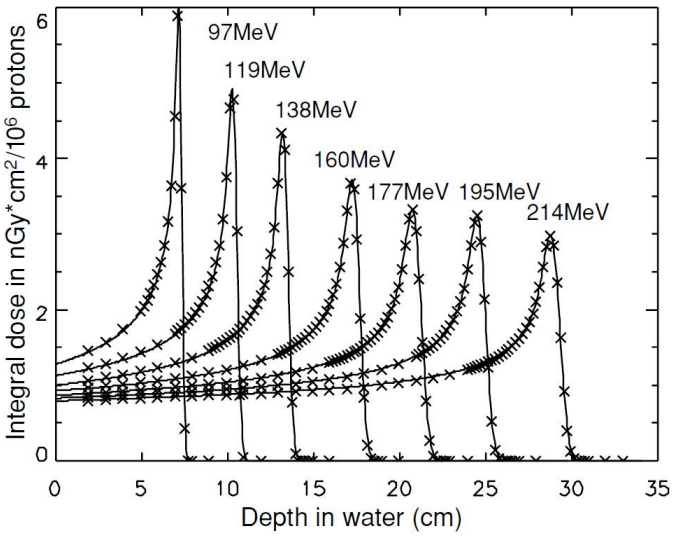

Figure 1.2.: Measured and modelled proton Bragg peaks with beam energies between 97 MeV and 214 MeV. Note the smaller plateau-peak ratio for higher energies due to range straggling. Image courtesy of [10].

The mean energy loss per distance travelled by a charged particle or, equivalently, the stopping power of the medium for this particle, is described by the Bethe equation [7]:

$$-\frac{dE}{dx} = \frac{4\pi n}{m_e v^2}\left(\frac{e^2}{4\pi\epsilon_0}\right)^2\left(\ln\left(\frac{2m_e v^2}{I\left(1-\beta^2\right)}\right)-\beta^2\right)$$

where E is the particle energy, n the electron density, m_e the electron rest mass, v the particle velocity, e the elementary charge, ϵ_0 the vacuum permittivity, I the ionisation potential or average excitation energy and $\beta = v/c$ with c the speed of light in vacuum. The stopping power is mainly a function of the particle velocity. The equation represents the experimental values quite well down to about 200 keV. The most uncertain variable is the ionisation potential. Reported values can vary considerably. Because the equation yields the mean energy loss, it is sensitive to outliers. The most probable energy loss is much lower [7]).

The bottom line of all this is that the stopping power peaks at low proton energies, at the end of their range, before they stop, i.e., are in thermodynamic equilibrium with the medium. This maximum is called the *Bragg peak*, discovered around 1904 for α particles by British physicist Sir William Henry Bragg [8]. For the centenary of this important discovery, a highly recommended history has been written about it [9]. Bragg peaks of different energies are shown in figure 1.2. Due to the depth-dose curve of protons, culminating in the Bragg peak, high dose can be deposited in the tumour by stacking proton beams of different energies and weights, while the dose outside the tumour is kept low. Far fewer beam directions are needed to achieve this goal than with photons.

The given spread of the initial proton energy and the stochastic nature of Coulomb

scattering (range or energy straggling) result in a distribution of ranges for a proton beam. The Bragg peak is in reality blurred out. Besides, what is usually plotted is not the stopping power but the absorbed dose as a function of penetration depth, integrated over the lateral plane, referred to as the depth-dose curve. As a rule of thumb, the variation in range is about 1 %. The Bragg peak itself is much lowered on the central axis due to multiple Coulomb scattering (MCS) with atomic nuclei [7]. The width of a narrow proton beam is about 2 % of the range. To this value the initial beam width has to be added in quadrature. There have been attempts to model the depth-dose curve of protons [11, 12, 13] but they could not replace the traditional approach of feeding treatment planning systems with measured or pre-calculated data [10]. Besides Coulomb scattering, protons also interact via the strong force with the atomic nuclei. In inelastic nuclear interactions, secondary protons, neutrons, α particles, deuterons and other nuclear fragments are produced. Typically, these remnants have a higher ionisation density than the primary protons, hence the *radio-biological effect* (RBE) is increased.

The RBE is defined as the biological effect relative to the one of X-rays for the same physical dose. The biological effect can be defined in various ways. Usually, survival curves of cell cultures are compared. One definition would take the absorbed dose it takes to kill half of a cell population, or a tenth, or any fraction, for that matter, relative to a ^{60}Co beam. However, the RBE varies with the fraction of killed cells chosen, because the survival curves as a function of absorbed dose are differently shaped for photons and protons. In treatment planning for proton therapy, a fixed RBE of 1.1 is usually assumed [14], irrespective of the range. Studies indicate that RBE increases at the distal edge of the physical Bragg peak, leading to a shift of the biological Bragg peak [15, 16]. On the other hand, the direct measurement of the RBE is subject to large uncertainties. Some experiments might measure the RBE *in vitro*, others *in vivo*. The choice of the type of cell is also important. A better approach is to derive a biophysical model for the RBE. For example, in the local effect model (LEM) the RBE distributions in the treatment field of heavy ions are derived from the X-ray dose distributions [17]. In this way, the vast amount of clinical data available from X-ray radiotherapy is made accessible.

As opposed to Coulomb scattering with electrons, nuclear interaction probabilities are derived from cross section measurements. Primary protons undergoing nuclear interactions are removed from the beam, so the proton fluence decreases with depth by about 1 % per cm of range. In figure 1.3, the reduction in primary proton flux due to nuclear interactions is plotted along with the dose contribution of the nuclear fragments produced in this process.

An excellent, accessible account of proton therapy physics is presented in the book *Radiation Oncology: A Physicist's-Eye View* [18].

1.2. Delivery methods

There are several methods to apply proton therapy. In the past, a treatment gantry supported just one of the methods. Only recently has it become popular to design

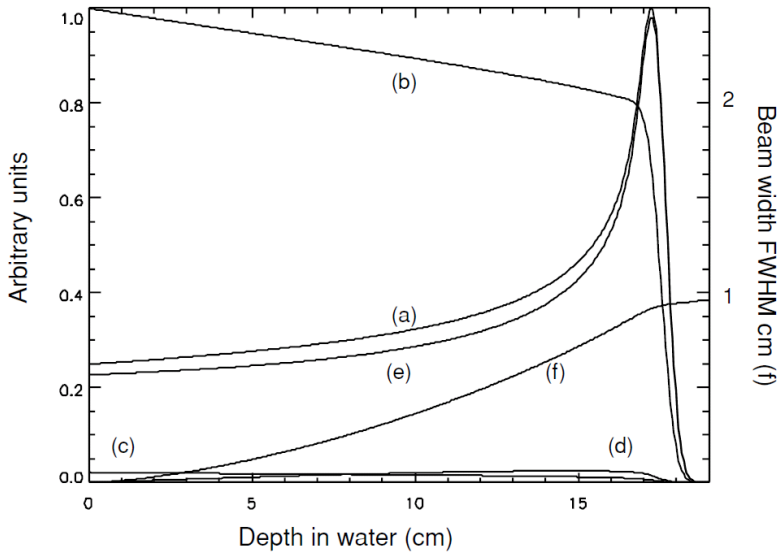

Figure 1.3.: For a beam energy of 160 MeV, several physical variables are plotted: (a) total integral depth dose, (b) primary proton flux, (c) local and (d) long-range contributions to the integral depth dose due to nuclear interactions of the primary protons, (e) integral depth dose due to primary protons and (f) Gaussian beam width. Image courtesy of [10].

gantries that can be adapted to several delivery methods. Some centres offer even a range of ion species to choose from, starting with protons and including, most prominently, carbon and helium ions. What is fixed, however, is the type of particle accelerator.

In *active, scanning* proton therapy [19, 20, 21], the dose is applied sequentially, see figure 1.4a. The sequence consists of spots, i.e., a set of lateral beam positions at a certain energy and with a certain beam weight. In other words, scanned fields are applied spot by spot. Sweeper magnets are controlled to change the spot positions, while the energy is set by varying the amount of material in the beam or by adjusting the beam energy directly in the accelerator. The beam-on time, or *dwell time* of a spot, and the beam current determine the amount of dose delivered by a spot.

By contrast, in *passive, scattering* proton therapy [22, 23] a uniform treatment field is applied to the whole target volume simultaneously until the required dose is delivered. The beam is first scattered laterally to achieve sufficient homogeneity and then aimed at a rotating modulator wheel. This wheel is made of varying thickness. Proton Bragg peaks are pulled back according to the energy lost in the modulator wheel. During a single rotation, the beam range is modulated over the full extent of the target volume. The field is constrained by a collimator to the target volume. The distal field edge is shaped to the edge of the target volume by means of a compensator, see figure 1.4a.

Wobbling or *uniform scanning* proton therapy is a hybrid of active and passive proton therapy [25, 26]. A broad beam is scanned by magnets in the lateral plane to create a uniform field. Iso-energy layers are applied one after another. The final dose distribution

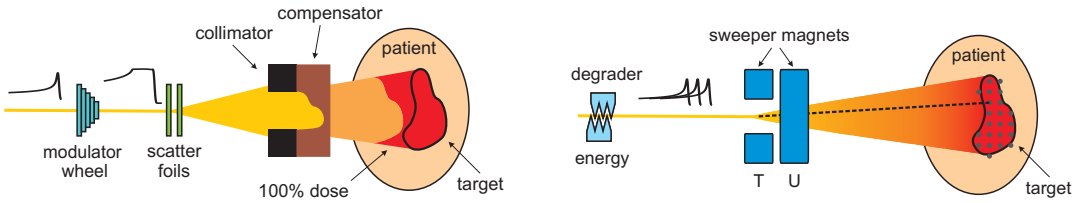

(a) passive, scattering proton therapy (b) active, scanning proton therapy

Figure 1.4.: Different approaches to the delivery of proton therapy. Scanning proton therapy is more conformal because it spares normal tissue proximal to the target. Images courtesy of [24].

has the same characteristics as in scattering. Patient-specific beam shaping devices are also necessary. It is not known yet if uniform scanning is more prone to organ motion than passive scattering. To counter interplay effect, a high rate of re-scanning is applied to each iso-energy layer and the time to change the energy is kept to a minimum [26]. The advantage over passive scattering is the better utilisation of the proton beam and less neutrons downstream of the nozzle, a larger treatment field and an increase in maximum range of up to 2.5 cm [26].

The most versatile beam shaping technology available in photon radiotherapy, the multi-leaf collimator (MLC), has also been adopted by proton therapy [27, 25, 28, 29]. Uniform fields are shaped without the need of a patient-specific collimator. Tungsten seems to be an appropriate material with acceptable levels of proton leakage and neutron dose [29, 30], but not everybody agrees [31]. There are still other open issues, such as lateral penumbra and equipment size [32]. Furthermore, patient-specific compensators are still necessary. MLCs are also an interesting option for improving the penumbra of scanned beams at low energy [33].

Several implementations of active, scanning proton therapy have been invented:

- *Discrete spot scanning*: The beam is switched on at the spot positions and blocked while advancing from one spot to the next. During this transition, no dose is applied.
- *Dynamic or continuous line scanning*: The beam is scanned continuously through the iso-energy layers. It is blocked only for changes in energy and, possibly, scanning direction. The concept of a spot is discarded.
- *Raster scanning*: The only difference to discrete spot scanning is that the beam is not blocked when moving to the next spot [20, 34]. It is a hybrid of discrete spot and continuous line scanning. The dose delivery is difficult if the dose per spot is too low [35].
- *Depth scanning*: All spots with the same lateral position are grouped and subsequently scanned in energy. An approach to limit dead time is to change the energy continuously by multiple absorber wedges [36].

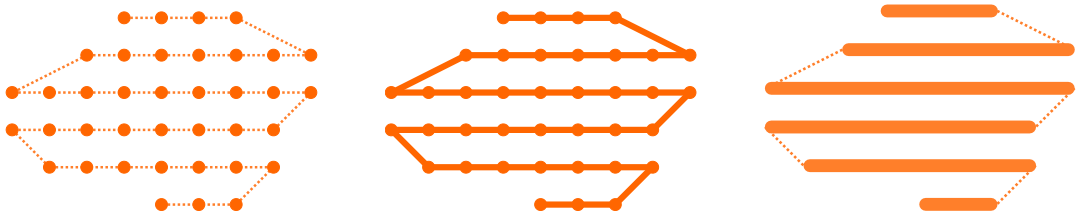

(a) spot scanning (b) raster scanning (c) line scanning

Figure 1.5.: Different approaches to the delivery of active, scanning proton therapy. Circles indicate spots, where dose is delivered with the beam scanning paused. Dashed lines show where the beam is scanned but no dose is delivered. Scanning path optimization is not shown for simplicity.

The first three methods are visualised in figure 1.5.

Raster scanning is faster than discrete spot scanning. Many synchrotron-based systems prefer raster scanning because it utilises the beam more efficiently during the spills.

For all scanning techniques, the beam is switched off while changing the energy, with the possible exception of depth scanning.

Our institution concentrates on spot and line scanning. Spot scanning has been implemented at the *Francis H. Burr Proton Therapy Center* at the *Massachusetts General Hospital* (MGH) in Boston MA, USA, at the *MD Anderson Cancer Center* in Houston TX, USA, at the *Rinecker Proton Therapy Center* (RPTC) in München, Germany and at the *Westdeutsches Protonentherapiezentrum Essen* (WPC) in Essen, Germany.

Implementations of raster scanning have been set up at the *Gesellschaft für Schwerionenforschung* (GSI) in Darmstadt, Germany [20, 36], at the *National Institute of Radiological Science* (NIRS) in Chiba [37, 38, 34], at the *Heidelberg Institute of Technology* (HIT) in Heidelberg, Germany [39, 40] and at the *Centro Nazionale di Adroterapia Oncologica* (CNAO) in Pavia, Italy [41, 42].

1.2.1. Discrete spot scanning

The appeal of spot scanning is mainly due to the following two reasons.

First of all, the idea of IMPT can only be fully implemented by scanning. IMPT means shaping inhomogeneous fields in such a way that the total dose distribution is conformal to the tumour, and organs at risk are optimally spared. Of course, this is also the aim of conventional radiotherapy. But there the fields are homogeneous and therefore the total dose distribution is necessarily convex. For example, with IMPT, the spinal cord can be spared while the surrounding tissue is irradiated from different directions with few fields. The main difference between IMRT and IMPT is the lack of modulation in depth for IMRT. Some degree of IMPT/IMRT is also possible in conventional radiotherapy and scattering proton therapy by using techniques such as wedges, blocked fields and field patching. The true elegance of IMPT is the lack of beam shaping devices. Even in IMRT, this is necessary in the form of an MLC.

This brings us to the second point: no patient- and field-specific beam shaping devices such as collimators or compensators are necessary in scanning, saving time in treatment preparation. Collimators have an additional disadvantage: although they conform the field to the proximal edge of the target by modulating the proton range, this is not possible for the distal edge. Since the shape of the distal edge of the target volume is in general not similar to the shape of the proximal edge, the full dose as prescribed to the target volume is applied to a substantial volume of healthy tissue. This is visible in figure 1.4a. What is more, scanning is well suited to tracking, as discussed in section 3.5.

A peculiarity of spot scanning is the *kicker leakage*. This is the number of monitor units (MU)[1] applied while the *kicker magnet* is opening or blocking the beam, which takes about 50 μs for the PROSCAN beam line at PSI (see section 1.3). The kicker leakage is taken into account by the delivery system [35]. It also defines the smallest deliverable amount of monitor units per spot, equal to a spot with zero dwell time. A consequence is that spots at low energy, which do not contribute much dose to the aggregate dose distribution, are not deliverable if the number of monitor units is less than the kicker leakage. If these spots are skipped, dose is missing. On the other hand, if they are applied, the result is over-dosage. This problem is accentuated in re-scanning, because the probability to get spots with low dose is elevated, as explained in section 3.2.

The lateral distance between spots depends on the lateral beam size to guarantee a homogeneous dose distribution [43]. The step size in energy varies with the width of the Bragg peak in depth, which in turn is determined by the initial energy spectrum, see also section 4.1.2.

1.2.2. Continuous line scanning

We have already seen at the beginning of this section that the difference between discrete spot scanning and continuous line scanning lies in the dynamics of dose delivery.

In principle, the beam could be scanned along arbitrary contours in the lateral plane. This *contour* scanning is not studied in this work. We restrict ourselves to the study of *line* scanning. As the name implies, the beam is scanned along a straight line in order to apply dose. The obvious choice of direction on Gantry 2 is the faster lateral scanning axis. For changing the slower, secondary scan coordinate, the beam is blocked. Otherwise, these turning points would receive too much dose [44]. Generally, such over-dosage could be eliminated by an optimisation routine.

The motivation for line scanning is that it is faster than spot scanning due to the reduced dead time. For line scanning, the main contribution to the dead time comes from the energy change. The dead time while scanning an iso-energy layer is negligible.

The problem of applying a certain dose distribution by line scanning is equivalent to specifying the dose rate per unit distance along the scanning path. The dose rate per unit distance depends on the beam intensity and the rate of change in sweeper

[1] In proton therapy, a *monitor unit* is a measure of the integrated output of the primary dose monitor, an ionisation chamber. As a function of the number of protons delivered, it depends on the beam energy spectrum.

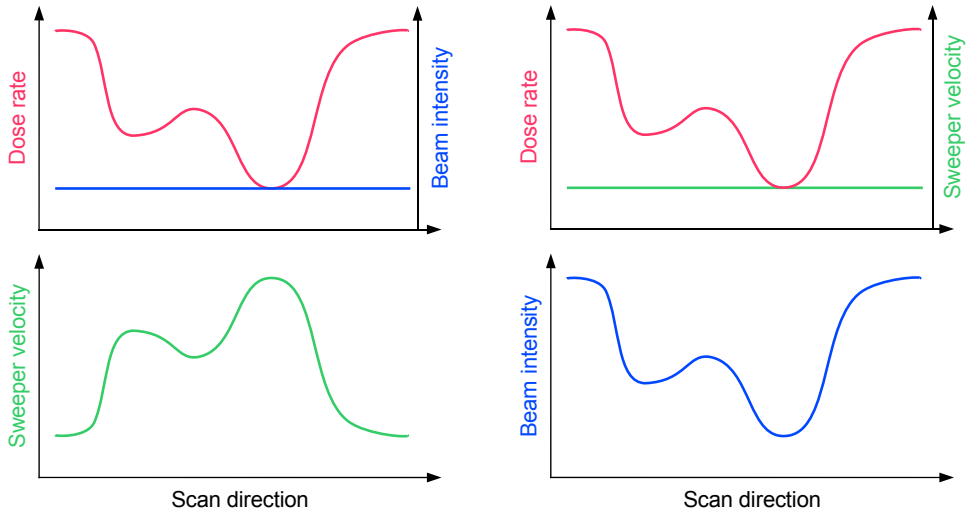

(a) fixed beam intensity (b) fixed sweeper velocity

Figure 1.6.: The two delivery modes for line scanning. In (a), the beam intensity is fixed. The line is shaped by the sweeper magnet velocity. In (b), the sweeper magnet velocity is fixed to the minimum speed, corresponding to the maximal dose rate for 100 % beam intensity.

magnet current, which determines the scanning speed. Two modes of delivering a dose distribution by line scanning can be distinguished, as shown in figure 1.6. The beam current for Gantry 2 is set by a deflector plate inside the cyclotron COMET, as described in section 1.3.

Firstly, if the beam intensity is assumed constant, the dose rate per unit distance is set by adjusting the scanning speed. Because it is always possible to reduce the scanning speed by reducing the rate of change in the current of the sweeper magnets, the beam intensity can be set to the maximal possible value. One drawback of this solution is that the scanning speed cannot be changed nearly as fast as the voltage of the deflector plate. Therefore, on-line compensation of fluctuations in the beam intensity should in any case be provided by the deflector plate. More importantly, the scanning speed is limited. As a result, the dose rate per unit distance cannot be set to an arbitrarily small value without reducing the beam intensity. This is typically only necessary in re-scanning, see section 3.2.

Secondly, line scanning can be delivered at full sweeper speed, where the dose rate per unit distance is controlled only by changing the beam intensity with the deflector plate. The advantage is the short response time of the deflector plate of about 100 μs. However, if the maximal beam intensity is too low, the required dose rate per unit distance may not be achieved. The best approach is to choose locally the fastest mode.

The deflector plate voltage is set by a control loop. The input of the control loop is the voltage output of the primary dose monitor in the gantry nozzle. This voltage corresponds to the current that is induced in the ionisation chamber as protons ionise the

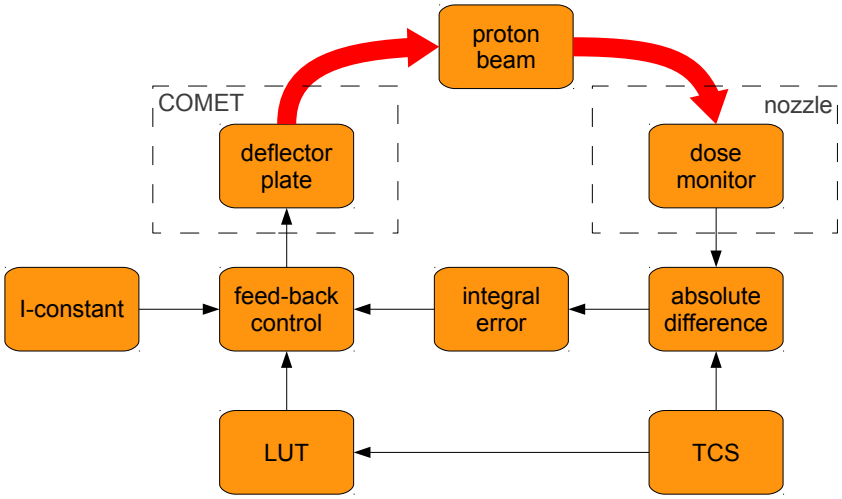

Figure 1.7.: Schematic of the control loop for adjusting the dose rate via the deflector plate. The primary dose monitor is mounted in the nozzle of Gantry 2. TCS is the therapy control system, which provides the target MU rate. The look-up table converts MU rate to deflector plate voltage.

air inside the chamber. In the feed-forward part of the control loop, this correspondence is implemented as a look-up table. This table is typically established once per measurement session. The residual error in beam current is adjusted by the feed-back part. The behaviour of this feed-back loop can be influenced by a parameter, the *I-constant*. This constant determines the influence of the integrated error on the output of the control loop. The integrated error is the difference between the input and the set-point, summed over the integration time. A schematic of the control loop is shown in figure 1.7.

1.2.3. Simulated scattering

Much experience has been gained in scattering proton therapy. Physicians may be reluctant to switch to scanning proton therapy. Ideally, a proton therapy treatment machine should be able to apply both scattering and scanning fields. One possibility to introduce this feature is *simulated scattering*, whereby a treatment plan is delivered by continuous line scanning but shaped and collimated by the same patient-specific devices as in the passive approach [44].

Motion mitigation is provided by fast volumetric re-scanning, imitating the rotating modulator wheel of scattering systems. If the re-scanning frequency is large enough, the dose distributions should not be more sensitive to motion than scattering fields. At the same time, there is an advantage thanks to the beam-shaping ability of scanning systems. While the distal edge of the field is shaped by a collimator, the proximal edge can be shaped in such a way that it is not parallel to the distal edge as in passive proton therapy but is conformal to the target volume. Nothing more is required than adapting the treatment plan by cropping or *shrinking* the iso-energy layers appropriately, at least

(a) (b)

Figure 1.8.: (a) fish-eye view of Gantry 2 and (b) beam coordinate system.

for convex target volumes. The process of shrinking is shown in figure 4.5.

An additional benefit of simulated scattering over passive scattering is the reduced neutron radiation in the beam path. In passive scattering, the treatment field is created by scattering a narrow beam to the required size. In this process, neutrons are produced in the interaction the of protons in the beam and the heavy atoms of the scattering material.

1.3. PROSCAN

At PSI, several treatment rooms are available for proton therapy. Gantry 1 has been operating since 1996 [21]. Gantry 2 is scheduled for starting patient treatments in Autumn 2013 [45]. Finally, OPTIS 2 is treating ocular tumours since 2010 as a successor to OPTIS, which was running since 1984. All three beam lines share one proton accelerator, the superconducting cyclotron (COMET). This means that at any moment, patient treatment is possible only in one room. Because irradiations are fast and most of the time is needed to prepare and transport the patient, this is not a bottleneck. Gantry 2, OPTIS 2 and COMET are referred to as the PROSCAN project.

1.3.1. Gantry 2 - Built for fast scanning

Devised as the successor of Gantry 1 and drawing heavily from its vast experience of 17 years of operation, the design goals for Gantry 2 have been, first and foremost, the ability to treat moving tumours by re-scanning. By contrast, Gantry 1 is not able to perform re-scanning because it can only scan the beam fast in one direction. Any form of re-scanning would cause an unbearably long treatment time.

At the iso-centre, the maximal scanning speed of the two magnets that deflect the proton beam during treatment, the *sweeper magnets*, is 2 cm/ms and 0.5 cm/ms in the

two scanning directions in the plane perpendicular to the beam, see figure 1.4b. These two coordinate axes are referred to as T and U, respectively. In figure 1.8, Gantry 2 and its beam coordinate system is shown. Naturally, when scanning through the target volume, the faster T direction is preferred to the slower U direction, but this preference may be influenced by the main target motion. The scanning speed is most important for continuous line scanning, see section 1.2.2.

1.3.2. COMET - A compact proton cyclotron

The proton beam is provided by a superconducting cyclotron [46]. The energy is fixed at 250 MeV. The COMET is depicted in figure 1.9a with its top cap removed.

It may be interesting to oppose the features of cyclotrons and synchrotrons for ion therapy.

Cyclotron

- Stable, continuous beam current
- Fixed beam energy
- Adjusting energy after cyclotron degrades beam shape and energy spectrum
  - Need to shape beam in beam line
  - Need to select correct energy in beam line
- Compact design (COMET: 3 m in diameter)

Synchrotron

- Beam current is not continuous
  - Beam is delivered in separate spills
  - During spill extraction, beam is continuous but not very stable
- Adjustable beam energy
  - Beam energy can be changed between spills
  - Very precise beam energy
  - Beam is shaped by synchrotron
  - Easy to set beam size, even to very small values[2]
- Spacious design (MedAustron: 25 m in diameter)

The fact that the beam energy is fixed by the configuration of the cyclotron means that a system is needed to adjust the energy during field application. The faster this system is, the shorter the treatment time will be. At PSI, the solution consists of a set

[2] Although the beam size at the output of the machine can also be set to very low values with cyclotrons, the beam size at the patient is necessarily larger because of the energy selection in the beam line after the cyclotron.

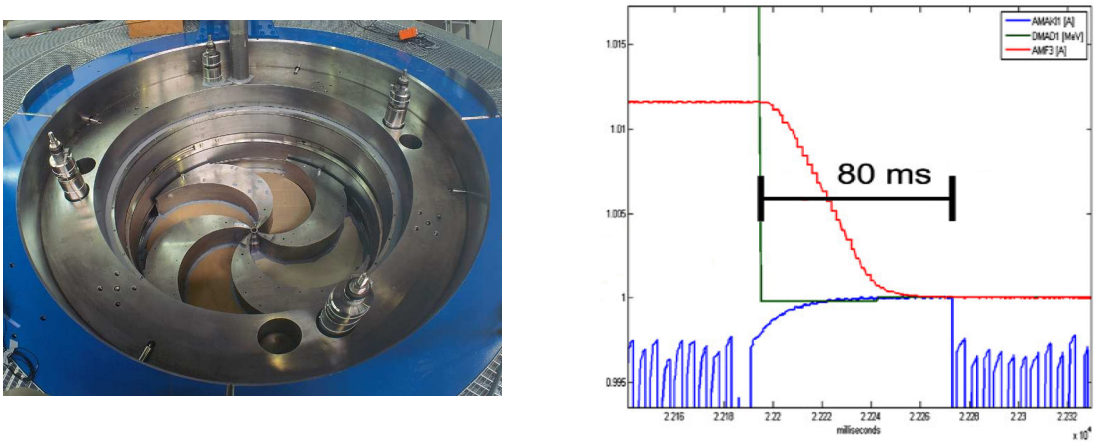

(a) (b)

Figure 1.9.: The superconducting cyclotron COMET is shown in (a), which is used to accelerate the protons. The cap has been removed and the spiral-shaped dees, which help keep the proton beam on track, are visible. In (b), the behaviour of several key components for a fast energy change is plotted. The green line shows the requested position of the carbon wedges. The current in the last bending magnet on Gantry 2 is shown in red. This is the slowest magnet of the whole beam line. The blue line indicates the state of the magnet that blocks the beam. While the energy is changed, the beam is blocked. Image courtesy of [45].

of carbon wedges that increase the amount of matter in the beam path by moving in or out. Taking into account also the necessary changes in the magnet settings of the beam line, a typical energy change of 3 MeV takes only 80 ms, as depicted in figure 1.9b. This is still an order of magnitude faster than that which synchrotrons achieve at the moment. It is an essential building block for enabling re-scanning on Gantry 2.

The disadvantage of such an energy variation system is the loss in beam intensity. The scattering in the wedges increases the beam size and the widens the energy distribution. The required energy is selected by the magnets of the beam line and the beam size is reduced by collimators. Both of these processes invariably reduce the number of particles in the beam. For low energies, over 99 % of the beam intensity is lost.

Inside the cyclotron the beam intensity is adjusted very rapidly by gradually deflecting the beam with the help of a static electric field. In the process, a slit removes part of the Gaussian beam, as shown in figure 1.10a. It follows that the curve relating the voltage of the beam deflecting electric field to the beam intensity is shaped as the cumulative probability function of a normal distribution, the error function. Figure 1.10b shows this curve. Note that the beam intensity is often expressed as the equivalent current of the charged protons. The delay of this so-called *deflector plate* is of the order of 150 μs. It is a very valuable tool for continuous beam scanning, as discussed in section 1.2.2.

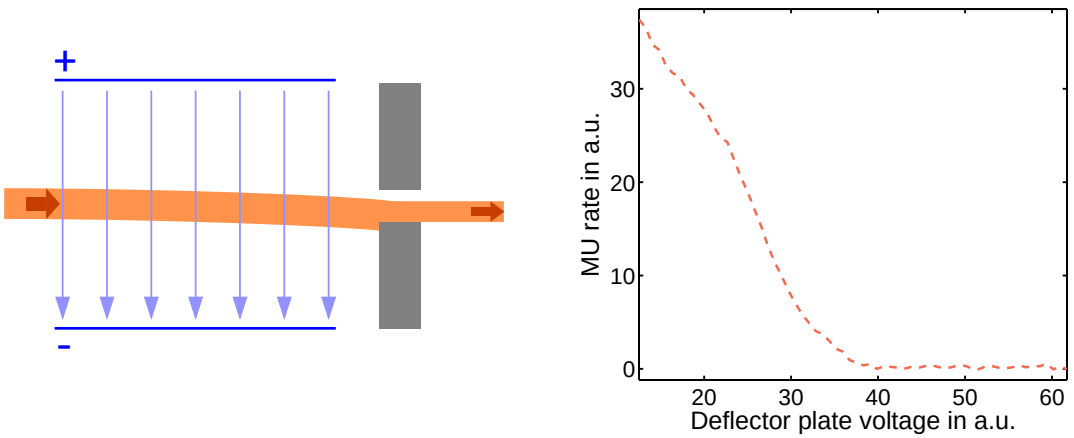

(a) (b)

Figure 1.10.: Deflector plate for beam current control: (a) schematic of the deflector plate, (b) functional relation between the voltage of the electric field applied to the deflector plate and the resulting beam current.

2. Motion

In radiation therapy, not only the treatment machine and patient set-up have an effect on the precision of dose delivery. Also motion inside the patient is an issue [47, 48, 49]. The term *organ motion* simply refers to the effect that any anatomical structure — not only organs — inside the patient can move away from its initial position relative to the skeleton, which can be considered fixed after immobilisation of the patient.

Several types of organ motion are differentiated:

- *Repositioning motion* due to position changes of the patient
- *Interfraction motion* between fractions
- *Interfield motion* between the application of fields of the same fraction
- *Intrafraction motion* during a fraction

To clarify the concept of repositioning motion, consider the following situation. If the computed tomography (CT) images for treatment planning is taken with the patient in the supine position, but the patient is treated in prone position, due to gravity the organs will drift away from their original position as seen on the CT.

Interfraction motion boils down to weight gain or weight loss, different filling of bladder, rectum or intestine or gas bubbles therein, changes in tumour size due to response to treatment or drift of tumours, for instance in the lung. Uncertainties in daily patient positioning are also a type of interfraction motion.

Examples of interfield motion are slow shifts of the patient, e.g., due to relaxation, and drifting gas bubbles in the intestine. They do not have to happen outside of the field application. This category exists merely because the application time of a single field is usually shorter than the time between fields.

Intrafraction motion is primarily caused by respiratory and cardiac motion. Even so, different filling levels of bladder rectum or intestine and the points mentioned for interfield motion contribute, too. The amplitude of cardiac motion is about 0.7 mm on the surface of the patient [50], which is much smaller than the amplitude of respiratory motion, and 1–4 mm for tumours near the heart and aortic arch [51]

2.1. Extent of organ motion

An exhaustive review of organ motion has been published over a decade ago [52], except for head and neck tumours. In tables 2.1 and 2.2 a selection of recent studies are compiled.

The following abbreviations for the coordinate axes of a patient are used in the tables:

- *SI* = superior to inferior: from head to toe. The *SI* direction is equivalent to *CC*: cranio-caudal.
- *AP* = anterior to posterior: from the front to the back.
- *LR* = left to right: from the left side of the body to the right side, from the patient's point of view.

Common abbreviations for imaging modalities are used as well:

- *CT*: computed tomography
- *4D-CT*: set of CT images for different breathing phases
- *cine-CT*: time-resolved CT image sequence, mainly for cardiac imaging
- *CBCT*: cone-beam CT[1]
- *RTRT*: Real-time tumour tracking in radiotherapy[2]
- *MRI*: magnetic resonance imaging
- *4D-MRI*: set of MRI images for different breathing phases
- *cine-MRI*: similar to 4D-MRI, mainly for cardiac imaging

2.2. Motion effects in radiotherapy

Why is organ motion a problem? In conventional radiotherapy, only static fields are applied. If the target volume is deformed or shifted from its planned position, the dose distribution does not cover the tumour any longer and some parts of the tumour are underdosed, whereas some parts of normal tissue or even organs at risk (OARs) are overdosed. In the region where the field and the target overlap, however, the correct dose is applied. This is different in IMRT, since there the uniformity of the final dose distribution relies on the precise superposition of inhomogeneous fields. If one field is shifted with respect to another, the uniformity of the resulting dose distribution is degraded [75].

The same rationale holds for protons. Steep dose gradients inside the field are especially susceptible to organ motion [76, 77]. Additionally, protons are much more sensitive

[1] The word 'cone' in the abbreviation of CBCT refers to the shape of the radiation field, rather than a fan as in conventional CT imaging. CBCT data can be acquired on-line on the treatment machine by rotating it around the patient, either with kilo-voltage (kV) radiation from an X-ray tube mounted on the treatment machine or with mega-voltage (MV) radiation provided by the treatment machine itself.

[2] This system consists of two X-ray tubes and two detectors, which continuously acquire images (*fluoroscopy*) to monitor tumour motion [53].

Author	Modality	Patients	Result
Head and neck			
Den [54]	CBCT	28	Interfraction shifts: 1.7 mm ± 1.9 mm SI, 1.8 mm ± 2.1 mm AP, 1.4 mm ± 1.4 mm LR
Lung			
Seppenwoolde [51]	RTRT	20	Intrafraction: 12 mm ± 2 mm SI, 2 mm ± 1 mm AP and LR tumours not attached to rigid structure
Shirato [55]	RTRT	21	Tumour speed (min, mean, max): 6.6 mm/s ± 3.6 mm/s, 9.9 mm/s ± 5.4 mm/s, 21.1 mm/s ± 18.9 mm/s Intrafraction mean: 10.7 mm ± 8.6 mm SI, 8.8 mm ± 7.0 mm AP, 8.2 mm ± 6.5 mm LR
Mori [56]	cine-CT	14	Intrafraction mean displacement at peak exhalation: 10.3 mm SI, 4.0 mm AP, 1.9 mm LR
Britton [57]	4D-CT	8	Intrafraction mean: 8.6 mm ± 1.9 mm SI, 3.9 mm ± 0.8 mm AP and 1.9 mm ± 0.5 mm LR Interfraction mean: 5.4 mm ± 3.2 mm SI, 4.5 mm ± 2.7 mm AP and 3.0 mm ± 2.3 mm LR
Suh [58]	Cyberknife	42	Intrafraction mean: $\geq$ 5 mm in 40% of the fractions, 4.8 mm overall
Sonke [59]	CBCT	56	Interfraction (mean ± σ_{sys} ± σ): −0.2 mm ± 3.9 mm ± 2.4 mm SI, −0.5 mm ± 2.8 mm ± 2.2 mm AP, 0.4 mm ± 1.6 mm ± 1.2 mm LR
Quirk [60]	optical	120	Intrafraction mean: amplitude 10 ± 5 mm, period 3.6 ± 1.0 s baseline drift > 5 mm for 40 % of patients
Breast			
Price [61]	3D optical	13	Intrafraction mean: 2–4 mm AP, inter- and intrafraction variability: $\leq$ 1 mm
Diaphragm			
Wysocka [62]	4D-CT	22	Interfraction mean: 20 mm SI

Table 2.1.: Recent papers on organ motion part I. [a]They measured less motion along the SI axes in the sagittal plane than in the coronal plane, so the results should be interpreted with care.

Author	Modality	Patients	Result
Oesophagus			
Patel [63]	4D-CT	30	Intrafraction mean: 8.0 mm ± 4.5 mm SI, 2.8 mm ± 2.0 mm AP, 2.2 mm ± 2.3 mm LR
Liver			
Eccles [64]	cine-MRI	60	Intrafraction mean: 11.6 mm SI, 5.6 mm AP
Kitamura [65]	RTRT	20	Intrafraction mean: 9 mm ± 5 mm SI, 5 mm ± 3 mm AP, 4 mm ± 4 mm LR
Bussels [66]	MRI	12	Intrafraction mean: 24.4 mm ± 16.4 mm SI (dominant)[a]
Von Siebenthal [67]	4D-MRI	13	Intrafraction mean of all traced points: 6.4 − 20.1 mm Intrafraction mean drift: 1.6 − 7.1 mm
Pancreas			
Bussels [66]	MRI	12	Intrafraction mean: 23.7 mm ± 15.9 mm SI (dominant)
Feng [68]	cine-MRI	17	Intrafraction mean displacement from end-exhalation position (S/I/A/P tumour border): 20 mm ± 10 mm / 20 mm ± 8 mm / 8 mm ± 3 mm / 6 mm ± 2 mm
Kidneys			
Bussels [66]	MRI	12	Intrafraction mean (left/right): 16.9 mm ± 6.7 mm / 16.1 mm ± 7.9 mm SI (dominant)
Uterus			
Kerkhof [69]	MRI	22	Intrafraction mean shift (sacral promontory/pubic symphysis): 1.6 mm ± 0.8 mm/2.3 mm ± 1.6 mm
Collen [70]	CBCT	10	Intrafraction mean shift (relative to planning CT): 6.1 mm ± 11.6 mm superior, 5.0 mm ± 11.2 mm inferior, 3.3 mm ± 11.9 mm anterior, all other shifts much smaller
Beadle [71]	CT	16	Interfraction mean maximum (cervix): 2.1 mm SI, 1.6 mm AP, 0.8 mm LR
Prostate			
Mah [72]	cine-MRI	42	Intrafraction mean: 0.0 mm ± 3.4 mm SI, 0.2 mm ± 2.9 mm AP, 0.0 mm ± 1.5 mm LR
Langen [73]	transponder	17	Intrafraction displacements: ≤ 3 mm for 13.6%, ≤ 5 mm for 3.3% of total treatment time
Adamson [74]	fluoroscopy	30	Intrafraction mean ± systematic error ± random error: 0.6 mm ± 1.2 mm ± 2.0 mm SI, 0.5 mm ± 1.3 mm ± 1.9 mm AP, 0.9 mm ± 0.5 mm ± 0.1 mm LR

Table 2.2.: Recent papers on organ motion part II.

to changes in tissue density, because this affects their range in the body. The Bragg peak is moved from its planned position and the lateral width of the peak increases upstream of tissue inhomogeneities [78]. In the case of active, scanning proton therapy, the dose is applied dynamically. Ideally, the total dose distribution is uniform. Yet if the target volume is moving during irradiation, *cold* and *hot* spots of under- and over-dosage occur respectively [79, 80]. This *interplay effect* is of major concern because cold spots inside the target volume are less effective in killing cancerous cells, while hot spots increase the risk of complications and the secondary cancer risk of healthy tissue inside and outside of the tumour. If the prescribed dose is increased to compensate for the cold spots, healthy tissue and OARs receive higher dose as well.

The interplay effect is not restricted to active, scanning proton therapy. It shows up in dynamic multi-leaf collimator (dMLC) delivery of IMRT [81, 82, 83, 84], in tomotherapy [85, 86] and in dynamic arc treatment [87, 88, 86, 89, 90, 91]. These results may be summarised by saying that interplay is negligible except for single fractions and single fields, where there is not sufficient averaging.

A large part of the breathing cycle consists of the inhale and exhale phases, while the average tumour position is located in between. Because the average tumour position is often used to set up the patient, much of the target volume is frequently irradiated with the penumbra region of the field, where dose gradients are high, subsequently leading to interplay effects [92]. Unless motion mitigation techniques are used, this restricts scanning charged particle therapy to tumour sites which are not affected by respiratory or cardiac motion. Examples where mobile tumours have been treated are rare. In Germany, at the RPTC, patients have been anaesthetised and treated in apnoe [93]. At HIT, liver patients have been treated with scanned carbon ions. Abdominal compression and gating was used to reduce motion effects [94]. In Japan, at NIRS, soon lung patients will be treated with gating.

The margin approach of conventional radiotherapy is not suited to mitigate motion effects in scanning ion therapy [95, 77]. See section 3 for an introduction to motion mitigation techniques.

In passive, scattering proton therapy, margins are replaced by techniques such as smearing, opening of the collimator and removing material from the compensator [96]. These means are not available in active, scanning proton therapy. There is even no consensus on a simple, standard definition of the planning target volume [2]. Especially for IMPT with its steep in-field dose gradients it is questionable whether the margin concept is sufficient [97].

The same dose distribution can be delivered by many different spot sets, usually obtained by different optimisation algorithms or start conditions. These sets do not react the same with respect to set-up errors and organ motion [76]. Therefore, research is headed into the direction of robust planning [98, 99, 100, 101, 102, 103, 104].

2.2.1. Quantification of motion effects in ion therapy

Generally, motion effects are proportional to the motion amplitude [79, 105, 106]. The minimum and maximum dose in the target volume decreases and increases, respectively,

with motion amplitude [107]. Motion amplitudes of up to 5 mm have been frequently reported to be unproblematic [95, 108, 109, 110]. The motion period does not seem to have a large effect as long as there is no resonance between the time to scan an iso-energy layer and the motion period [79, 105]. A longer period has been reported to be beneficial, though [111]. The interplay effect might correlate with treatment time but both positive [106] as well as negative [111] correlation has been found. In case of baseline drift, a positive correlation is likely.

For cubic targets, motion along the main scanning direction has less an adverse effect on the dose distribution than motion perpendicular to it [112, 105, 106], yet for spheres this effect is already elusive, especially for high scanning speeds [110, 113], and irrelevant in most cases for realistic target volumes [111]. The impact of small rotations is also limited [112]. Irregular motion tends to average dose errors [114].

The interplay effect is highly specific to the patient, the tumour location and the delivery system [111, 107]. It seems to be unpredictable from the full set of motion parameters, mostly due to the motion starting phase [105, 111]. As most dose is delivered by the most distal iso-energy layers, the timing of their application has a major influence on dose homogeneity.

Dose homogeneity is worst in the distal part of the target volume because proximal iso-energy layers receive also dose from distal layers at different motion phases, which helps smear out the dose error [112]. The interplay effect does not correlate with the tumour volume [107].

Motion in the lateral plane broadens the penumbra [106]. Dose error is seen mostly at the edge of the target volume. This also has to do with the motion asymmetry [115]. For example, if motion is simulated according to the function $\sin^4$, more time is spent in the exhalation phase. If a homogeneous field is assumed, overdosage in the exhalation phase and underdosage in the other phases is the result. The mean shift of the dose distribution due to asymmetric motion is about 10–20 % of the amplitude [106].

The water-equivalent range of structures inside the patient may change, for instance if a rib, composed of high-density tissue, moves in front of the tumour. This effect widens the Bragg peak in range and OARs located distally to the target may receive additional dose [116, 109].

Surprisingly, the effect of motion could be averaged out better in uniform scanning than in scattering [117].

An overview of studies about the interplay effect is given in table 2.3 for simulations and in table 2.4 for measurements. Not listed in the tables are the studies from Dowdell et al. [111] and Grassberger et al. [107]. Both simulated treatments on 4D-CT data sets with Monte Carlo code. Some of their results are cited above.

Author	System	Target	Motion	Results
Phillips [79]	ss + p	cuboid in water	sin (A = 0–30 mm, P = 1–10 s)	inhomogeneity: static 1 %, motion in Y (A = 10 mm, P = 5 s) 10.8 ± 1.5 %, same motion with double beam width 3 %
Groezinger [112]	rs + c	sphere in water	sin (A = 30 mm, P = 4 s)	V_{80} = 47 %, 76 %, 82 % for X, Y, Z motion
Bert [105]	rs + c	lung tumour 4D-CT	$\sin^4$ in X, Y, Z (A = 12–28 mm, P = 2–6 s)	$V_{95} = 71.0 \pm 14.2$ %
Seco [106]	ss + p	cuboid in water	$\sin^n$ (A = 30 mm, P = 3.3–5.2 s)	Penumbra (10–90 %: static 8 mm, motion 48 mm
Kraus [114]	ss + p	lung tumour 4D-CT	A = 5.9–16.1 mm in 2D	$D_{95} = 74 \pm 6$ %
			P = 1.5–7.5 s	$D_{95} = 76 \pm 2$ %
			drift = -7.2–7.2 mm	$D_{95} = 68 \pm 16$ %
			phase = 0–100 %	$D_{95} = 75 \pm 2$ %
			irregular	D_{95} = 78 %

Table 2.3.: Quantification of the interplay effect due to organ motion. Studies based on analytical dose calculations. Delivery method: discrete spot scanning (ss), raster scanning (rs), uniform scanning (us), scattering (sc). Ion type: carbon (c), proton (p). Motion directions: parallel to primary scanning (X), perpendicular to primary scanning (Y), parallel to beam axis (Z). Motion parameter: peak-to-peak amplitude (A), period (P). See section 4.4 for an explanation of the meaning of the D and V values.

Author	System	Detector	Target	Motion	Results
Bert [118]	rs + c	radiographic film	cuboid in water	regular in X (A = 20 mm, P = 3 s), wedge in Z	homogeneity: static 97.3 %, motion 88.8 %
		3D IC array			rel. dose difference: all ICs −9±38 %, ICs in target 27 ± 14 %, ICs distal to target 45 ± 66 %
Bert [105]	rs + c	radiographic film	rectangle in air	sin (A = 16, 30, 40 mm, P = 3–7 s)	homogeneity: static 97 %, motion 87–90 %, 69–83 %, 78–79 %
Groezinger [119]	rs + c	radiographic film	square in air	X, Y: A = 30 mm, P = 10 s	homogeneity: static 97 %, motion 66 %
Su [117]	us + p	3D gel	cylinder	sin in Y (A = 20 mm, P = 4 s)	$P_{\gamma<1} = 75\,\%$
	sc + p				$P_{\gamma<1} = 70\,\%$

Table 2.4.: Quantification of the interplay effect due to organ motion. Studies based on experiments. IC: ionisation chamber. See the caption of table 2.3 for the key to the other abbreviations.

3. Motion mitigation

An important means of reducing motion effects is immobilisation of the patient [120]. For the treatment of head and neck tumours, a face mask or a bite block is used to fix the skull. Thermoplastic masks are wrapped around the head while the material is hot, and subsequently stiffen while cooling down. Holes in the mask reduce the amount of range shift incident beams due to the mask material. Parts of the body that are up to two joints away from the target volume have to be immobilised. Thermoplastic sheets are wrapped around the patient. Bags filled with styropor elements take on the shape of a patient. This shape is stabilised by pumping out the air from the bag. Another option is using a mask or mould made out of plaster of Paris. Devices that can be rigidly attached to the treatment couch are more accurate [121].

Motion effects have to be taken into account when creating a treatment plan. According to the guidelines of the International Commission on Radiation Units and Measurements (ICRU), organ motion should be accounted for in the internal target volume (ITV) and set-up errors as well as inaccuracies in dose delivery in the planning target volume (PTV) [122, 123]. These definitions are shown in figure 4.2a. When 4D imaging of the patient is available from CT, MRI or positron emission tomography (PET) data sets, the influence of organ motion can be included in treatment planning [124, 125, 126]. For example, the envelope of the clinical target volume (CTV) during a breathing cycle is a way of defining the ITV [127]. Of course, this approach is detrimental to dose conformity and sparing of normal tissue. It removes the interplay effect in IMRT [92] and (in the absence of tissue heterogeneities, which lead to range changes) in scattering proton therapy, but not in scanning proton therapy [95].

Relevant to interfraction motion is the minimisation of patient set-up errors. This is not discussed here. Repositioning errors only can be eliminated by keeping the patient in the same position during the whole treatment and allowing the organs to settle before treatment is initiated. CT for treatment planning has to be taken in exactly the same position as intended for radiotherapy delivery and using the same immobilisation equipment.

Theoretically, the best approach is to track the tumour with the field [128], see section 3.5. Other efforts focus on reducing organ motion by controlling respiration. Either the breathing cycle is measured and the beam is only delivered when the breathing amplitude or phase lie in a given range (*gating*, see section 3.3), or respiratory motion is completely stopped for a short time during beam delivery (*breath-hold*, see section 3.4). A problem of this method is that respiratory motion is not predictable because even for patients who breathe regularly most of the time, stretches of irregular breathing are inevitable [129].

A simple approach to mitigate the effect of organ motion on active, scanning proton

therapy is to increase the beam size or decrease the spot spacing [79, 130, 111, 107]. In this fashion, more spots contribute to the dose at a given point. Dose error due to motion offset of one spot affects the dose homogeneity less. In this fashion, local control in lung cancer patients could be restored for motion amplitudes of up to 30 mm for conventional, fractionated treatment at the cost of increased mean lung dose [107]. The drawback of this method is that dose conformity to the target dose is compromised since the pencil beams are less sharp, leading to a larger penumbra.

Fractionation exploits statistics when delivering the whole dose in several fractions. The hot and cold spots of the field delivered to the target volume are averaged out. The standard deviation of the dose decreases as the inverse square root of the number of fractions or field deliveries [79]. A promising approach is to use this statistical effect and technological advances in scanned particle therapy to scan the target volume many times per fraction, as discussed in section 3.2.

In order to mitigate interplay effects caused by respiratory motion of the target volume, the respiratory motion is determined by one of various techniques, e.g., spirometry, infrared tracking of a point or a surface on the patient, kV or MV X-ray imaging or an abdominal belt [48, 49]. This topic is presented in section 3.1.

3.1. Motion detection

For motion mitigation techniques such as gating, breath-hold and tracking, knowledge — or at least a close approximation — of the tumour location is required. The tumour position can be measured nearly in real-time by X-rays [53]. Since imaging during treatment adds dose to the patient, we concentrate on motion detection techniques that do not rely on continuous kV imaging.

3.1.1. External markers

Infrared tracking of a marker on the body surface is possibly the most widespread motion detection system in radiotherapy [131]. In the case of the Real-time Position Management (RPM) system (Varian Medical Systems, Palo Alto, CA, USA) the marker consists of a highly reflective block. A camera system illuminates the block and registers the reflected light. The position is calculated in three dimensions at a frequency of 30 Hz. The mean error for realistic motion trajectories is typically below 2 mm [132].

Consumer electronics systems for infrared tracking are catching up with currently available medical equipment [133, 134], while being available at a much lower price. Of course, these devices are not certified yet for medical use.

In hybrid gating [135, 136], the correlation between tumour motion and external marker is updated by imaging the internal location with a certain frequency. The Cyberknife system (Accuray Inc., Sunnyvale, CA, USA) has a tumour localisation error of 1.9 ± 0.9 mm with kV images taken every 1–2 min to update the correlation model [137]. The Exactrac II system (BrainLab, Feldkirchen, Germany) reduces tumour motion to 1.7 mm in adaptive gating treatment [138].

These kV imaging systems require fiducial markers to be surgically implanted in the tumour. Besides other complications, this operation can cause pneumothorax[1] and markers can migrate away from the tumour, so a marker-less approach is desirable. The breathing phase can be determined by continuous kV imaging in various ways: by intensity variations of the lung during breathing [139], matching of a tumour template [140, 141], image classification with a support vector machine [142], image matching by mutual information [143], tumour tracking by optical flow, i.e., dead reckoning [144], and principal component analysis for surrogate position prediction [145]. Template matching also works on CBCT images [146]. Obviously, this cannot be used for real-time motion detection. A commercial solution is available for the Cyberknife, the Xsight Lung Tracking (XLT) System [147]. It has been successfully introduced into clinical practice [148]. Patients with large tumours are better suited to trackerless treatment because these tumours have a high chance of being visible [149].

Hybrid gating relies on frequent updates of the correlation between internal and external motion. A fixed frequency of, e.g., 10 Hz has been reported [135]. Such an approach is not optimised for gating, however. A better approach is determining the tumour position once per breathing cycle to ensure a good correlation near or inside the gating window [136]. Outside of the gating window, high precision is not required. In the beginning, a training phase with an acquisition frequency of 30 Hz over a few breathing cycles establishes the initial correlation model parameters.

Another idea is to track the markers on the MV portal images and switch on the kV imaging only when the markers are not visible [150]. While imaging dose is clearly reduced compared to continuous kV imaging, time lag is still of the order of 300 ms. The time delay of optical systems is of the order of the measurement period, e.g., 33 ms for the RPM system [151, 152].

A more critical analysis of the RPM system showed that gating could reduce the standard deviation of external motion only by 0.3 mm or 6 % and was even larger in one patient [153].

External motion monitoring is feasible at a low price with acceleration sensors as available in consumer electronics devices [154]. By contrast, electromagnetic position sensors are not as widely available but they can be combined with a dosimeter [155].

A solution to improve the accuracy of external marker tracking is the introduction of a larger number of markers [156, 157]. Still, phase shifts can occur. What is more, depending on the location on the patient, markers are dephased with respect to one another [158]. This pattern may also change between fractions. Incorporating both phase and amplitude information into the motion model may help [159].

Interestingly, in one study prediction errors on the tumour motion could not be reduced by updating the prediction model by intrafraction imaging [160]. This suggests that the

[1] Each lung is separately enclosed by the pleura, a double layer of membrane. The space between these two layers is called the pleural space or pleural cavity. It is filled with the pleural liquid. Thanks to the pleura, the lungs are following the motion of the chest wall, but they are not rigidly attached to it because the inner pleura layer slides on the outer layer. Pneumothorax is the intrusion of gas, e.g., air, into the pleural cavity. This may lead to the collapse of the lung, which is a potentially life-threatening condition.

lowest achievable localisation error of external surrogate methods is already reached with immediate pre-treatment imaging.

3.1.2. Correlation issues

Many studies have looked at the correlation between internal motion of anatomical structures and external motion on the surface of the patient [161]. One possible pitfall is the fact that patients require several minutes before they settle into regular and quiet breathing, if they do so at all [129]. If the correlation model is determined before this happens, correlation errors are bound to occur. Another problem is the phase shift between different parts of the body moving according to breathing and its variability during treatment [162, 163, 131, 129, 164, 165, 166]. For instance, one study observed a phase shift of 200 ms between an external marker and the diaphragm [162]. Besides this phase shift, diaphragm motion correlates well with external markers on the abdomen [167]. Due to phase shift, the minimum dose that 95 % of the target volume receives correlates well with lung tumour displacement rather than with respiratory phase, indicating that external surrogates are suboptimal in respiratory gating [109]. Moreover, fluctuations in the exhale position of lung tumours occur in about 20 % of the patients [168]. This means that the surrogate motion is not always in the gating window in the exhale phase.

External markers might be a good solution for tumours which are close to the diaphragm such as in the abdomen [169, 157]. In this case, SI motion of the tumour correlates with AP motion of the tracker [129]. Similarly, in the case of the lung, the best correlation between organ and abdominal marker is between SI lung motion and AP marker motion [170, 165]. In the liver, drift of the external marker is not necessarily correlated with the drift in liver motion [171]. Motion in inferior parts of the liver is less reproducible than diaphragm motion due to intrafraction deformation of the liver.

3.1.3. Abdominal belt

A small strain gauge detector has been used successfully in proton treatment of liver tumours [172]. A similar, commercial system is the Anzai belt (Anzai MEDICAL, Tokyo, Japan) containing a pressure sensor. The belt is wrapped around the abdomen. The amplitude signal correlates well with the RPM signal, but phase differences between the two signals may occur [173].

The difficulty of use, instability of the signal and obstruction by immobilisation devices have been mentioned as the drawbacks of belts [162].

3.1.4. Body surface imaging

Stereo cameras image the body surface in 3D. Adding the time as a 4th dimension, body surface imaging systems detect respiratory motion in 4D. The maximum standard deviation of translational motion detection in such a system is 0.75 mm [174]. An imaging frequency of 6.5 Hz is reported, which might be too low to detect fast changes in the motion trajectory. Tracking the whole surface predicts tumour motion more precisely than

tracking only a single point [175, 159]. Both approaches correlate well with spirometry and are not subject to drifts, in contrast to spirometry, see section 3.1.5.

GateCT (VisionRT, London, UK) is a commercial surface imaging system. It is a reliable tool for phase gating, yet RPM is superior in amplitude gating [176].

Another approach is time-of-flight body surface reconstruction [177]. The patient is illuminated with modulated light. The surface is reconstructed from the phase shift in the captured modulation signal. Frequencies are as high as 20 Hz. In order to make sure that the phase difference is unambiguous, the camera has to be closer than 7.5 m to the patient. This is hardly a problem in any treatment room. The performance is comparable to other external surrogate techniques. The tracking error is 1.62 ± 1.08 mm and the time delay is 65 ms [178].

3.1.5. Spirometry

Respiratory motion is related to the air flow through the trachea and the air temperature. Spirometers are able to measure air flow. The air temperature sensor and strain gauge methods were deemed best suited to gating because they are comfortable for the patient and have a large signal-to-noise ratio [179].

Lung volume has a higher correlation with tumour motion than external, abdominal motion and this correlation is also more reproducible between fractions [164].

A problem with spirometry is that the signal usually drifts in time [180, 181, 175, 182]. Solutions to this problem have been suggested [180]. Still, spirometry is not recommended for amplitude gating. On the other hand, it is considered superior to phase gating based on external markers because the phase shift between air flow and tumour motion is less [164, 183]. Another problem shared by both the surface imaging and spirometry approaches is that if the baseline is set to fully relaxed exhale phase, the stability of the target position cannot be guaranteed. What is more, residual lung volume may change during the treatment.

Better results are achieved with a pneumotachigraph, which measures lung volume by integrating the air flow [184]. Combining spirometry and optical tracking of external markers lead to more accurate results than using only one of the surrogates [183].

3.2. Re-scanning

The motion mitigation technique that is easiest to implement in scanning proton therapy is re-scanning, where the pencil beam is scanned through the target volume not just once but several times. The motion offset between desired and actual spot position in the target volume is ideally random for each re-scan. By superimposing the inhomogeneous dose distributions of all re-scans, it is expected that the hot and cold spots cancel each other. As a result, the summed-up dose distribution becomes more homogeneous.

The standard deviation of the actual dose from the planned dose due to respiratory motion has been shown to decrease as a function of $1/\sqrt{N}$, where N is the number of

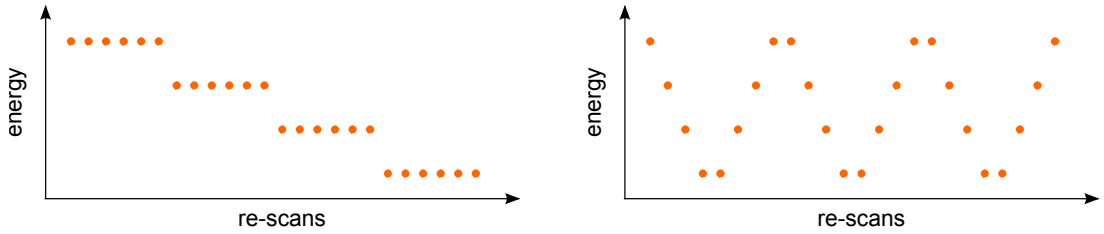

(a) layered re-scanning (b) volumetric re-scanning

Figure 3.1.: Two possibilities of arranging the re-scanning sequence of the iso-energy layers. Each dot represents one re-scan of an iso-energy layer.

fractions or re-scans [79, 81, 37, 92]. This value is one possible measure of the *dose homogeneity*.

Re-scanning is specific to scanning proton therapy. In scattering proton therapy, there is inherent re-scanning because the energy layers of the fields are delivered at a frequency of about 40 Hz [185].

Since in most systems changing the energy is much slower than adjusting the lateral spot position, iso-energy layers are scanned one after another. There are several possibilities to do this [106]:

- *Slice-by-slice or layered re-scanning*: Each iso-energy layer is re-scanned before changing the energy to switch the layer.
- *Volumetric re-scanning*: The whole tumour volume is scanned in one go and then re-scanned.
- *Random volumetric re-scanning*: The order of iso-energy layers irradiated in volumetric re-scanning is random.

Schematics of these methods are given in figure 3.1. Volumetric re-scanning is only feasible if the energy can be changed fast enough, as it is the case for Gantry 2. Because this delay grows with the energy separation, random volumetric re-scanning would further prolong the treatment.

Several algorithms for distributing the spot weights between the re-scans have been conceived of [110]:

- *Scaled re-scanning*: The spot weights are divided by the number of re-scans.
- *Iso-layered re-scanning*: An upper limit of dose delivered to a spot per re-scan is set. Assuming a constant beam intensity, this readily translates to a maximum *dwell time* per spot and re-scan.
- *Mixed re-scanning*: For spots with a weight above a certain threshold, scaled re-scanning is applied. All other spots are subject to iso-layered re-scanning.

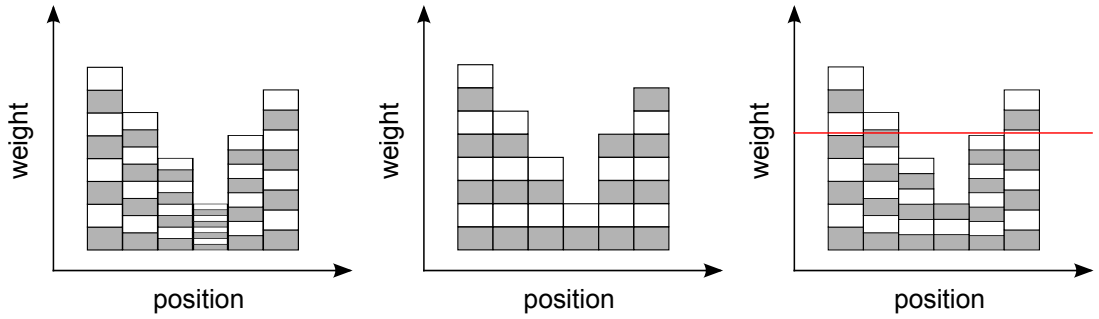

(a) scaled (b) iso-layered (c) mixed

Figure 3.2.: Comparison of re-scanning methods. Shown is one row of spots in an iso-energy layer. The red line in (c) indicates the threshold for switching between scaled and iso-layered re-scanning.

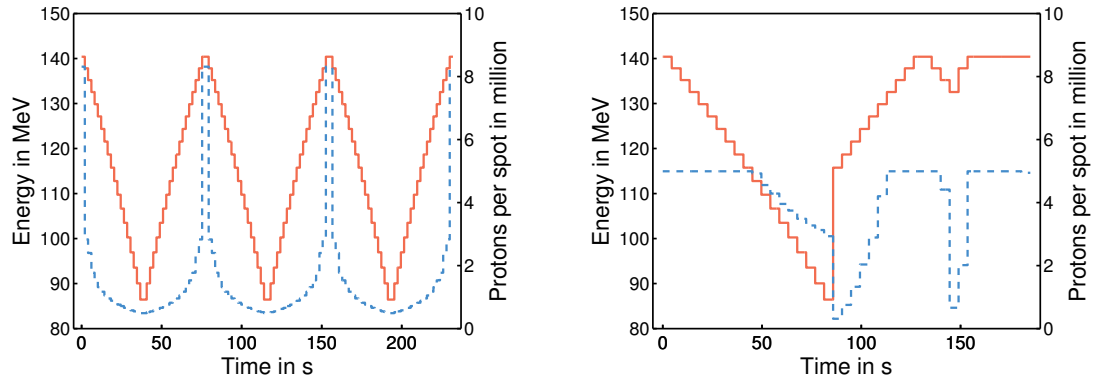

(a) scaled re-scanning (6 times) (b) iso-layered re-scanning (2 ms dwell time)

Figure 3.3.: Energy sequence (full line) and distribution of dose per spot (broken line) for two methods of re-scanning. The target volume is a cube with side length 8 cm. Dose is expressed as number of protons.

Schematics of these methods are given in figures 3.2 and 3.3. These re-scanning methods depend on one or two parameters. By increasing the number of re-scans or decreasing the dwell time, the effect of re-scanning is usually enhanced. In this way, the re-scanning methods are tailored to the amplitude of motion. However, the amount of re-scanning possible is limited for technical reasons.

Scaled re-scanning is susceptible to low-weighted spots because re-scanning these spots can introduce spots with less than 100 MU. In this case, as the dose resolution of the delivery verification system is at least 1 MU, a delivery error of 1 % would not be detected. What is more, too many low-weighted spots in sequence may raise an interlock[2] as the

[2] An interlock is an error detected by the treatment control system that is likely to lead to an interruption of the delivery.

kicker magnet is not able to open and close the beam line fast enough. Finally, the dead time introduced by the necessity to visit each spot of the target volume in every re-scan, while only delivering a small dose to many spots, is considerable. Continuous line scanning mitigates both of these problems.

Since the central and proximal parts of a target volume receive much dose from more distal spots, the spot weights on the border of iso-energy layers are generally higher. Considering iso-layered re-scanning, two conclusions can be drawn from this fact.

First, decreasing the dwell time affects mainly the highly weighted spots. After a couple of re-scans, the low-weighted spots are not visited any more, meaning that they are not re-scanned as many times as the highly weighted spots and only at the beginning of the treatment, followed by re-scanning only the highest weighted spots in fast succession. The full statistical effect of re-scanning cannot be exploited. This problem could be tackled by improving the algorithm so that the highest weighted spots are more separated in time.

Second, the total dead time is reduced with respect to scaled re-scanning, but it gives rise to the question how the remaining spots are scanned most efficiently. The benefit of smaller treatment time by solving this *travelling salesman problem* (TSP) is small compared with simply choosing a meander path, where the beam is scanned along straight lines and the scan direction is alternating [110]. For raster scanning with a synchrotron and delay of 1.5 s for changing the energy, the TSP path length is 13–56 % shorter for different patient cases but the delivery time is less than 1 % shorter [186]. For re-scanning, this value is 4–20 %. These values depend on the scanning system. A spiral path can also be chosen [37]. In conclusion, the choice of scanning path is mainly determined by the scanning speeds and dead times for the three scan directions. Scanning path optimisation might only be important for the implementation of re-scanning for raster scanning [186, 187].

Mixed re-scanning is the natural solution for solving the problems of scaled and iso-layered re-scanning. The distribution of the number of re-scans is narrower than in the case of iso-layered re-scanning. At the same time, the treatment time is only slightly longer than for iso-layered re-scanning.

Although re-scanning can reduce interplay effects, a larger volume of healthy tissue is irradiated as well because the target volume always has to cover the tumour. Hence, combining re-scanning with gating or breath hold is necessary for large tumour motion [37, 188]. The target volume should also include the effects of range changes due to organ motion [189, 190, 191].

Another drawback of re-scanning is the possibility that some spots are scanned with a similar frequency as the target motion so that interference occurs [81, 192, 105, 110]. In the worst-case scenario, the patient breathes very regularly in phase with a regular re-scanning pattern. In other words, the assumption that the spot displacements in subsequent re-scans are random breaks down. This is most likely the case for volumetric re-scanning, as one complete re-scan for a typical target volume takes 4–6 s on Gantry 2, which is in the range of human breathing. Random pauses or different scanning paths may be a solution to this problem.

Several groups have studied re-scanning by simulations and experiments. Their results are outlined in the rest of this section.

For the treatment of spherical targets with carbon ions, the group at NIRS simulated motion mitigation by re-scanning and gating in a water phantom. Motion was set to the $\sin^4$ function with a period of 3.2 s. They showed that the standard deviation of the dose decreases exponentially with the number of re-scans for phase-controlled re-scanning (PCR), not as the inverse square root as in conventional re-scanning [37]. The idea of PCR is to guarantee that the average motion offsets of each iso-energy slice add up to zero when all re-scans are considered. The re-scans of an iso-energy layer are delivered one after another during a breathing period or, in case of gated treatment, during a gating window. The beam intensity has to be adjusted so that the time to perform the re-scans matches the length of the breathing period or gating window. This seems to work even if the breathing period is not perfectly predictable, as verified by simulations with gating on respiratory motion from real patients.

Experimental verification of these results have been reported by the same group [188]. They irradiated radio-chromic films with a single-energy field for uniform scanning of carbon ions. Sinusoidal motion was in the plane perpendicular to the beam with a peak-to-peak amplitude of 20 mm in both directions and a period of 4 s. Ten times PCR was sufficient to mitigate the interplay effect. In three dimensions, a sphere with 30 mm radius was applied by raster scanning and the dose distributions measured by an array of pin-point ionisation chambers. Motion effects could be reduced by eight times PCR, which performed better than re-scanning without phase control and was found to be robust against changes in the breathing period.

In a later study, they simulated lung tumour treatment on 4D-CT datasets of a lung phantom and a patient[113]. Both layered and volumetric PCR was applied to mitigate the effects of regular motion on a raster scanning system. Changing the synchrotron energy took 150 ms, while smaller steps in energy were achieved by a range shifter in 450 ms. Layered PCR was more stable with respect to motion parameters and less susceptible to interplay between the re-scanning and breathing frequencies. Four times layered PCR lead to acceptable dose homogeneity for motion amplitudes up to 22 mm. The results for the phantom and the patient were comparable.

Several types of delivering the iso-energy layers were compared for proton spot scanning of a cubic target in water [106]. Only scaled re-scanning was considered. Besides layered and volumetric re-scanning, volumetric random re-scanning with random ordering the iso-energy layers was studied, as well as layered time-delay re-scanning with pauses of random length before each re-scan and layered breath-sampling re-scanning, where all re-scans in an iso-energy layer are evenly distributed over a breathing period. Over 30 fractions, layered breath-sampling performed best. With only 5 re-scans to achieve acceptable dose distributions, treatment time was lowest[3]. The results did not

[3]In this study dose distributions were assessed by the mean standard deviation. This value was calculated from the whole dose distribution. This means that blurring at the edges of the dose distribution is included in the results. Blurring is a motion effect ubiquitous in external radiation therapy. Its contribution is of little relevance when studying the interplay effect.

depend on the exponent n of the motion trajectory of the form $\sin^{2n}$.

A similar study at PSI investigated scaled and iso-layered re-scanning for discrete spot scanning and continuous line scanning of uniform spherical target volumes of different sizes [110, 24]. Simulations were calculated in a water phantom with a $\cos^4$ motion trajectory. Line scanning was clearly superior to spot scanning in mitigating motion effects. Not only was the treatment time shorter, but the dose distributions were also more homogeneous for the same re-scanning settings. This benefit increased with the target size. Iso-layered re-scanning performed better than scaled re-scanning, especially at large tumour volumes and low treatment times. Layered line scanning was inferior to layered spot scanning because all re-scans of an iso-energy layer were applied in less than a breathing period for line scanning. Thus, the averaging effect of the motion was not present. In the case of a slow energy change of 1 s, only line scanning was able to perform volumetric re-scanning in an acceptable time. This underlines the importance of a fast energy change for re-scanning. They concluded that tumours moving up to 5 mm could be treated on Gantry 2 either by spot scanning with volumetric, iso-layered re-scanning or by line scanning with volumetric, scaled re-scanning.

For Gantry 2, volumetric, scaled re-scanning was evaluated on 4D-CT data sets of liver patients [193]. Regular, rigid motion was simulated. Re-scanning showed the largest benefits for few fields and for field directions orthogonal to the motion direction, which means that spot scanning is not sensitive along the beam axis, as long as the range does not change. The number of re-scans and fields are complementary. They emphasised the importance of range-adapted target volumes. For multiple fields, moderate motion of up to 6 mm could be treated without re-scanning.

In a similar study, discrete proton spot scanning on lung tumour 4D-CT data sets was simulated for realistic motion, including different magnitudes of baseline shift [114]. The transition time between iso-energy layers was set to 2 s. Dose homogeneity improved thanks to scaled volumetric re-scanning. The effectiveness of re-scanning varied with the plan and the motion model.

3.3. Gating

In gating, the beam is only delivered when a representative measurement of respiratory motion, for example, the height of the abdomen, is in a specified *gating window* of amplitude or phase. This measurement is assumed to be correlated to tumour motion.

The idea of gating seems to have been introduced for scintigraphy of lung and liver [194, 195]. It took a while until it was developed and used clinically in the treatment of cancer, first in proton therapy [172, 179, 196, 162].

The gating window may be determined by fluoroscopy, 4D-CT or 4D-CBCT. Usually, the gating window is placed in the end-exhalation position because there tumour motion is least [131]. As an example from proton therapy of liver tumours, the average residual motion over all breathing cycles was 1.1 ± 0.4 mm in end-exhalation, smaller than in end-inhalation, where 2.7 ± 1.6 mm was measured [197]. In radiotherapy, acceptable dose distributions are achieved with a gating window of 3 mm [198].

At maximum inhalation, there are benefits too, since the lung volume is less dense, so less normal tissue is irradiated [199]. Furthermore, tumours are often more separated from OARs such as the heart [200]. This allows the dose to be increased without risking damage to the OARs [201]. However, in photon therapy of lung tumours, only modest dosimetric differences have been measured [136].

The *duty cycle* is the fraction of the respiratory cycle in which the patient is irradiated. There is always a trade-off between duty cycle and motion mitigation. The shorter the gating window, the less the residual motion during the beam delivery. On the other hand, shorter gating windows also imply a longer treatment time. This significantly reduces tumour motion inside of the gating window and opens up the possibility of margin reduction [202]. Because the baseline of the motion shifts during treatment, for amplitude gating the gating window has to be adjusted for long treatments. Adjustments are also necessary to limit the impact of intrafraction organ deformations [171].

Although gating is a motion mitigation technique, there is a chance that gating even compromises treatment outcome because motion patterns of a patient may be different at CT acquisition and treatment [153]. Also problematic is that internal tumour motion does not necessarily correlate with surrogate motion, as discussed in section 3.1.2.

The problem of residual motion and duty time can be tackled using individualised gating windows [203]. In charged particle therapy, increasing the pencil beam width helps mitigate the interplay between scanning and residual motion [130]. Likewise, gating may be combined with re-scanning [188] or even tracking. Although residual motion and change of shape is reduced by gating of liver tumours [204], for lung tumours residual motion is highly unpredictable [205].

Precise set-up is critical for gating. Even if set-up is based on implanted markers in lung tumours, set-up errors may well be larger than the residual motion inside the gating window [206].

In heavy ion therapy, gating with a duty cycle of 30 % prolonged the treatment time by a factor of 2.5, while the dose distribution approached the static case [192]. With gating, the penumbra was only half of the value for ungated treatment [162]. Gating may not be required in the treatment of pancreatic cancer, although reduction of excessive dose to normal tissue can be achieved [207].

3.4. Breath-hold

Organ motion is minimised by temporarily stopping respiratory motion [200, 196]. This can be achieved either by actively preventing breathing or passively guiding the patient to hold his breath. In the latter case, the patient is usually acoustically or visually guided, for example by displaying a diagram of the breathing cycle.

Gating and breath-hold techniques can be combined such that the patient is guided to hold his breath in the gating window, thus increasing the gating window and also the duty cycle. Using audiovisual feedback [208, 209], treatment times are comparable to conventional ungated therapy [210].

If breath-hold is employed for treatment, the position of the organs may divert from

Author	Treatment site	Duration [s]	Number
Hanley [200]	lung	12–16	10–13
Wong [196]	lung, liver, Hodgkin	max 15–40	2–3 per beam
Dawson [211]	liver	max 20–35	
Balter [212]	liver	max 15–35	3–8
Remouchamps [213]	breast	10–26	4–6
Pedersen [214]	breast (DIBH)	12–48	> 3
	breast (EBH)	12–62	> 3
Koshani [215]	lung	> 20	
McNair [216]	lung	max 15–25	6–13
Wong [217]	lung	17–22	11–16
Peng [218]	lung	3–55	1–2
Hu [219]	gastric	> 15	
Zhong [220]	liver	max 65	

Table 3.1.: Summary of the breath-hold duration and the number of breath-holds required per treatment fraction. DIBH: deep-inspiration breath-hold. EBH: exhalation breath-hold.

their positions for free breathing. Hence, CT images should also be acquired with breath-hold.

Values for the maximum breath-hold duration per patient and the number of required breath-holds per fraction are summarised in table 3.1. While typical breath-hold durations are too short for applying a full field by discrete spot scanning with fast energy change, the delivery of single re-scans should be possible. The corresponding number of breath-holds would then depend on how many re-scans had been selected in treatment planning. If continuous line scanning is considered, a single field may be applied, even with a few re-scans, depending on the target volume.

Results on the reproducibility of the breath-hold position are given in table 3.2 for different breath-hold techniques. Judging from this data, it seems that it is possible to mitigate intra- and inter-breath-hold motion by re-scanning.

3.4.1. Active breath-hold

In *active breath control* (ABC), a spirometer or temperature sensor is used to derive the breathing phase. When a predefined breathing phase is detected, the device stops further breathing for a given time by closing a valve [196]. Patients are trained before treatment with a real-time display of their lung volume and the intended breath-hold duration, e.g., 10 s. The ABC technique is highly reproducible, easy to use and able to reduce margins [196]. A moderate deep inhalation breath-hold at 75 % of the maximum inspiration capacity was shown to result in good reproducibility, patient comfort and dosimetric advantage.

Author	Treatment site	Imaging	Breath-hold	Motion	SI [mm]	AP [mm]	LR [mm]
Hanley [200]	lung	fluoroscopy	DIBH	intra-bh	diaphragm: 1.0 (0.3–2.6), chest wall: 0.6 (0.3–0.8)		
				inter-bh	diaphragm: 2.5 (0.5–4.9), chest wall: 0.9 (0.3–2.0)		
Dawson [211]	liver	radiography, micro-coils	ABC	inter-bh	1.9 (0.5–3.6)	0.6 (0.2–1.4)	0.6 (0.1–1.9)
				interfraction	6.6 (2.3–10.9)	3.3 (1.2–6.5)	3.2 (1.4–5.9)
Remouchamps [213]	breast	EPID	ABC	interfraction	2.7 ± 3.2	2.0 ± 2.1	
Eccles [221]	liver	fluoroscopy	ABC	intra-bh	1.4 (0–3.4 mm)		
		CT		inter-bh	-0.9 ± 1.5	-0.5 ± 1.5	0.2 ± 1.5
Koshani [215]	lung	CT	ABC	inter-bh	0.3 (0.0–3.1)	0.0 (0.0–4.2)	0.2 (0.0–1.7)
			ABC inhale	interfraction	-0.5 (0.0–9.0)	-1.3 (0.4–6.8)	0.3 (0.1–3.8)
			ABC exhale	interfraction	0.2 (0.3–3.3)	-0.2 (0.2–7.4)	-0.7 (0.1–3.6)
Stock [222]	thorax	optical	DIBH	intra-bh	4.0 ± 3.3	5.8 ± 4.6	
	abdomen				2.9 ± 1.9	2.4 ± 1.4	
Glide-Hurst [223]	lung	CT	ABC	inter-bh	1.4 (0.3–1.8)	1.0 (0.2–1.6)	0.6 (0.1–1)
Starkschall [224]	lung	CT	end-inhalation	interfraction	5 ± 4	3 ± 3	3 ± 3
			end-exhalation		2 ± 4	3 ± 3	2 ± 2
Wong [217]	lung (surface)	optical	ABC + DIBH	intra-bh	0.8 ± 0.4	0.6 ± 0.3	0.4 ± 0.3
	lung (tumour)	correlation model	ABC + DIBH	intra-bh	0.7 ± 0.4	0.3 ± 0.1	0.2 ± 0.2
Nakamura [225]	pancreas	CT	end-exhalation	inter-bh	0.1 ± 1.0	0.1 ± 1.2	0.0 ± 1.1
				interfraction	0.3 ± 1.8	0.8 ± 1.8	0.3 ± 2.0
Peng [218]	lung	CBCT	DIBH	inter-bh	1.5 ± 0.8	1.2 ± 0.7	1.0 ± 0.4
Wang [226]	lung	CBCT	ABC	inter-bh	2.0 ± 1.7	1.8 ± 2.9	0.9 ± 1.5
				interfraction	4.8 ± 4.5	2.9 ± 3.5	3.6 ± 2.5
Zhong [220]	liver	fluoroscopy	ABC	intra-bh	0–2	0	0
		CBCT		inter-bh	2.2 ± 3.6	1.5 ± 2.5	0.7 ± 2.3
		CBCT		interfraction	6.8 ± 6.8	3.0 ± 3.6	3.2 ± 3.0

Table 3.2.: Summary of studies into intra- and inter-breath-hold (bh) and interfraction motion. EPID: electronic portal imaging device. ABC: active breath-hold.

It is also possible to gate on an external signal and use the ABC device merely to force a breath-hold during the gating window [223, 219].

A shortcoming of ABC is that many lung cancer patients are not able to hold their breath with sufficient reproducibility To guarantee a good reproducibility of the breath-hold position, which in turn allows margin reduction, is only possible with daily imaging and repositioning of the patient [227].

3.4.2. Voluntary breath-hold

Instead of forcing the patient into a breath-hold as with ABC, voluntary breath-hold techniques have been trialled.

Deep-inhalation breath-hold (DIBH) [200] is motivated by the finding that the normal tissue complication probability (NTCP) of the lungs increases with the proportion of the lungs irradiated if the mean dose is held constant [228]. This means that lowering either the mean dose or the irradiated proportion reduces the complication probability. Delivering dose only in the deep inhalation breathing phase achieves the second approach because in this phase the density of the lungs is minimal while the irradiated volume is unchanged [199]. For example, in one study, lung volume increased in deep inhalation by a factor of about 1.5 [218]. Moreover, tumour movement is reduced with DIBH as in every breath-hold technique. The DIBH technique consists of the following steps: the patient is coached to perform quiet tidal breathing followed by a slow deep inhalation, slow deep exhalation and again a slow deep inhalation until the deep end-inhalation phase is reached. This state is then held for a duration that is comfortable for the patient. The described technique aims at a lung volume of 100 % vital capacity, at which the patient cannot inhale any further, held over a sufficient time in which radiation is applied. The patients receive training in how to correctly perform DIBH.

In one study, chest wall movements were almost twice as large in uncoached DIBH as in free-breathing and four times as large as in gating [229]. During DIBH with visual feedback, single fluctuations in chest wall displacements of more than 10 mm have been seen [230].

To address such problems, DIBH may be gated by external markers [231, 229, 217]. Good correlation between the markers and the tumour motion was found [222], but other studies do not agree [232], see also section 3.1.2. This could be improved by replacing the markers with a 3D surface displacement measurement system [233]. Thereby, reproducibility and stability of DIBH is reduced to less than 1 mm by visual coaching. As a bonus, setup errors are reduced by surface imaging [234, 235].

Even if research indicates advantages for DIBH, treatment time is nearly doubled compared with free breathing [236]. On the other hand, from all the motion mitigation techniques only tracking does not prolong treatment.

Instead of holding their breath in deep inhalation phase, patients can be guided to do so in other phases of the breathing cycle, most beneficially in end-exhalation.

3.5. Tracking

Although tracking is theoretically the best means of reducing intrafraction organ motion, it is technically very demanding. One of the main problems is the delay between registering tumour motion and correcting for this motion. Proof of principle has been established at GSI [118], but so far no treatment centre has implemented tracking clinically for ion therapy.

An example of a tracking system in clinical use is the Cyberknife [237]. The tumour is tracked by a linear accelerator mounted on a robotic arm. A motion model between internal and external motion is built daily before treatment and updated at regular intervals by taking two orthogonal X-ray images. The external motion is acquired optically at a high frequency for predicting the internal motion based on the correlation model.

Because of the inevitable lag in motion compensation systems, prediction algorithms are necessary [238, 239, 240]. Audiovisual feedback to the patients about their breathing facilitates motion prediction by reducing respiratory irregularities [241].

Tracking in ion therapy can in principle be achieved either by adjusting the lateral position and range of the beam, or moving the treatment couch. However, couch tracking lacks the ability to adjust the beam range. Beam tracking is addressed in section 3.5.1 and section 3.5.2 illuminates couch tracking. Table 3.3 gives an overview of the performance of some tracking systems. To interpret the time delay, a simple example should suffice. If we take a sine function as the motion trajectory and set the motion period to 4 s, then the uncompensated motion due to a time delay of 100 ms is in the best case 1 % of the peak-to-peak amplitude and in the worst case 31 %.

3.5.1. Beam tracking

A scanned ion beam can follow the target laterally at a high velocity so that the tracking quality depends only on the quality and latency of the imaging system and the necessary image processing. Motion in range is followed by adjusting the beam energy. Note that motion along the beam direction is not the same as motion in range. For instance, if the patient shifts by a millimetre on the beam axis, the water-equivalent range (WER) of the tumour might well stay the same. To quench enthusiasm a little, quality assurance for tracking is difficult. Possibly, range verification with prompt gamma cameras or PET could prove advantageous [254].

Much research in beam tracking has been conducted at GSI with their fast raster scanning system. Simulations showed that if tracking with a precision of 2 mm is possible, only 3 % lower dose homogeneity than for static irradiation would be expected [112]. This is in line with an earlier study which established that the dose homogeneity with tracking was better than 95 % [255].

Geometric phantom experiments have confirmed this. Dose homogeneity was recovered from 90 % for motion without tracking to 97 % when tracking was enabled [256]. Relative dose differences between the static and tracked experiments of only 1 ± 2 % and 0.3 ± 1.5 %, depending on the study, were observed and dose gradients could be preserved [118, 256].

Author	Method	Delay [ms]	Mean error [mm]
D'Souza [242]	couch	67	< 3
Bert [118]	beam	lateral 1, range 25	
Qiu [243]	couch	67–1000	2.0 ± 2.9
Wilbert [244]	couch	73[a]	0.36 ± 0.12
Hoogeman [245]	robotic linac	115–193	1.9 SI and LR, 2.5 AP
Saito [246]	beam	lateral 1, range 27[b]	lateral 0.04±0.16, range 1.08
Buzurovic [247, 248]	couch	145	0.14 ± 0.2 SI, 0.18 ± 0.2 AP, 0.12 ± 0.2 LR
Haas [249]	couch	420	0.4–1.5
Lee [250]	couch	250	5.8 ± 3.4 SI, 7.5 ± 5.7 AP, 6.1 ± 3.5 LR
Menten [251]	couch	160	2.2 AP, 1.0 LR
Seregni [252]	beam		SSM 0.34±0.25, ANN 0.27± 0.55[c]
Wilbert [253]	couch	700[d]	0.01 ± 0.55 AP

Table 3.3.: Time delay and mean tracking error for motion tracking. For the tracking error, a single number designates the root mean square error (RMSE), while two numbers give the mean and the standard deviation. The studies of D'Souza and Qiu are based on simulations, all other studies report on experiments. [a]Not included is the delay of imaging of 501 ± 143 ms. [b]A shift of 5 mm took 16 ± 2 ms. A constant delay of 11 ± 2 ms was observed. [c]The two correlation models were State Space Model (SSM) and Artifical Neural Network (ANN). [d]The delay of imaging is included.

To enable tracking in depth, which is necessary because of the sensitivity of protons to tissue density and beam path fluctuations [116], wedges were successfully used to quickly change the beam energy [36, 119, 256]. The Bragg peak position could be recovered within 0.23 mm WER. Its shape and height was unaltered with tracking, while it disintegrated completely without motion compensation.

For Gantry 2 at PSI, a simulation study compared tracking of simple target volumes in digital phantoms with and without relative motion of a density inhomogeneity, by way of a rib proximal to the target [257]. In the case of homogeneous density, perfect tracking could reproduce the static case. Considering the case of inhomogeneous density, D_5 - D_{95} as defined in section 4.4 was only 3.4 % for a target motion amplitude of 15 mm and perfect tracking. This means that perfect tracking cannot completely mitigate target motion. Re-scanning 8 times without tracking showed the best results.

A straight-forward application of tracking for ion therapy works only for translational motion. In the case of rotations or deformations, even if tracked beams deliver the dose at the correct position in the Bragg peak, the plateau dose is applied to the wrong anatomical structures. To tackle this problem, *real-time dose compensation beam tracking* (RDBT) has been introduced [190, 258]. The idea is to keep track of the delivered dose per voxel in real time by monitoring intrafraction motion and appropriate re-evaluation of the spot weights. The target volume is scanned starting from the highest energy. Under-dosages in certain voxels are corrected for by increasing the weight of the corresponding spot. Over-dosages cannot be compensated for completely. In any case, for RDBT it is assumed that the 4D-CT data set of the patient is still valid at the treatment, which limits the best performance that could theoretically be achieved by this method. Experiments with an ionisation chamber (IC) array showed a reduction in under- and over-dose when switching from naive beam tracking to RDBT [258]. Robustness against motion starting phase also increased.

Taking validation of tracking a step further, experiments with an anthropomorphic respiratory phantom [259] were conducted at GSI [252]. Markers on the phantom were surveyed by an optical system. While the total dose to the target was reduced by 9.5 % due to motion, tracking could limit this difference to 0.6 % for motion including phase shifts and 2.3 % when baseline drifts were added to the trajectory. Phase shifts posed a problem for the correlation models between external and internal motion. In this case, tracking results were not statistically significantly better than if no motion mitigation was applied. Baseline drift also reduced the accuracy of tracking.

3.5.2. Couch tracking

Modern treatment couches are highly responsive and accurate systems. They are candidates for the widespread introduction of tracking, at least for photons, where motion tracking with the couch performs similarly to tracking with a multi-leaf collimator (MLC), although it is more robust against different motion trajectories [251].

Appropriate immobilisation devices have to be employed for couch tracking because patients may compensate for the motion when the treatment couch is moved [260]. Nausea seems not to pose a problem, although people who are prone to nausea while

travelling might experience slight discomfort [261].

Hexapod treatment couches (Medical Intelligence GmbH, Schwabmünchen, Germany) have been evaluated in photon radiotherapy [262, 242]. With these couches, displacements of up to 3 cm are possible. Due to technical limitations of the couch, realistic motion periods could not be compensated for at the time of that study. The maximum speed of the table was less than 1 $^{cm}/_{s}$ per axis, while a maximal lung tumour speed of over 7 $^{cm}/_{s}$ has been reported [55]. Given a sufficiently powerful couch with a dead time below 100 ms, simulations suggested that the residual motion is sufficiently suppressed also for realistic motion periods [242].

Instead of tracking only optical markers on the surface, an MV fluoroscopy system has been added to the Hexapod tracking system [244]. This helps in compensating drift of lung tumours. Residual motion is reduced by as much as 65 %.

Respiratory motion with a mean period of 2.6 ± 0.4 s could be tracked in a later study [260]. Pass rates on a 2 %, 2 mm γ index test were above 98 % for the average of 15 patient trajectories [253].

Dedicated prediction algorithms based on least squares reduce the tracking error by more than 60 % with respect to standard multiple linear regression [243].

Tracking has also been implemented for an Elekta Precise Table (ELEKTA Ltd., Crawley, UK). Maximum dose deviations of 1.2 % on the central axis and 2.4 % in high-dose regions were measured for IMRT plans [248]. Differences between static and tracking dose distributions were mostly due to dose blurring at the edges [249].

Slow tracking has been studied with a TrueBeam system (Varian Medical Systems, Palo Alto, CA). While permanently monitoring patient motion, every 10 s the predicted baseline drift is corrected [263]. Initial experiments with a motion phantom were successful: the root mean square error (RMSE) was more than halved.

3.6. Conclusion

We have seen in this chapter that motion mitigation is an intricate problem. In principle, tracking is the way to go, but there are several open questions to this approach. How can treatment with tracking be verified? How can the correlation between tumour motion and motion surrogate be modelled with minimum additional dose and how can this correlation model be verified during treatment? How should we proceed in the case of over-dosage in RDBT?

At PSI, we decided to start with re-scanning and gating, as these techniques are easier to implement. In the context of this thesis, breath-hold and gating are treated as the same motion mitigation method.

Re-scanning is arguably the most robust method, because no information about the actual organ motion during treatment is required. On the other hand, re-scanning also leads to the largest volume of irradiated healthy tissue, since motion effects are averaged out rather than prevented. There is a continuous spectrum of possibilities to apply re-scanning. Therefore, an important goal was the identification of the most effective implementation, as presented in chapter 5. The conclusions are drawn here solely for

Gantry 2 and might not be applicable to other systems.

Gating shares with tracking the fact that the motion mitigation performance depends on the ability to precisely measure tumour motion. While this is an interesting subject, in this thesis the focus was on the relative benefits of gating and the combination of gating and re-scanning for different target volumes and motion trajectories. The results are presented in chapter 6. No baseline drift of the tumour motion was applied as this could be corrected for by slow tracking. The idea here is to detect the baseline drift by our X-ray BEV system and subsequently offset the patient table at an interval of, e.g., 30 s.

As discussed in section 3.2, although studies showed that the PCR method was superior to other re-scanning methods, it was not used in the combination of gating and re-scanning, because assumptions on the breathing period would have to be made.

Gating and re-scanning both lead to a longer treatment time. What is more, there is a technical limit to the possible number of re-scans in discrete scanning. A solution to these problems offers the technique of continuous scanning, which allows very fast scanning of iso-energy layers. The benefits of this technique are reported in chapter 7.

4. Materials and methods

As a key part of this thesis, equipment and processes for the experimental evaluation of motion mitigation techniques have been developed. More precisely, the goal was to introduce the analogue of 4D dose calculations for measurements in scanned proton therapy. This chapter gives an overview of the tools and methods that were essential to obtaining the results presented in the following chapters.

The purpose of section 4.1 is to become acquainted with the treatment planning procedure specific to Gantry 2 and for all delivery methods that have been studied in this work. This is not an introduction to the operation of a treatment planning system (TPS) but rather a hands-on approach to creating plans for Gantry 2.

The same plans that have been applied on Gantry 2 in the course of the measurements have also been simulated with the same motion parameters. To this end, the timing of the dose delivery has been modelled. This allowed a direct comparison of the results expected from simulations and the results actually measured. The simulation engine is covered in detail in section 4.1.6. Its application to the prediction of our measurements is discussed in section 4.2.

In order to experimentally verify the effectiveness of motion mitigation techniques, a dosimetry device has been developed and combined with a commercial respiratory motion platform. The aim was to construct a light-weight device with a high spatial resolution. The restriction on a small weight was due to the limitations of the respiratory motion platform. The components of this measurement set-up is described in section 4.3.

The approach to data analysis is outlined at the end of this chapter in section 4.4. Although the results from simulations and experiments were processed by two different tool chains, data analysis was implemented as similarly as possible in both tool chains.

4.1. Treatment planning

No treatment planning system (TPS) was available for Gantry 2 at the outset of this work. A software program was developed by Zenklusen [24] for generating plans for geometric target volumes such as cubes, ellipsoids and cylinders. This program has been modified and enhanced. For example, the generation of treatment plans for patient target volumes were added. The target volumes can be imported from the TPS of Gantry 1. The software is restricted to a single homogeneous medium. Further details of this program are discussed in section 4.2.

4.1.1. Beam model

The basic ingredient to treatment planning for Gantry 2 is the three-dimensional beam model [10]. It is described by a two-dimensional Gaussian distribution in the lateral plane and a physical model for the integral depth-dose curve. The physical model is fitted to depth-dose curves measured by ionisation chambers. The width of the Gaussian is assumed to be the same in both directions and has been taken from measurements, as well. Hence, spots are assumed to be circular in the lateral plane.

Neutrons are not included in the model. Some fraction of the charged products from nuclear interactions are distributed linearly between the point of interaction and the end of range. The rest is deposited locally. Nuclear interaction cross sections of protons for hydrogen and oxygen are taken from the literature and are parametrised. The nuclear interactions add a shallower Gaussian to the lateral beam profile. This so-called *halo effect* is not taken into account in the beam model. The reason is that for a target volume the effect of the beam halo is mainly a scaling of the absolute dose. Therefore, as long as it is not required to predict the absolute dose by the dose calculation, the halo effect is neglected for the sake of fast calculation.

4.1.2. Spread-out Bragg peak

At the heart of proton therapy lies the art of generating a volume of homogeneous dose with Bragg peaks. To this end, proton beams of different energies, i.e., ranges, and weights are superimposed to yield a flat part in the summed depth-line. This part is called *spread-out Bragg peak* (SOBP), see figure 4.1.

There are analytical formulae for creating SOBPs, as mentioned in section 1.1, but an optimisation procedure is more flexible and gives better results. In our case, we decided to use an implementation of the simplex algorithm. The most distal Bragg peak, i.e., the one with the largest range, always has the highest weight, because the dose deposited by this spot also contributes to the dose of all other, more proximal, spots. Generally, the weights increase with depth, but there can be exceptions to this.

For all particles that have an RBE differing from one, it is advisable to optimise the SOBP not for physical dose homogeneity but for homogeneity of biological effect. This is commonplace in heavy ion therapy [264], yet not in proton therapy, because the RBE is assumed to be fixed to the value 1.1, as discussed in section 1.1.

A certain role is played by the separation in depth of adjacent Bragg peaks. The separation readily translates to a difference in range and energy. The closer the Bragg peaks, the easier it is for the optimisation algorithm to end up with a homogeneous dose distribution. In general, smaller separations are associated with less interplay effect [130]. In addition to the obvious choice of a fixed separation, it can be set to increase linearly with depth or as a function of the Bragg peak width in depth [265]. This is useful because in depth, the width of the Bragg peak decreases with energy due to energy straggling. In this work, all SOBP have been created with linearly increasing energy steps.

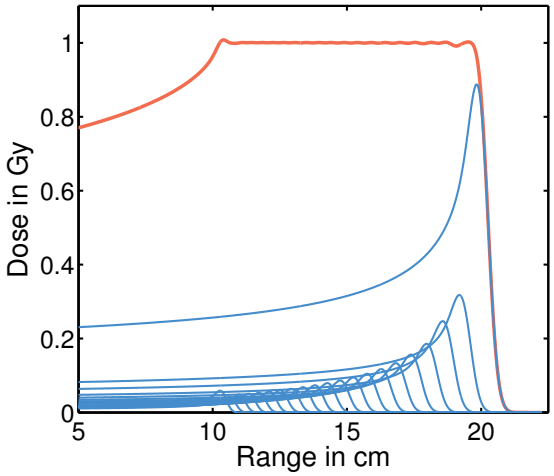

Figure 4.1.: Composing a spread-out Bragg peak out of many weighted proton beams at different energies. More distal beams have higher weights (deposit more protons) because proximal regions receive dose already from the plateau of these distal beams. The spacing in range of the shown SOBP is linearly increasing with range.

4.1.3. Discrete spot scanning

This section deals with the generation of a treatment plan for discrete spot scanning based on a CTV and a prescribed dose as defined by a physician. The CTV can either be a geometric target volume or a target volume from a patient case. This is the volume that has to be irradiated with the dose prescribed by the physician.

In the first step, a grid is set up within the treatment volume, whereby the grid spacings correspond to the spot spacings. If the spacing in depth has not been chosen to be constant, a representative fixed value is taken. For each lateral grid node, an SOBP is generated between the minimal and maximal depth, resulting in a list of spots. Each spot is assigned a T- and a U-coordinate, an energy corresponding to the range of the Bragg peak and a weight in the form of a number of protons necessary to deliver the prescribed dose.

The CTV is expanded to an ITV so that the tumour always receives the prescribed dose. Because only motion along a single direction is applied, for the geometric target volumes, the CTV is expanded only in the direction of motion. For the patient target volumes, the situation is slightly different because no ITV had been defined in the original treatment plan. Instead, an isotropic margin had been added to the CTV, resulting in the PTV. This PTV was large enough to cover the CTV in all motion phases, so no additional ITV had to be defined. The volume definitions are shown in figure 4.2b.

At this point, re-scanning can be performed. The resulting spot list is sorted so that for each energy, a meander path is scanned with the primary scanning direction in T, because scanning in T is faster than in U. These energy layers are subsequently sorted.

The spot list is converted to a *steering file*, from physical quantities, such as number of

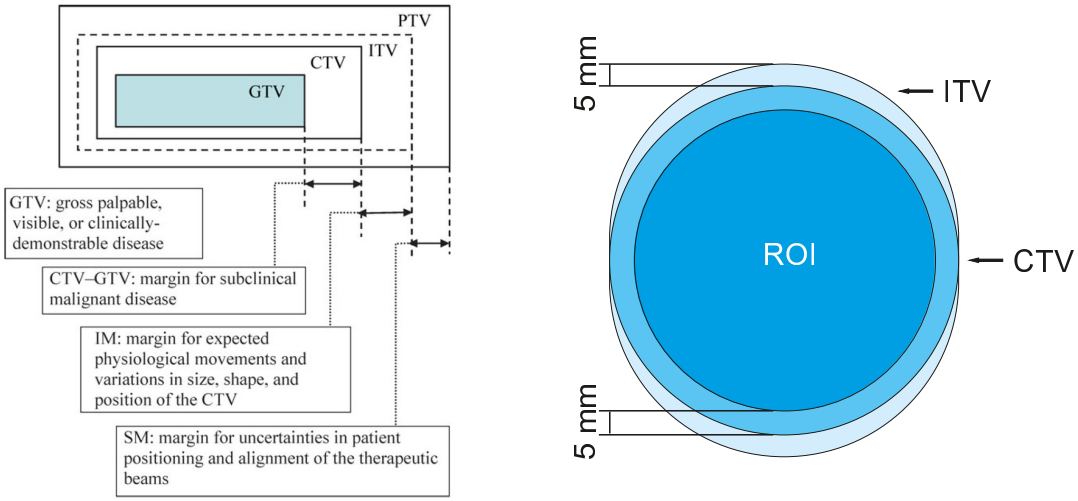

(a) (b)

Figure 4.2.: Definition of target volumes (a) by the ICRU [266] and (b) as interpreted in this thesis. Shown is the spherical target volume with an anisotropic extension of the CTV to form the ITV. The ITV for patient target volumes is isotropic because this is what has been defined by the physician.

protons, energy and positions in cm to quantities understood by Gantry 2, such as MU or electrical current for the sweeper magnets. Because the current induced by protons in an ionisation chamber decreases with energy, the conversion from protons to MU is energy-dependent.

The *tunes*, i.e., the settings of the beam line, vary with energy. This information is stored in a separate file, the *tune file*. It contains, for all energies that are used in the corresponding steering file, the position of the wedges of the energy degrader, the currents of all the magnets of the beam line, including the magnets mounted directly on Gantry 2, and the settings of COMET that control the range of available beam intensities.

4.1.4. Continuous line scanning

The starting point of treatment planning for continuous line scanning is a spot list. It is divided into rows of all spots with the same energy and the same secondary scanning coordinate U, see figure 4.3. The spot copies obtained by re-scanning end up in different rows because they are not applied directly after each other.

A convolution of a row with a suitable kernel yields a *line* along the T axis. Such a line represents the smallest entity of dose delivery for line scanning. It contains the T-coordinate and the beam intensity as a function of time. A line is really a convolution of a set of delta functions at the positions of the spots, scaled by the spot weights. As a

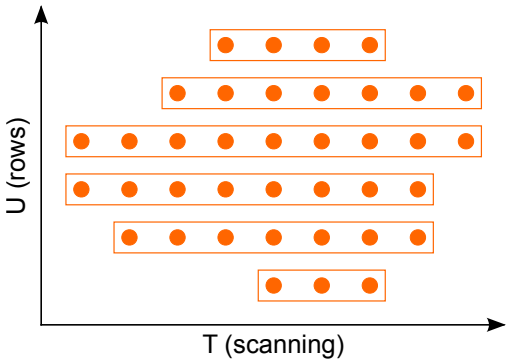

Figure 4.3.: Division of spots of an iso-energy layer into rows for each U coordinate.

result, the convolution is trivial, because it just sums scaled kernels. In this thesis, the simplest kernel has been chosen, the rectangular kernel with support Δ [267]:

$$k(x) = \frac{1}{2\Delta} \left(\operatorname{sgn}(x + \Delta/2) - \operatorname{sgn}(x - \Delta/2) \right).$$

with $\operatorname{sgn}(x)$ the sign function ($\operatorname{sgn}(0) = 0$).
For a line $D(x)$ with spot weights w_i and the spot separation Δ, we get:

$$\begin{aligned} D(x) &= \sum_i \Delta w_i k(x - x_i) \\ &= \begin{cases} w_i & \text{if } x \in (x_i - \Delta/2, x_i + \Delta/2) \\ \frac{w_i + w_{i+1}}{2} & \text{if } x = x_i + \Delta/2 \\ 0 & \text{else} \end{cases} \end{aligned}$$

where the normalisation factor is equal to the spot separation. This is shown in figure 4.4a.

It has been shown that using the kernel that should give best results, a sinc kernel[1], is not appropriate because it asks for negative dose to be delivered, which is impossible. Setting all negative values to zero is inferior to just using a simple rectangular or triangular kernel, for instance [267]. Better results are achieved by optimising the weights. It is beyond the scope of this thesis to implement this method. A comparison of lines obtained by different simple kernels has been undertaken *in silico*. The rectangular kernel proved to be the best.

In practice, when a line is actually applied on a gantry, it is convolved with the beam model, see figure 4.4b. In our case, this is an energy- and depth-dependent Gaussian kernel. It is the ultimate goal to deliver the same dose distribution with line scanning than with spot scanning. For comparing the effect of the different convolution kernels,

[1]The unnormalised sinc function is given by $\operatorname{sinc}(x) = \frac{\sin(x)}{x}$.

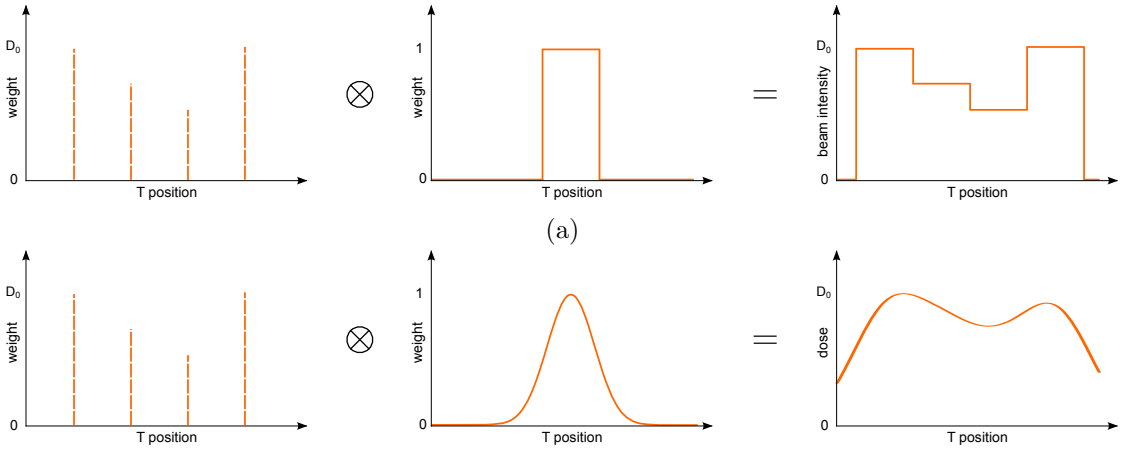

(a)

(b)

Figure 4.4.: Conversion of a row of spots with different weights. In (a), the ideal dose profile is obtained by convolving the spot weights with a rectangular kernel. This profile is the input to the control loop of the beam intensity. The actual dose distribution is shown in (b). Here, the rectangular kernel is first convolved with the Gaussian beam model.

only the resulting line after further convolving by the beam model is of interest, smearing out the differences between the kernels.

In the simple case where a constant dose D_0 is applied from $-L/2$ to $L/2$, the convolution by the beam model leads to the integration of a Gaussian, corresponding to the beam applied at every position along the profile for an infinitesimal time:

$$\begin{aligned} D_{\text{applied}}(x) &= \frac{1}{L}\int_{-\infty}^{\infty} D(y)\frac{1}{\sigma\sqrt{2\pi}}e^{-\frac{1}{2}(x-y)^2/\sigma^2}dy \\ &= \frac{D_0}{L}\int_{-L/2}^{L/2}\frac{1}{\sigma\sqrt{2\pi}}e^{-\frac{1}{2}(x-y)^2/\sigma^2}dy \end{aligned}$$

The term $1/L$ is a normalisation factor. Substituting $x-y/\sigma\sqrt{2}$ by t gives

$$\begin{aligned} D_{\text{applied}}(x) &= \frac{D_0}{L}\frac{1}{\sigma\sqrt{2\pi}}\sigma\sqrt{2}\int_{x-L/2/\sigma\sqrt{2}}^{x+L/2/\sigma\sqrt{2}} e^{-t^2}dt \\ &= \frac{D_0}{L}\frac{1}{\sqrt{\pi}}\left(\int_0^{L/2-x/\sigma\sqrt{2}} e^{-t^2}dt + \int_0^{L/2+x/\sigma\sqrt{2}} e^{-t^2}dt\right) \end{aligned}$$

Modality	Penumbra
Single spot	$\sigma\left(\sqrt{-2\ln 0.2}-\sqrt{-2\ln 0.8}\right)\approx 1.13\sigma$
Spot scanning	$1.68\sqrt{\sigma^2-\lambda^2/12}=1.61\sigma$ for $\lambda=\sigma$
Line scanning	$\sqrt{2}\left(\mathrm{erf}^{-1}(0.6)-\mathrm{erf}^{-1}(-0.6)\right)\approx 1.68\sigma$

Table 4.1.: Exact and approximate formulae for calculating the penumbra from the beam width σ for different treatment modalities. λ is the distance between spots.

and using the definition of the error function[2] we have

$$\begin{aligned} D_{\text{applied}}(x) &= \frac{D_0}{L}\frac{1}{\sqrt{\pi}}\frac{\sqrt{\pi}}{2}\left(\mathrm{erf}\left(\frac{L/2-x}{\sigma\sqrt{2}}\right)+\mathrm{erf}\left(\frac{L/2+x}{\sigma\sqrt{2}}\right)\right) \\ &= \frac{D_0}{2L}\left(\mathrm{erf}\left(\frac{L/2-x}{\sigma\sqrt{2}}\right)+\mathrm{erf}\left(\frac{L/2+x}{\sigma\sqrt{2}}\right)\right) \end{aligned}$$

As a result, the line itself is unaltered except for the penumbra[3], which is shaped like an error function. This is the worst case for the penumbra, whereas the smallest penumbra is achieved by a single spot and shaped like a Gaussian [43]. The penumbra for spot scanning is larger than for a single spot, but smaller than for line scanning and depends on the spot separation. In a word, the penumbra for line scanning is larger than for spot scanning. In table 4.1 theoretical predictions for the different penumbrae are summarised.

In the following, the implementation of line scanning on Gantry 2 is discussed. After the conversion of spots to lines, all lines with the same energy are connected to a *path* and stored as a set of tables indicating the position in T and U and the beam intensity. In the *time-driven* mode, each table holds the set point of the device and the time when this set point should be achieved. By contrast, in the *dose-driven* mode the time is replaced by the dose that should be achieved when the device is at the given set-point. Because the beam intensity is practically constant, these two modes are completely exchangeable. In fact, the standard deviation of the beam intensity is about 2 % at a time scale of 200 μs. In this work, only the time-driven mode has been studied.

Similar to spot scanning, the path has to be converted to a format fit for application on Gantry 2. The delivery tables of the path are prepared so that they can be loaded into a field-programmable gate array (FPGA). This device can store up to 512 entries per table. If the tables are longer than this limit, they have to be split. Loading the tables into the FPGA takes a couple of ms.

The FPGA interpolates the delivery tables at 100 kHz. This has to be taken into account when converting a path to a set of tables as follows. If the dose profile is not

[2]The error function is defined as $\mathrm{erf}(x)=\frac{2}{\sqrt{\pi}}\int_0^x e^{-t^2}\,\mathrm{d}t$.

[3]In this thesis, the penumbra is defined as the distance between the 20 % and 80 % iso-dose curves.

continuous at a certain position[4], the deflector plate value has to be set just before and just after this position[5]. Otherwise, the interpolation by the FPGA would set the deflector plate values according to a linear function between the preceding and the following table entries, which are probably many ms apart.

A detail is the time delay of the sweeper magnets with respect to the deflector plate voltage. This parameter has been measured in dedicated experiments. It takes into account all communication and set-up delays. With 200 μs a good synchronisation between sweeper and beam current was observed. The time entries in the deflector plate table have to be shifted accordingly.

4.1.5. Simulated scattering

We have seen in section 1.2.3 that in simulated scattering, a field is applied by continuous line scanning with the help of a collimator and a compensator. While the collimator blocks dose lateral to the target volume, the compensator shapes the distal edge of the field.

Treatment planning for this modality starts with a spot list for a uniform field whose dose distribution has to be reproduced as accurately as possible by simulated scattering.

First, a cuboidal spot list is generated as the envelope of the original spot list. Hence, for every spot in the original spot list there is a rectangular iso-energy layer of spots in the cuboidal spot list. The lateral size of all these layers is identical and large enough so that the original spot list is contained in it, i.e., it is a subset of the cuboidal spot list.

While iterating through this cuboid, it is checked whether the current spot would add dose inside the target volume if it were applied using the compensator. At the end of this step, the most distal layer stretches over the whole lateral extent of the field, while proximal layers are more and more shrunk to reduce dose delivered to healthy tissue proximal to the target volume. This procedure is shown in figure 4.5.

As a final step, the spot list is converted to lines. All lines of the same iso-energy layer share the same weight. The lines can be extended in both directions across the collimator to achieve a better homogeneity. Possible causes for inhomogeneities include oscillations in the monitor unit rate as a result of the control loop and the delay of the sweeper magnet in reaching the nominal scanning velocity.

For target volumes of convex shape, the single iso-energy layers are homogeneous in dose. This renders it easier to control the beam intensity. On the other hand, for concave target volumes or if an inhomogeneous dose distribution is required, the dose rate has to be modulated during the delivery of an iso-energy layer. It is more challenging to reproduce scattering or spot scanning fields under these circumstances, especially at fast scanning speeds or, equivalently, large numbers of re-scans. One reason for this is the time delay in changing the beam intensity and the sweeper magnet speed. Oscillations of the beam intensity due to the imperfect behaviour of the control loop, caused partly by the time delay of the deflector plate, also contribute.

[4]When using rectangular or triangular kernels, this is unavoidable.

[5]The separation between these two nodes should be on the order of the sampling interval of the FPGA. We have taken twice this value, i.e., 20 μs

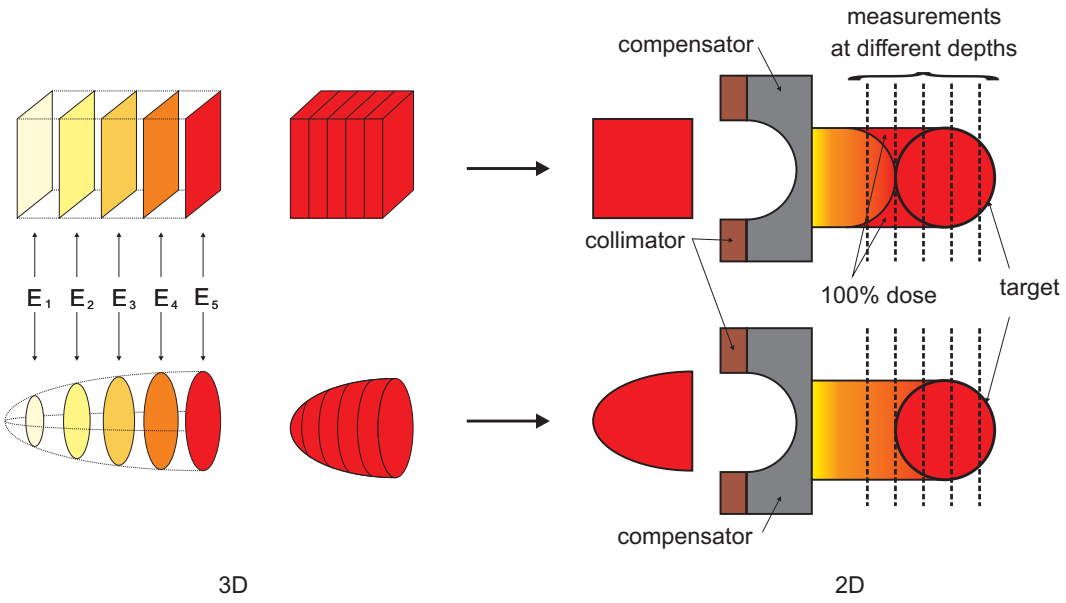

Figure 4.5.: Principle of creating treatment plans for simulated scattering by appropriately shrinking a cuboid field. Image courtesy of [44].

4.1.6. Dose calculation

For discrete spot scanning, calculating the dose corresponding to a treatment plan involves superimposing the contributions of all the spots. Since in this thesis we restrict ourselves to water in a rectangular phantom, nothing more is required than taking proton beams of different energies and lateral positions, weighting them according to the spot weights and summing them up in a dose grid. An example for a single row of five spots is shown in figure 4.6a.

In the case of continuous line scanning, the dose calculation differs along the primary scanning direction T and the secondary scanning direction U. Along the U axis, dose calculation is analogous to the one of spot scanning. Two approaches are possible for the dose calculation along the T axis. Remember that a line for line scanning is obtained by convolving the spot positions by a rectangular kernel, see section 4.1.4.

The first, *simple*, approach just takes all the lines corresponding to the single spots, merges adjacent lines with the same weight, models the penumbra of each of these lines by an error function depending on the beam width and adds them up. This is shown in figure 4.6b.

The second, *full*, approach is very similar to the dose calculation for spot scanning, but many additional nodes are inserted between the original spot positions for the calculation to approach the physical process of a continuously moving spot, see figure 4.6c.

Full dose calculation lends itself better to complicated dose profiles, because the fidelity of the dose calculation can be increased by using more calculation nodes. Interpolation yields the weights of these additional nodes. The disadvantage is that it takes much

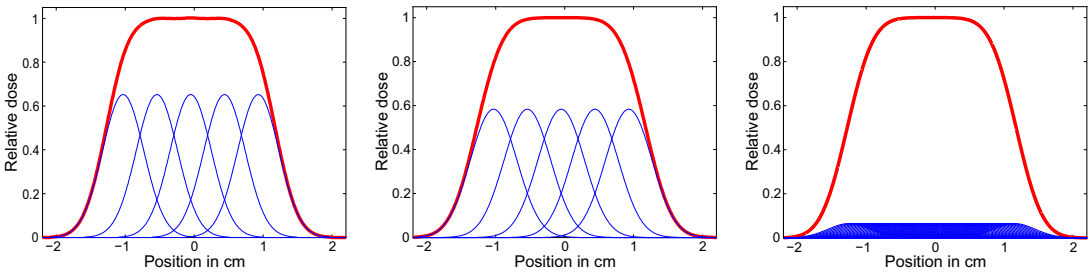

(a) spot scanning (b) line scanning, simple calculation (c) line scanning, full calculation

Figure 4.6.: Comparison of dose calculation methods for spot and line scanning for a line of five spots with unit weight.

more time to calculate than for the simple method.

Both methods can be combined. While the dose contribution of each node is still modelled by the error function, additional nodes between the spot positions are inserted.

The two-dimensional Gaussian is restricted to $3.5\,\sigma$, where σ is the Gaussian beam width at the end of the Bragg peak range. Here, σ attains its maximum value. While small differences can be seen when using a larger width, as shown in figure 4.7a, calculation time increases by about 30 % for $4\,\sigma$, see figure 4.7b. Taking into account that most dose distributions have been calculated for motion, this error is negligible. Outside this area, the dose contribution is set to zero. The grid spacing of the dose grid is usually set to 2 mm as this is a common resolution of CT data. Dose calculation is also considerably faster for this spacing than for 1 mm or less.

An energy-dependent Gaussian beam width was implemented. The values plotted in figure 4.7c were measured on Gantry 2 in steps of 10 MeV and linearly interpolated.

By using look-up tables for the slow operations exp and erf, the dose calculation could be sped up by a factor of two. The exponential function is cut off at $x = -20$ and set to zero. Likewise, the error function is cut off at $|x| > 4$ and set to ± 1.

The dose calculation for simulated scattering is a special case of the dose calculation for line scanning. The only difference is the simulation of the collimator and compensator. The collimator is implemented as a part of the compensator with the water-equivalent thickness (WET) set to a large enough number. Beam broadening due to MCS in the collimator is taken into account [268]. Both beam size and shift in WER in the collimator are calculated for a set of incident beam energies. The WET is calculated analytically with the help of range and energy look-up tables. The energy dependence of the range shift with initial energy is due to the proton mass stopping power ratio between a material and water [269]. For many biological tissues, this ratio depends only weakly on the energy. Common detectors for dosimetry may show larger deviations [270].

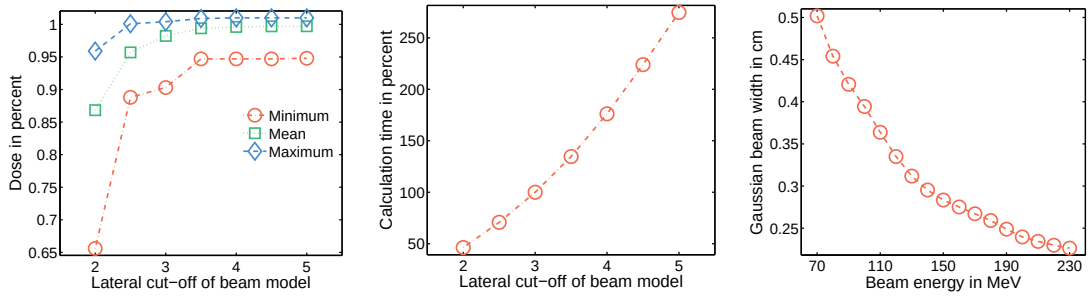

(a) (b) (c)

Figure 4.7.: Comparison of different cut-offs on the Gaussian beam model in the lateral plane in terms of (a) dose and (b) computation time. The cut-off is given as multiples of the Gaussian beam width. The dependency of the Gaussian beam width on the beam energy is plotted (c) in air and at the iso-centre of Gantry 2.

4.1.7. Dose optimisation

For cubic and even for spherical target volumes, fairly homogeneous dose distributions conforming to the target contour are obtained by setting the spot weights in a way to create a homogeneous SOBP at each lateral position in the spot grid. This approach breaks down for more complicated target volumes. The irradiated volume is typically much larger than necessary. As a remedy, the spot weights are optimised so as to minimise the difference between the dose prescription and the actual dose distribution. In general, dose to OARs has to be minimised as well, but this is not taken into account in the following.

The optimisation algorithm of the PSI TPS was implemented in our software package [271]. This is a gradient-based method. Without going into details here, the main benefit of such a method is its speed. In each iteration of the algorithm, the new spot weights are directly calculated from the previous weights. This is in sharp contrast with more sophisticated but slower algorithms, where several sets of spot weights are tested in each iteration and the best set chosen. The goodness of a set of spot weights is determined by a cost function. In our case, the cost function to be minimised is defined as

$$\chi^2 = \sum_{i=1}^{N} g_i^2 (P_i - D_i)^2$$

where N is the number of voxels of the dose grid, P is the dose prescription, D is the actual dose and g is the importance factor. The importance factor determines how much of the dose difference in a voxel contributes to the cost function. The weight of the jth spot in the kth iteration of the optimisation algorithm are updated according to

$$\omega_{j,k} = \omega_{j,k-1} \frac{\sum_{i=1}^{N} g_i^2 d_{i,j}^2 \frac{P_i}{D_i}}{\sum_{i=1}^{N} g_i^2 d_{i,j}^2}$$

where $d_{i,j}$ is the unweighted contribution of the jth spot to the dose in the ith voxel.

Generally speaking, gradient-based optimisation algorithms follow in the direction of steepest decent in the space of spot weights, as expressed by the gradient of the cost function. If the gradient becomes small enough, the algorithm stops, as the value of the cost function cannot be reduced by a significant amount. As a result, the cost function rapidly converges to one of the local minima near the starting point. Unfortunately, if it attains the global minimum for an entirely different set of spot weights, the solution is not optimal.

One way to circumvent this problem is to just use a slower, but more robust algorithm that finds the global minimum for whatever starting point. Alternatively, the starting point is varied and the best solution singled out, which might or might not be the optimal solution.

4.2. Simulations

The dose calculation has been combined with a motion model to predict the effect of target motion and motion mitigation techniques on dose distributions. As the motion model, a one-dimensional motion based on $\cos^4$ was chosen [272]. Each simulation was started at 36 different phases.

If the spacing between nodes for continuous line scanning were too large, the motion effect could not be calculated correctly. The node spacing was adjusted so that the motion model was sampled in steps of not more than the grid size of the dose grid, which is 2 mm. The delivery tables are defined in terms of time. Hence, the node spacing had to be converted to time steps. The maximum derivative of the motion model was taken for this conversion, so the average effective spatial node spacing was much less than 2 mm.

The target volumes were defined as in section 4.1.3. The dose distributions calculated with motion were compared with a reference distribution without motion. The spacing of the spots was always set to 5 mm laterally and 4.5 mm in range.

The necessity of including an ITV means that rescanning invariably increases the volume of treated normal tissue. This is the reason why we limited our studies to 10 mm tumour motion. Larger motion should be addressed by other motion mitigation techniques such as gating, breath-hold or tracking.

All the simulations have been run on the Merlin4 linux cluster at PSI. The output data was stored in Hierarchical Data Format version 5 (HDF5) files [273].

For comparisons between simulated and measured dose distributions, quenching was taken into account, which is explained in section 4.3.2.

4.3. Measurement set-up

To capture dose distributions of a moving target, as a part of this thesis, we have developed and characterised an in-house system comprised of a scintillating screen, a mirror and a charge-coupled device (CCD) camera [274, 275]). The camera is positioned at a distance of about 70 cm from the proton beam to limit radiation damage to the CCD chip and electronics, as shown in figure 4.8. The mirror is at an angle of 45 ° with respect to the scintillating screen. The CCD camera records the light that is emitted by the scintillating screen during irradiation.

The equipment is placed in a light-tight box to eliminate ambient light. As a substitute for water, poly(methyl methacrylate) (PMMA) blocks are placed on the scintillating screen so as to measure the light output at the required WER. This box was attached to a commercial motion platform.

The components of this set-up are described in detail in the following sections. The emphasis of the design was on a light-weight and compact CCD box because of the restrictions of the motion platform. This implied also a limit on the length of the CCD box, which in turn determined the length of the optical path from the scintillating screen to the CCD camera. This distance is tied to the optical performance of the whole system, see section 4.3.3. The small weight of both the CCD box and the motion platform also simplified the handling and setting up of the measurement equipment.

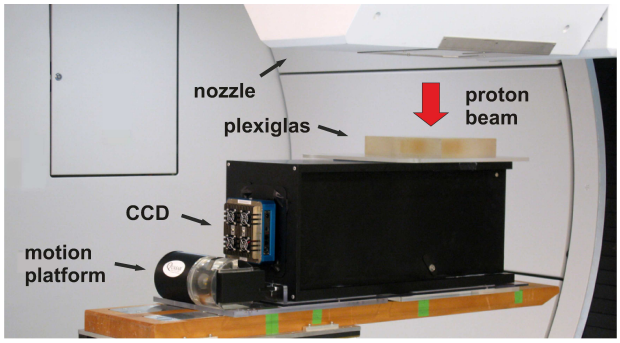

(a) CCD box mounted on Gantry 2

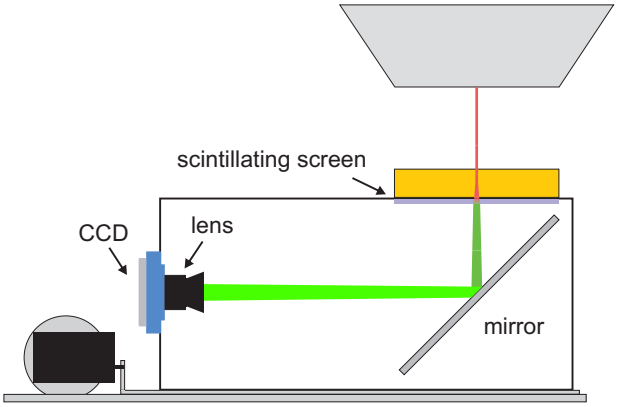

(b) internal view of the CCD box

Figure 4.8.: Measurement set-up for Gantry 2. Dose deposited by protons are converted to light by a scintillating screen. This light is deflected by a mirror to a camera, positioned at a distance from the beam.

4.3.1. Scintillating screen

To convert the energy loss of the protons to visible light, we chose a scintillating screen made of Gd_2O_2S:Tb powder. The thickness of the screen is about 400 μm, of which 65 μm consists of the scintillating material. The thickness of the scintillating layer is proportional to the light output and inversely proportional to the resolution. In our case, 1 Gy in the SOBP of a cubic target volume is equivalent to about one third of the dynamic range of the CCD camera. The wavelength of the light emitted by the screen is 545 mm. This matches the wavelength of peak quantum efficiency[6] (QE) of the CCD sensor to a good approximation at 560 mm.

According to the manufacturer, the modulation transfer function (MTF) of the scintillating screen, evaluated at the spatial frequency of the CCD camera defined by the pixel size and the distance to the screen, is about 60 %. This gives a contrast that results in the screen resolution not limiting the resolution of the whole imaging system.

After irradiation, there is still some light emitted. This afterglow decays rapidly. Various values have been proposed in the literature for the decay time of the afterglow, e.g., 100 ms [276] and 0.7 ms [277]. A reduction in intensity by a factor of 10^{-4} took 10 ms [277]. One study found that there are two decay times characterising the afterglow. The fast decay component had a decay time of 2.4 μs, while less than 1 s was measured for the slow decay component [274]. Similarly, yet another study determined the decay time from 90 % to 10 % as 1 ms and from 10 % to 1 % as 1.6 ms [278]. A second mechanism contributing to detectable signal at previously irradiated locations on the screen is activation of the PMMA slabs close to the screen. PMMA consists of carbon, oxygen and hydrogen. During proton irradiation, isotopes of oxygen and carbon are produced with decay times of several minutes. The decay products in turn excite the scintillating screen.

4.3.2. Quenching

The signal of an ideal dosimeter is linear in the linear energy transfer (LET) of the particle to the medium. The LET is defined only for charged particles and expresses the part of the stopping power lost by ionisation. Ionisation chambers fulfil this requirement down to very low particle energies, where the LET is highest [279]. The light output of many scintillating materials is reduced at high LET. This effect is called quenching. It is not fully understood why this happens. A popular theory is that for high LET, the material runs out of molecules that the traversing charged particles can excite [280]. A simple model of the light output per unit path length is the following [280]:

$$\frac{dL}{dx} = \left(\eta \frac{dE}{dx}\right) / \left(1 + kB\frac{dE}{dx}\right)$$

where η is the fraction of the energy released by the incident particles in the scintillator that is emitted as light by the scintillator, k is the fraction of the molecules excited by

[6] Quantum efficiency is the percentage of incident photons that create charge carriers in the CCD sensor. This depends on the energy and thus on the wavelength of the photon.

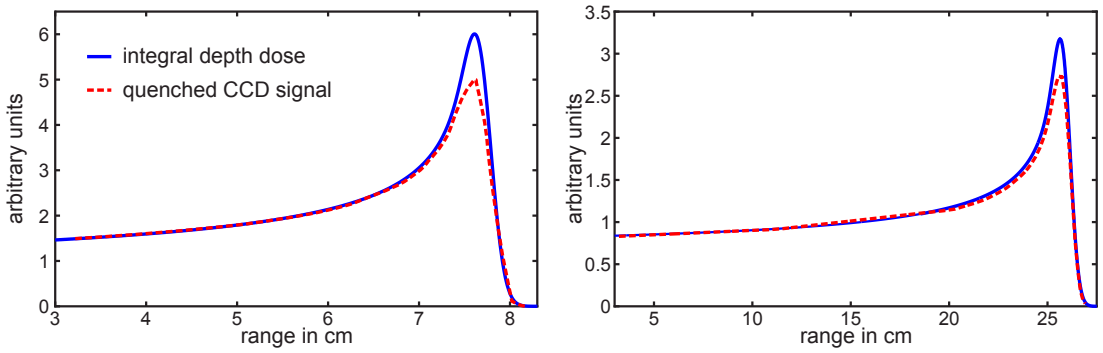

(a) (b)

Figure 4.9.: Calculated integral depth-dose curve and light output of the scintillating screen for a proton beam of (a) 100 MeV and (b) 200 MeV.

the secondary electrons that dissipate their energy non-radiatively, B is a proportionality constant relating the number of excited molecules to the energy loss and $\frac{dE}{dx}$ is the LET. Since k and B cannot be determined separately, they are combined to a single parameter. We are left with η and kB.

These three parameters were determined for three initial beam energies: 70 MeV, 100 MeV and 200 MeV. The measured light output was compared with the calculated integral depth dose. The energy in the plateau of the depth dose curve is so high that no quenching occurs. The light output curve was shifted so that it overlapped with the calculated curve in the plateau. kB turned out to be constant but η showed a dependency on the energy. Here are the results of the fit to the model:

$$kB = 0.0035 \pm 0.0001$$

$$\eta(E) = 1.593E^{-0.7571} + 0.9862$$

where the energy is given in MeV. Figure 4.9 shows the calculated integral depth dose and the measured light output for the initial energies 100 MeV and 200 MeV.

4.3.3. CCD camera

An Apogee Alta U6 CCD camera was chosen (Apogee Imaging Systems, Roseville CA, USA). Some of its properties are given in table 4.2.

Important for our purposes were the large pixel size and the low noise to allow exposure times of several minutes without image degradation. Especially the possibility to cool the camera to reduce dark current was required. While system noise affects the signal only during read-out, irrespective of the exposure time, dark current is proportional to the exposure time and doubles for every temperature increase of 6 °C. It arises due to spontaneous generation of electron hole pairs in the depletion zone of the pixels. Another reason for this choice of camera was the wavelength at which peak quantum efficiency is

Array size	1024 x 1024
Pixel size	$24\,\mu\text{m} \times 24\,\mu\text{m}$
Pixel size at iso-centre	$0.32\,\text{mm} \times 0.32\,\text{mm}$
Peak QE at 560 nm	$> 72\,\%$
Digital resolution	16 bit (0–65534) at 1 MHz digitisation rate
Cooling	50 °C below ambient temperature
System noise	$8\,e^-$ RMS
Dark current	$0.5\,e^-/s$ at 25 °C

Table 4.2.: Data sheet of the Apogee Alta U6 CCD camera. QE: quantum efficiency. RMS: root mean square.

achieved. This wavelength is very close to the light output wavelength of the scintillating screen.

The camera was connected to a Nikon AF Nikkor 50 mm F/1.8 D lens (Nikon Imaging Japan Inc., Tokyo, Japan) to image the whole scintillating screen in focus. A lens hood was attached to the lens to limit stray light. The aperture was set to $f/8$, where the resolution of the lens is diffraction limited. The size of the Airy disk at this setting is about 11 μm, which is smaller than the pixel size. Since this lens has negligible distortion, no geometrical corrections had to be applied. What the lens did introduce, however, was a radiometric distortion, namely a light intensity drop off the centre, also known as the $\cos^4$ law [281]. This distortion was unavoidable. A flat field correction was derived from measurements with the proton beam. Because the beam is most homogeneous in the central part, the measurement of the flat field was split into nine homogeneous, rectangular fields, covering an area of 24 x 30 cm^2 in T and U, see figure 4.10a. The overlap was 3 cm. The individual fields were cuboibds with an SOBP width of 4 cm. The central plane of these fields was imaged. This prevented inhomogeneity due to slight variations in range of the PMMA slabs.

Mono-energetic fields could also have been used and imaged in the plateau but a narrow spot spacing would have been necessary to achieve a homogeneous dose distribution. The passage through the PMMA slabs served the same purpose at the default spot spacing. After background subtraction, the images were stitched together and fitted with a two-dimensional function. In T, a quadratic polynomial was chosen, while in U, the sum of a quadratic polynomial and a Gaussian was fitted. The polynomials model the $\cos^4$ law. The additional Gaussian models the effect of what appears to be multiple reflections between the mirror and the scintillating screen [282]). This could be due to reflections either off the walls of the CCD box or off the light violet scintillating screen. Profiles of the fitted flat field are shown in figure 4.10b.

The problem of the radiometric distortion could be mitigated by placing the camera further away from the mirror. This would lead to a heavier box, which in turn would have to be supported by a more powerful (and more expensive) respiratory platform.

A CCD temperature of -20 °C proved to be a good compromise between temperature

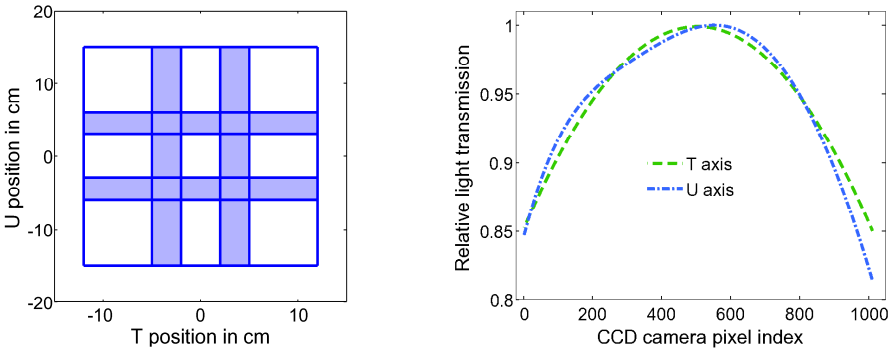

(a) (b)

Figure 4.10.: Measurement of the flat field: (a) layout of the individual fields used for covering the whole scintillating screen with the overlapping parts coloured, (b) central profiles along T and U of the fit to the flat field measurement.

stability and dark current. At -25 °C, the temperature regulation sometimes failed, especially when the air temperature in the treatment room was higher than usual.

Ambient light was suppressed by sealing the CCD box and switching off as many lights as possible in the treatment room. Any remaining ambient light was removed from the data by subtracting the background image.

4.3.4. Respiratory motion platform

In order to provide motion for the CCD camera system, a customised version of the Quasar respiratory motion platform (Modus Medical Devices, London, Ontario, Canada) was selected. The platform was enlarged so that the CCD box could be fastened onto it. Some specifications of Quasar are listed in table 4.3. The data of the accuracy and precision of the amplitude and the period are maximum values for sin and $\cos^4$ trajectories for both 4 s and 6 s motion period. In these tests, the CCD box was mounted on Quasar, including a representative amount of plexiglas slabs.

It is possible to load arbitrary motion trajectories and edit them directly in the control software. The signal obtained from the motor encoder is displayed to the user along with the planned trajectory. However, it turned out that this encoder signal was not a reliable surrogate of the actual motion.

Motion reproducibility was tested with an optical distance sensor. The standard deviation of the period was not more than 3 %. For the amplitude, the standard deviation was well below 1 %. The maximum absolute errors are given in table 4.3.

Sometimes, sudden shifts in amplitude occurred if the CCD box was put on the platform. If such a shift was observed during measurements, and it exceeded a millimetre, the current measurement was stopped and repeated.

Sampling frequency	100 Hz
Maximum peak-to-peak amplitude	PM: 30 mm
	RM: 40 mm
Amplitude accuracy	0.25 mm
	3 %
Amplitude precision	0.05 mm
	0.5 %
Period range	RM: 1–15 s
Period accuracy	65 ms
	1.1 %
Period precision	533 ms
	9 %
Maximum load	20 kg

Table 4.3.: Data sheet of the Quasar respiratory motion platform. The accuracy and precision data are the maximum values encountered during tests of different regular motion scenarios (see text for details). In rotation mode (RM), the trajectory is sinusoidal. In programmable mode (PM), the trajectory is arbitrary.

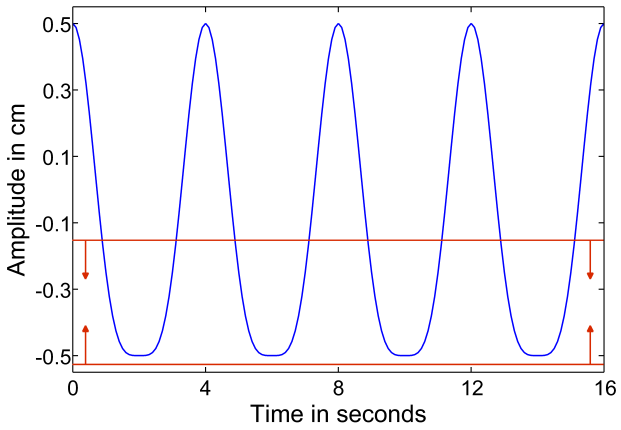

Figure 4.11.: Gating window for a regular trajectory. Irradiation resumes as soon as the motion surrogate enters the gating window.

4.3.5. Gating

As we have seen in section 3.3, the main idea of gating is to limit breathing motion effects by interrupting the treatment when the motion surrogate is outside the gating window. This is shown in figure 4.11.

To measure the amplitude of the respiratory platform, we acquired and calibrated an optical distance sensor. The gating window was then defined as an upper limit on the amplitude. If the signal was larger than this limit, the control system stopped the

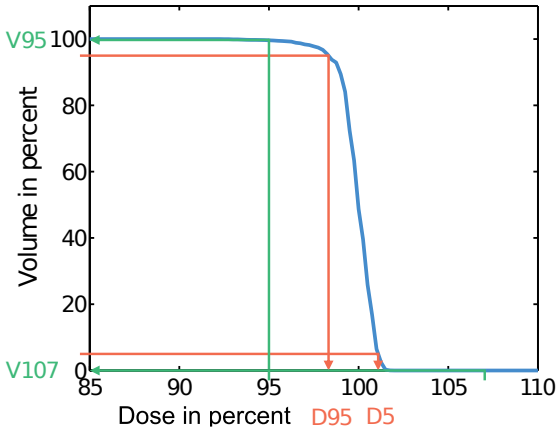

Figure 4.12.: Calculation of D_5, D_{95}, V_{95} and V_{107} from a DVH.

irradiation after the application of the current spot or path. This can be justified by the fact that during the short time it takes to apply a spot, the breathing motion is negligible, especially for re-scanning.

This approach is slightly problematic for paths because their application time is much longer than for a single spot. Splitting paths into straight pieces would be a solution. The additional dead time for loading these short paths into the control system is only an issue for a high number of re-scans.

4.4. Data analysis

Data analysis was performed using MATLAB (2010a, The MathWorks, Natick, MA, USA). Statistical values of the analysis region of interest (ROI) were extracted from the cumulative dose volume histograms (DVH) and dose area histograms (DAH). The ROI was defined as the CTV minus a margin of 5 mm. The reason why the ROI was smaller than the CTV was to avoid the dose gradient at the edge of the target volume and dose blurring effects [130, 110]. For the experimental results, only DAHs could be obtained because the data was available in the form of two-dimensional measured dose distributions, see section 4.3.

The minimum dose that a certain fraction v of the target volume receives is denoted by D_v. Similarly, the volume fraction that receives at least the dose d is symbolised by V_d, see also figure 4.12. In radiotherapy, D_5 - D_{95} is a common measure of the dose homogeneity, while 100 % - V_{95} and V_{107} indicate the percentage of the target volume receiving dose below or above the clinically acceptable values [122]. These values were added to form a statistic, 100 % - V_{95} + V_{107}, which measures the percentage of cold and hot spots in the target volume.

Since the measurement data is two-dimensional and not indicating dose but rather light output of the scintillating screen, the values predicted by the simulations were

extracted in the two-dimensional ROI corresponding to the WER of the measurement and corrected for the quenching effect, see section 4.3.2.

In the following, D_5 - D_{95} and 100 % - V_{95} + V_{107} are termed $D_{5\text{-}95}$ and $V_{\text{hot+cold}}$, respectively. Low values of these quantities indicate homogeneous dose distributions and little interplay effect.

$D_{5\text{-}95}$ and $V_{\text{hot+cold}}$, although inspired by the definition of DVH values, are not meant to be equivalent to the DVH values physicians refer to. They are merely a convenient measure of the interplay effect and the deterioration of dose distributions. Plans were judged clinically acceptable if $V_{\text{hot+cold}}$ was zero for all motion phases.

Since the statistical values calculated from the light output distributions are not normally distributed for different starting phases of the motion, the minimum and the maximum have been plotted for the simulation data. For the measurements, the data points were plotted individually due to the small sample size.

Hypotheses were tested by a two-sided Wilcoxon rank sum test. This test is a non-parametric test, not relying on normality of the underlying probability distribution. The null hypothesis is that both samples are drawn from the same probability distribution. Actually, samples from two distributions with equal median but different variance pass the null hypothesis.

The significance level α was set to 5 % for all statistical tests. In the tables reporting the results of the statistical tests, the symbol = indicates that the null hypothesis was not rejected. If it was rejected, the symbols + and - show if the values in the first sample were larger or smaller than the values in the second sample.

5. Experimental verification of motion mitigation of discrete proton spot scanning by re-scanning

As discussed in section 3.2, many studies have investigated *in silico* the possible advantages of re-scanning for alleviating the interplay effect. In addition, experimental verification of re-scanning has been carried out for raster scanning of carbon ions at NIRS [188]. However, the motion trajectory was a simple sinusoidal curve, re-scanning was combined with gating and the dose was recorded with an array of ionisation chambers, resulting in only a few point measurements of the dose. On the other hand, data at different depths could be acquired in a single measurement. However, no work has been done experimentally investigating the effects of different re-scanning approaches for scanned proton therapy, or by using a high resolution detector such as the CCD system described in section 4.3. In addition, in this work, we wished to systematically separate out the effects of re-scanning alone and re-scanning combined with gating. The latter approach is discussed in chapter 6.

In this chapter[1], we report on the detailed experimental investigations of the interplay effect and the effectiveness of different re-scanning strategies under varying motion conditions and address the following questions:

- What is the relationship between the motion parameters and the interplay effect?
- Which re-scanning strategy best mitigates the interplay effect?
- Do the experimental results agree with simulations?

5.1. Outline of performed measurements

The interplay effect was studied as a function of amplitude for motions perpendicular and parallel to the faster of the two beam scanning directions and for several motion periods. Furthermore, dose distributions at different water-equivalent depths in the phantom were taken for one combination of motion parameters. The results from these measurements allowed for the selection of motion parameters for the subsequent measurements of re-scanning, i.e., those for which the interplay effect was most pronounced. All possible combinations of scaled and iso-layered re-scanning, layered and volumetric re-scanning were investigated. The definition of the target volume is discussed in section 5.1.1.

[1]This chapter has been submitted for publication [283].

Energy re-scanning	Weight re-scanning	Parameter	Abbreviation
layered	iso-layered	dwell time	LI
volumetric			VI
layered	scaled	# re-scans	LS
volumetric			VS

Table 5.1.: Abbreviations of re-scanning techniques as used in the text.

For the measurements without motion, i.e., the reference data, 3 images were taken. To assess the impact of motion without re-scanning, the motion amplitude was increased from 1 mm to 5 mm in steps of 1 mm and, as an extreme case, up to 10 mm. Three motion periods of 4, 6 and 8 s have been used, and the lateral beam scanning axes were parallel as well as perpendicular to the motion direction. For re-scanning, the motion amplitude was limited to 5 mm and 10 mm, while the motion period was fixed at 6 s. The dependence on the water-equivalent depth of the ROI was checked for 10 mm amplitude and a 6 s period. For all measurements other than the static reference measurements, either 5 or 6 images per parameter set were taken to randomly sample the starting phase of the motion. The prescribed dose was always set to 1 Gy.

Statistical tests could not be applied to the comparison between scaled and iso-layered re-scanning as it is not clear which amount of scaled re-scanning corresponds to which amount of iso-layered re-scanning. Therefore, conclusions were drawn based solely on visual inspection of the data.

The abbreviations for the different re-scanning techniques are listed in table 5.1.

5.1.1. Target volume

A spherical CTV with radius 3.5 cm was taken and expanded with a margin of 0.5 mm in the direction of motion. This resulted in an ITV with a volume of 199 ccm. The target was centred at a depth in water of 10 cm. The choice of target size was motivated by the fact that its volume was close to the volume of the largest liver target studied by Bernatowicz et al [284] and similar to the smallest spherical target investigated by Zenklusen et al [110]. Liver tumours are likely candidates for the application of motion mitigation techniques with spot scanning.

A two-dimensional ROI was defined as the intersection of CTV − 5 mm with the measurement plane. The reason for the negative margin of 5 mm is that the CTV edge lies roughly on the 90 % iso-dose, adding inhomogeneity to the dose distribution which is not caused by the interplay effect. This approach is in line with other studies of the interplay effect [130, 110]. The data analysis is described in section 4.4.

Adding an ITV increases dose to normal tissue. Therefore, we limited our study to tumour motion of up to 1 cm. Larger motion should be addressed by other motion mitigation techniques, for example gating or breath-hold. No PTV was defined because the set-up errors for the experiments were considered negligible.

5.2. Results

5.2.1. Interplay effects without motion mitigation

The motion direction with respect to the primary (faster) beam scanning direction had only a small influence on $D_{5\text{-}95}$ (dose inhomogeneity) for both measurements and simulations [110] as presented in figure 5.1a for a motion period of 6 s. $V_{\text{hot+cold}}$ was measured to be worse for motions perpendicular to fast scanning, as shown in figure 5.1b. This was also predicted by the simulations.

Measurements showed that $D_{5\text{-}95}$ scaled approximately linearly with motion amplitude in the range from 1 mm to 10 mm (squared correlation coefficient: parallel: $R^2 = 0.92$, perpendicular: $R^2 = 0.95$). Higher-order polynomials do not improve the quality of the fits due to the spread in the data for a fixed amplitude. $D_{5\text{-}95}$ varied linearly for small amplitudes and was somewhat larger for the static case than expected. This hints at the fact that a little motion can wash out dose inhomogeneities in the static dose distribution. The simulations suggested that the amplitude range where $D_{5\text{-}95}$ was increasing linearly was roughly from 1 mm to 15 mm, but this depended on the period, the direction of motion and the scanning and analysis region. The slope of $D_{5\text{-}95}$ was smaller outside of the linear part.

Interestingly, the spread in the median light output in the measurements was heavily dependent on the motion and scanning directions. This is displayed in figure 5.1c. Motion perpendicular to fast scanning introduced large deviations from the reference light output. This also resulted in a larger spread of $V_{\text{hot+cold}}$ (under- and over-dosage), as this value is sensitive to the median light output.

Varying the motion period between 4 s and 8 s did not statistically significantly alter the interplay effect (as quantified by $D_{5\text{-}95}$) for either simulations or measurements, as displayed in figure 5.2a for motion perpendicular to the primary scanning direction. Interestingly, the experiments revealed a systematic drop in median light output, but only for the 4 s period, as visible in figure 5.2c. For motion perpendicular to primary scanning, this offset was accompanied by a large spread in median light output, again also connected with an enlarged spread in conformity. Although in the simulation data the offset was not visible, the spread was predicted but overestimated.

In general, the $D_{5\text{-}95}$ and $V_{\text{hot+cold}}$ values were overestimated by the simulations. Additional simulations indicated that the interplay effect was even more pronounced for periods below 3 s. Taking into account that not many patients breathe with such a small period [51] and that the motion platform had increasing difficulty to follow the trajectory accurately, we decided not to further investigate this effect.

5.2.2. Comparison of different re-scanning techniques

Comparison of layered scaled (LS) and volumetric scaled (VS) re-scanning

Table 5.2 confirms that for the measurements, VS yielded statistically significantly lower $D_{5\text{-}95}$ values starting from 8 re-scans for 5 mm and 10 re-scans for 10 mm motion amplitude. However, $V_{\text{hot+cold}}$ was not statistically significantly different for 5 mm amplitude,

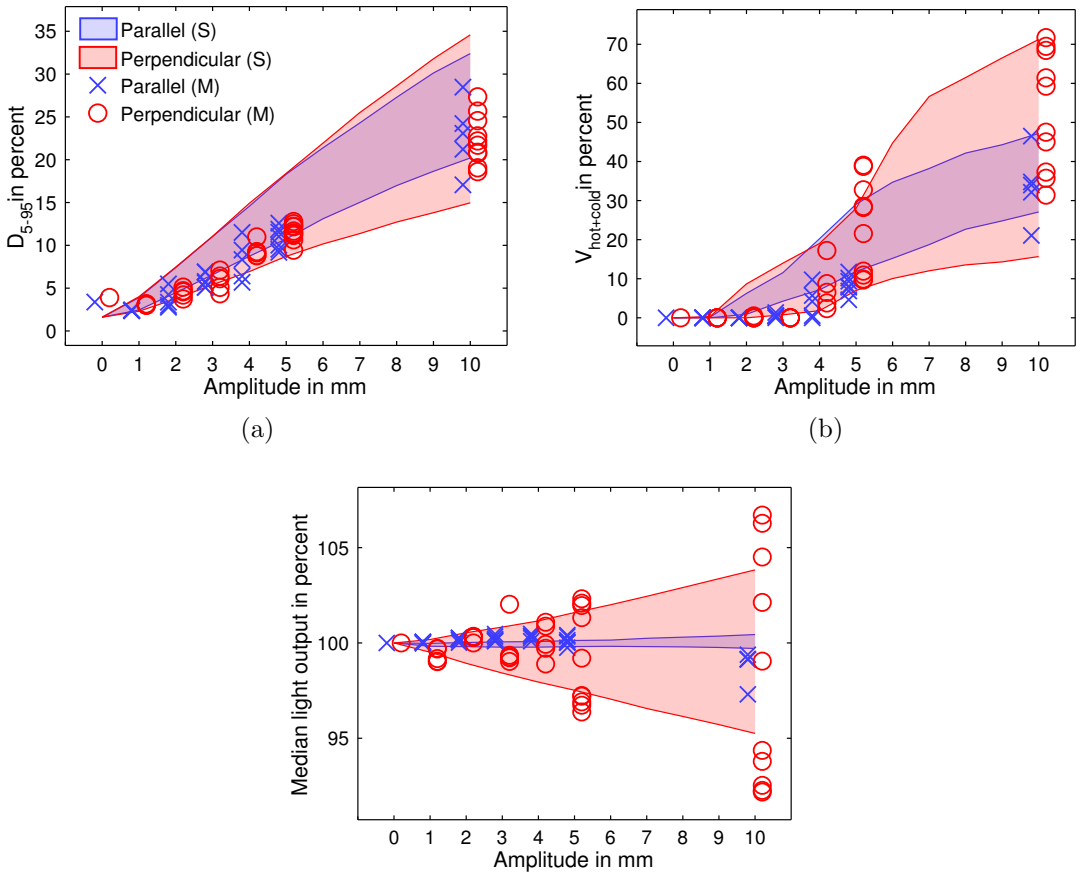

Figure 5.1.: Interplay effect as a function of motion amplitude in terms of (a) $D_{5\text{-}95}$, (b) $V_{hot+cold}$ and (c) median light output relative to prescribed dose for simulations (S) and measurements (M). The motion period was 6 s. For the simulations, the area between the minimum and maximum values out of 36 different starting phases was shaded, restricted to the two-dimensional region of interest of the measurement. Each marker represents a single measurement.

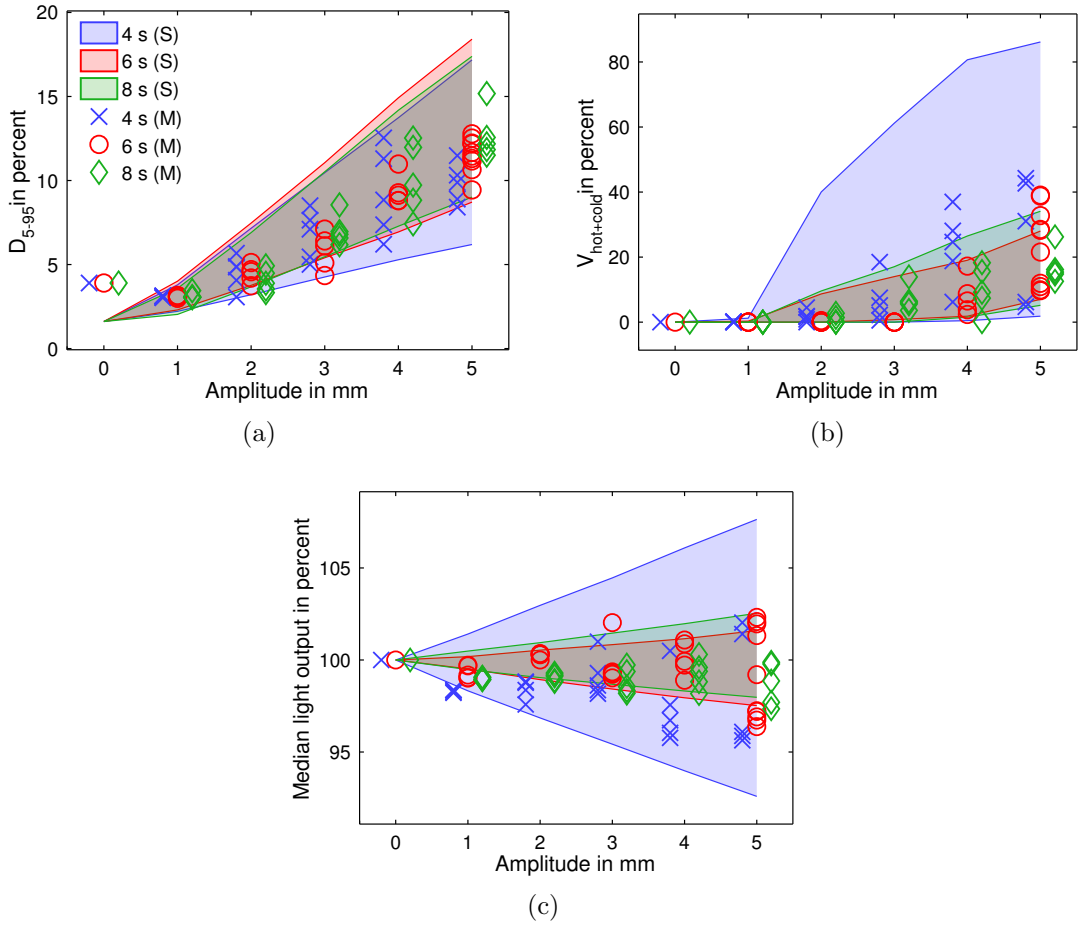

Figure 5.2.: Dependence of the interplay effect on the motion period for different motion amplitudes in terms of (a) $D_{5\text{-}95}$, (b) $V_{\text{hot+cold}}$ and (c) median light output relative to prescribed dose. Data from simulations (S) and measurements (M) are plotted. For the simulations, the area between the minimum and maximum values out of 36 different starting phases was shaded, restricted to the two-dimensional region of interest of the measurement. Each marker represents a single measurement.

A [mm]	N	$D_{5\text{-}95}$		$V_{hot+cold}$		median	
		p_{exp}	p_{sim}	p_{exp}	p_{sim}	p_{exp}	p_{sim}
5	6	=	+	=	+	=	-
	8	+	=	=	=	+	-
	10	+	+	=	+	=	-
	12	..	+	..	+	..	-
10	6	=	+	=	+	=	-
	8	=	=	+	-	=	-
	10	+	+	=	+	-	-
	12	+	+	+	+	-	-

Table 5.2.: Wilcoxon rank sum test for the null hypothesis that the statistical values $D_{5\text{-}95}$, $V_{hot+cold}$ and median light output were equal for LS and VS. P-values for both simulated (p_{sim}) and experimentally measured (p_{exp}) results are given. The significance level was 5 %. The statistical values for LS were (+) significantly larger, (-) significantly smaller or (=) compatible with the values for VS. For median light output, = is best, while for the other two statistics, lower is better. Some data (..) was not available. A is the motion amplitude and N is the number of re-scans.

which is somewhat contradictory to the results shown in figure 5.3. For VS, hot and cold spots were washed out for at least 4 and 8 re-scans for the smaller and larger amplitude, respectively. On the other hand, with LS, hot and cold spots remained even for up to 12 re-scans. The simulations predicted that the dose distributions should get temporarily worse at about 7 to 8 re-scans for VS. This could not be confirmed by measurements. When random fluctuations of ±5 % were introduced to the motion period or the proton flux in the simulations, these bumps disappeared, indicating that in reality these interference effects are negligible.

Comparison of layered iso-layered (LI) and volumetric iso-layered (VI) re-scanning

In the case of iso-layered re-scanning, the measurements revealed smaller differences between the two techniques than for scaled re-scanning, as visible in figure 5.4 and confirmed statistically in table 5.3. This was expected from the simulations, which indicated that LI should yield statistically significantly higher $D_{5\text{-}95}$ and $V_{hot+cold}$ values than VI in about half of the cases for both motion amplitudes. As explained in section 3.2, for iso-layered re-scanning, the re-scan factor is determined by the maximum dwell time allowed for each spot, with shorter dwell times resulting in a higher order of re-scanning. In the experiments, a dwell time of 1 ms was sufficient to suppress any hot or cold spots and 2 ms was enough to reduce $D_{5\text{-}95}$ to below 10 % for 5 mm motion amplitude for both LI and VI. In the case of 10 mm motion amplitude, VI for 0.75 ms or less yielded distributions with less than 10 % $D_{5\text{-}95}$, while for LI, 0.5 ms was necessary to achieve this. Both techniques were generally able to wash out over- and under-dosage for 0.75 ms or

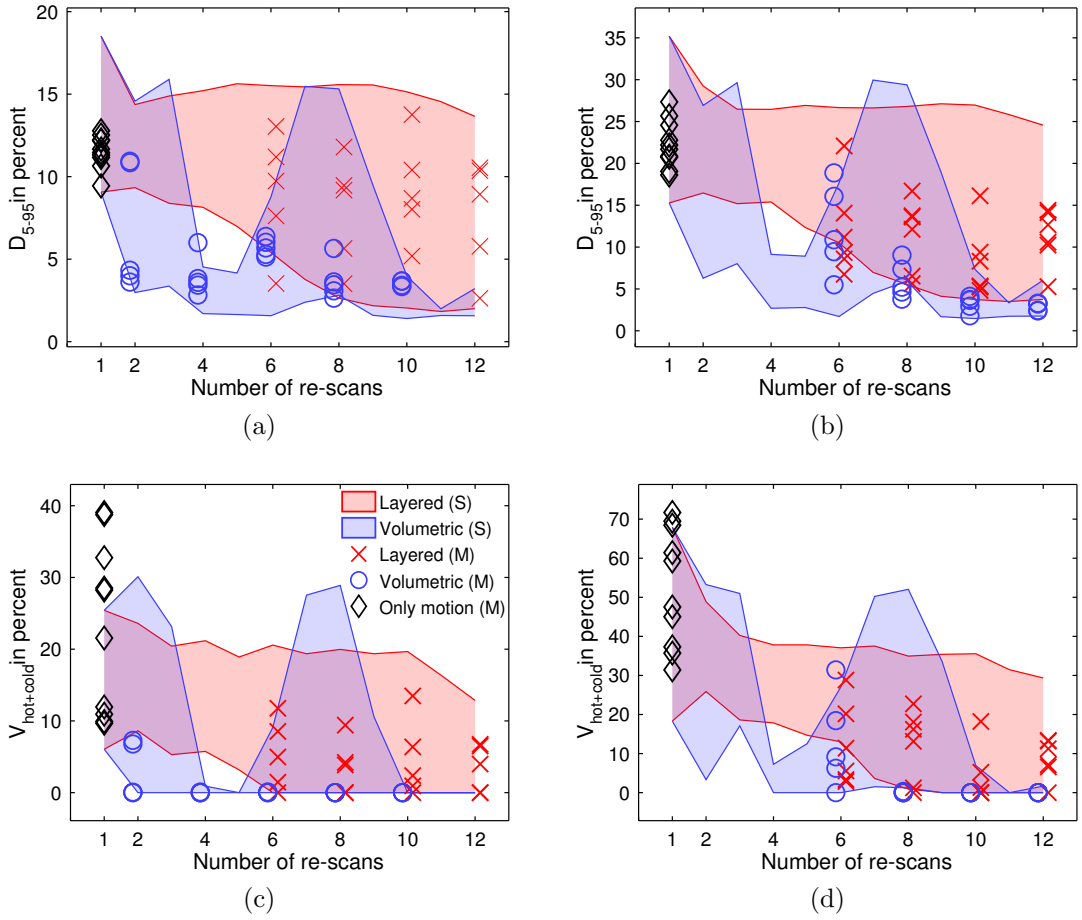

Figure 5.3.: Comparison of LS and VS. $D_{5\text{-}95}$ for (a) 5 mm and (b) 10 mm motion amplitude, $V_{hot+cold}$ for (c) 5 mm and (d) 10 mm motion amplitude. Data from simulations (S) and measurements (M) are plotted. For the simulations, the area between the minimum and maximum values out of 36 different starting phases was shaded, restricted to the two-dimensional region of interest of the measurement. Each marker represents a single measurement.

		$D_{5\text{-}95}$		$V_{hot+cold}$		median	
A [mm]	T [ms]	p_{exp}	p_{sim}	p_{exp}	p_{sim}	p_{exp}	p_{sim}
5	2	=	+	=	+	=	=
	1	=	=	=	=	+	=
	0.75	=	+	=	+	+	-
	0.5	-	+	=	=	+	=
10	2	+	+	+	+	=	=
	1	=	=	=	=	=	=
	0.75	+	=	=	=	-	-
	0.5	-	+	=	+	=	=

Table 5.3.: Wilcoxon rank sum test for the null hypothesis that the statistical values $D_{5\text{-}95}$, $V_{hot+cold}$ and median light output were equal for LI and VI. P-values for both simulated (p_{sim}) and experimentally measured (p_{exp}) results are given. The significance level was 5 %. The statistical values for LI were (+) significantly larger, (-) significantly smaller or (=) compatible with the values for VI. For median light output, = is best, while for the other two statistics, lower is better. A is the motion amplitude and T is the dwell time per re-scan.

less, although there were a few measurements showing dose outside the ICRU limits. The simulations actually predicted LI would perform worse. For example, $V_{hot+cold}$ was predicted to reach zero for LI for both amplitudes only for a dwell time of 0.5 ms. The simulated results for VI were comparable to the measurements.

Comparison of scaled and iso-layered re-scanning

For layered re-scanning, $D_{5\text{-}95}$ is shown in 5.5. LI performed better and with shorter treatment times than LS for 5 mm motion amplitude in both $D_{5\text{-}95}$ as well as $V_{hot+cold}$. For 10 mm motion, the differences were smaller, but LS could still not compete with LI. These results could be seen in both simulations and measurements. As predicted by the simulations, the spread in the statistical values was much larger for LS. Clinically acceptable plans without any dose outside the ICRU specifications could only be achieved by LI. The only apparent drawback of LI is that the median light output is deviating much more from 100 % than LS. The very long treatment time of LI for 0.5 ms was only reflected in better motion mitigation for the larger motion amplitude. In figure 5.6, the results for volumetric re-scanning are given. Experimentally, VS leads to lower $D_{5\text{-}95}$ and was less affected by different motion starting phases than VI for both amplitudes. In addition, generally less treatment time was necessary for VS to achieve an improved effect, although this was not the case when the interplay effect increased again at 6 re-scans for 5 mm amplitude. In other words, to wash out all hot and cold spots, a shorter treatment could be used for VS than for VI re-scanning. As observed above, the spread of the median values was again much larger for VI, with a systematic shift away from

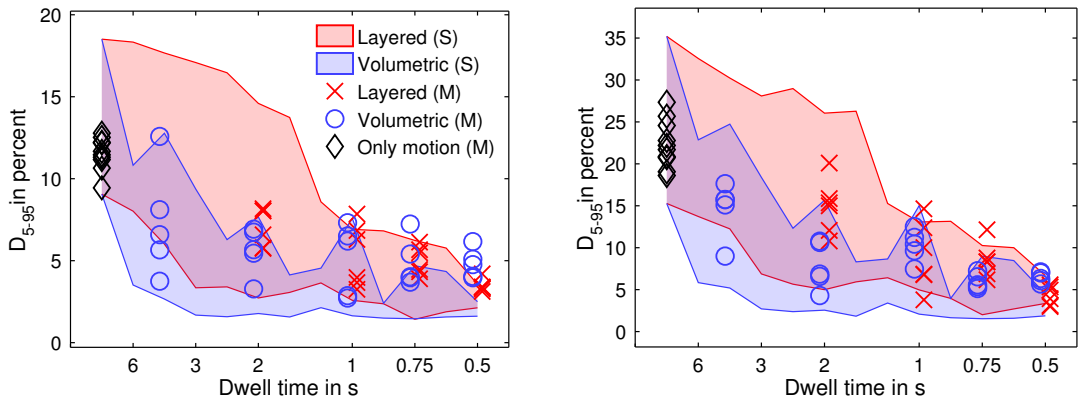

Figure 5.4.: Comparison of LI and VI. $D_{5\text{-}95}$ for (a) 5 mm and (b) 10 mm motion amplitude. Data from simulations (S) and measurements (M) are plotted. For the simulations, the area between the minimum and maximum values out of 36 different starting phases was shaded, restricted to the two-dimensional region of interest of the measurement. Each marker represents a single measurement.

the 100 % value for most of the cases, especially for the smaller motion amplitude.

For the results of the simulations on volumetric re-scanning, see the two preceding paragraphs in this section.

5.2.3. Influence of the WER of the analysis region

Because it is time-consuming to acquire all dose distributions at different WER with the CCD system, the influence of the WER on the interplay effect was studied only for the case of no motion mitigation. Generally, the interplay effect in the measurements increased for larger WER, see figure 5.7. Its influence was rather small when looking at $D_{5\text{-}95}$, but led to a doubling in $V_{\text{hot+cold}}$ between 8 cm and 11 cm WER and also affected the spread of the median dose. The reason for this trend is that, for smaller WER, each point in the dose distribution receives dose from several Bragg peaks, whereas for larger WER, only a few Bragg peaks contribute to the total dose. The simulations predicted the same pattern, but the dependence of the spread of the statistical values on the WER was not replicated well.

5.3. Discussion

The impact of tumour motion on the dose distributions of a spherical target for different motion parameters such as period, amplitude and direction with respect to the primary scanning direction has been studied experimentally and the ability of different re-scanning schemes to mitigate these effects quantified. In particular, we have studied

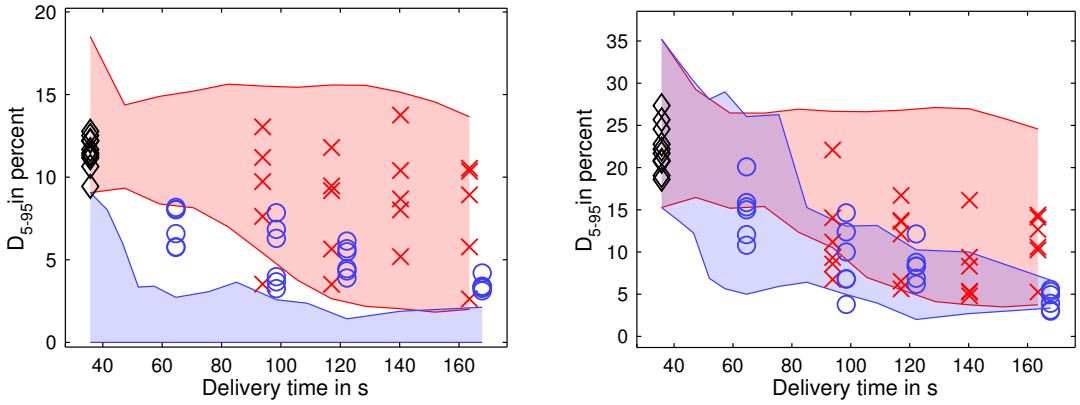

Figure 5.5.: Comparison of LI and LS. $D_{5\text{-}95}$ for (a) 5 mm and (b) 10 mm motion amplitude. See figure 5.6b for the legend. For the simulations, the area between the minimum and maximum values out of 36 different starting phases was shaded, restricted to the two-dimensional region of interest of the measurement. Each marker represents a single measurement.

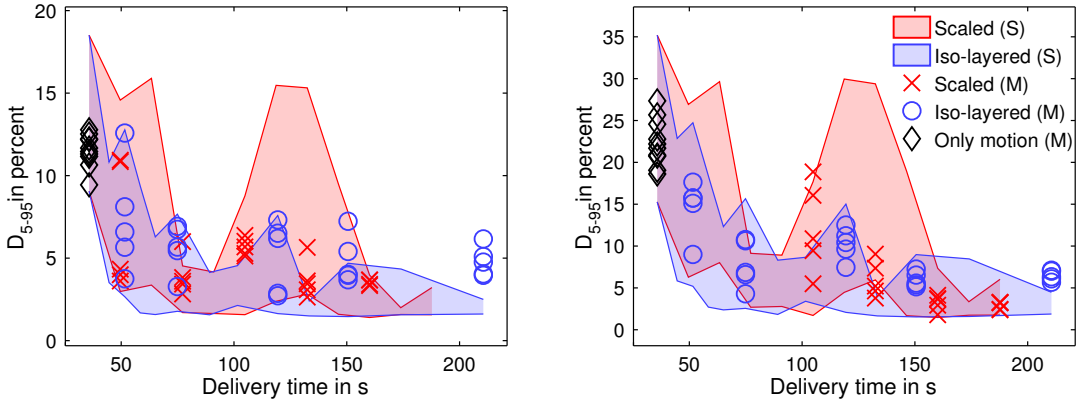

Figure 5.6.: Comparison of VI and VS. $D_{5\text{-}95}$ for (a) 5 mm and (b) 10 mm motion amplitude. Data from simulations (S) and measurements (M) are plotted. For the simulations, the area between the minimum and maximum values out of 36 different starting phases was shaded, restricted to the two-dimensional region of interest of the measurement. Each marker represents a single measurement.

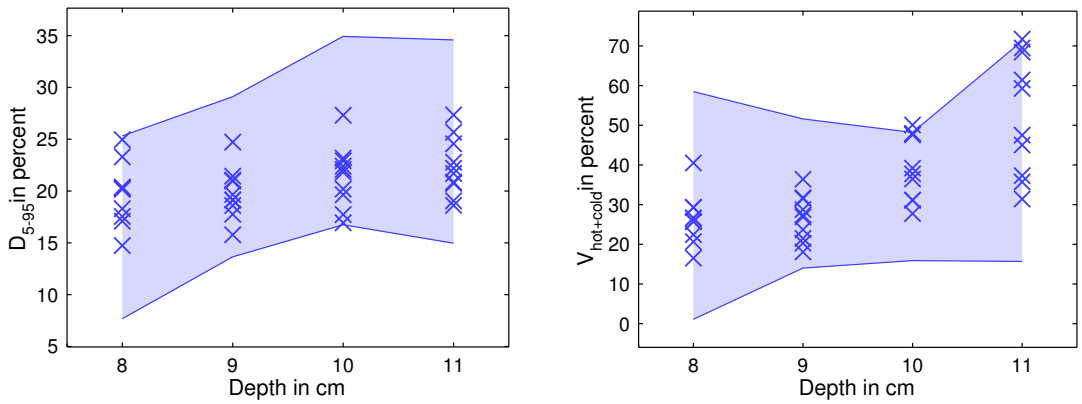

(a) (b)

Figure 5.7.: Interplay effect for different water-equivalent ranges of the analysis region in terms of (a) $D_{5\text{-}95}$ and (b) $V_{hot+cold}$ for 1 cm motion amplitude and 6 s motion period. For the simulations, the area between the minimum and maximum values out of 36 different starting phases was shaded. Each marker represents a single measurement.

the relative effectiveness of scaled or iso-layered, layered or volumetric re-scanning for reducing $D_{5\text{-}95}$ resulting from motion.

The interplay effect has been found to scale approximately linearly with motion amplitude in the case of a spherical target. $D_{5\text{-}95}$ was not affected by the motion period or motion direction relative to the primary scanning direction. Conversely, motion perpendicular to scanning led to a larger spread in the median light output values. A large motion period showed the opposite effect. Motion mitigation is necessary for amplitudes above 2 mm in order to apply clinically acceptable treatment plans, but this had been found to depend on the motion period.

VS mitigated the interplay effect more effectively than LS, reducing $D_{5\text{-}95}$ to less than 5 % for both 5 and 10 mm motion amplitudes. LI performed worse for few re-scans and better for more re-scans than VI, but this was statistically significant only for 10 mm amplitude. For the motion parameters studied, VS seems to be the best choice for treating moderately moving tumours with motion amplitudes of up to 10 mm. The measurements also confirmed that there is a trend for larger motion effects in the distal regions of the target, justifying the choice of a distal analysis region, although this trend is only statistically significant for analysis of hot and cold spot volumes.

Generally, the simulations were well reproduced by the experimental results, with the exception of VS. Often the measured median light output relative to the static case was 1–2 % higher than predicted by simulations for re-scanning, especially for iso-layered re-scanning. The p-values of the statistical tests, as listed in tables 5.2 and 5.3, calculated for the simulated data did not agree with the p-values obtained by testing experimental data. However, the following simplifications have been made in implementing the dose calculation: constant motion period, constant proton flux, perfect dose delivery, perfect

performance of the beam deflection magnets and a phantom made of water (as opposed to PMMA for the measurements), which can have an effect on the beam widths due to multiple scattering in the phantom in comparison to the simulations (measured beam widths will be somewhat smaller than those in the simulations). Since the interplay effect approximately scales linearly with the motion period for a spherical target, it is sufficient to measure it at two different amplitudes and deduce $D_{5\text{-}95}$ for other amplitudes by interpolation. Extrapolation seems also possible beyond 10 mm of motion amplitude. However, the simulations indicated that the interplay effect grows more slowly (sub-linearly) between 10 mm and at least 2 mm. This interpolation works in principle also for $V_{\text{hot+cold}}$, but here a quadratic or cubic function has to be fitted, so data at three or four different amplitudes is necessary, making this fit procedure less efficient. However, it should be stressed that these trends, although interesting, may only be valid for relatively regular targets such as the spheres studied here, and whether such trends are valid for real (and irregular) tumour volumes still needs to be validated.

The finding from our simulations that motion periods below 3 s are more susceptible to motion effects is a result of the dynamics of the delivery. If an iso-energy layer is delivered in, say, 1 s, then for a motion period of 2 s, the spots will be considerably shifted from their nominal positions, leading to an inhomogeneous contribution to the total dose, while for a period of 8 s, this offset is much smaller and the dose contribution will remain quite homogeneous. Of course, this picture is only valid for iso-energy layers where adjacent spots are weighted similarly. For realistic targets (where spot weight optimisation will tend to result in much more variation in spot weights within each energy level) this premise is not valid. In this case, only simulations and measurements can estimate the interplay effect, but this estimate is highly dependent on the target shape and its motion, not to mention range changes due to a potentially deforming anatomy. Because the light output distributions were affected by motion to about the same degree for motion periods above 3 s, the choice of 6 s for the measurements was somewhat arbitrary. On the other hand, a longer period put less stress on the motion platform and arguably increased the accuracy of its motion. Generally, spherical targets are less affected by the interplay effect than cubic targets because the spot weights are not uniform within an iso-energy layer. We expect that for realistic, less regular targets, motion effects should be even smaller than for spheres.

Although the measured distributions improved more for volumetric re-scanning, the improvement as a function of re-scanning magnitude was more predictable for layered re-scanning. This effect was predicted by the simulation and has also been observed by others [193, 113] and is a result of the interplay between the motion period and the timing of the treatment delivery [110]. Because the motion period and the proton flux are smeared out in a real treatment, we expect that this effect will not be of relevance in clinical applications. This view is supported by the fact that the pattern is less prominent in the experimental results than predicted. On the other hand, similar behaviour has recently been found from simulations of clinical cases by [284], and this needs to be investigated further experimentally through the use of clinically relevant target volumes, ideally in realistic patient geometries.

However, in order to interpret these results, one has to be aware of the limitations of the measurements presented here:

First of all, information about the dose distribution is only available in two dimensions and most of the dose is delivered by the most distal iso-energy layer, with more proximal spots receiving dose from these more distal spots. Therefore, we would expect the interplay effect to be less in the proximal part of the target. Because of this, we chose a plane for our measurements that lies distal to the centre of the target, but still in the region where the cross section of the target is large.

Second, the signal from the scintillating screen is quenched for large stopping powers [275] and thus the measured ratio of Bragg peak to plateau is smaller than that used for the simulations, which is based on ionization based depth-dose measurements of our clinical Bragg peaks. For the case of a target with a fixed rectangular cross section, it would be possible to calculate a correction factor to the iso-energy layer studied, based on the weights of the contributing Bragg peaks at this depth. Unfortunately, these contributions vary significantly across an iso-energy layer for all but the simplest targets. Taking a sphere as an example, the central spot will receive dose from all distal iso-energy layers, while for a spot at the edge there might be no distal iso-energy layer at all. In a static scenario, correction factors can be assigned separately to all spots in the target. In the presence of target motion however, there is no accurate solution to this problem. Simulations however showed that the statistical values affected by quenching always overestimated the true values. To circumvent the problem of quenching and two-dimensional data, three-dimensional dose distributions could be calculated based on the actual motion and spot application timing of the measurements [285]. On the other hand, unless it is thoroughly verified, this method cannot be considered an independent test of the results from simulations. Another approach, three-dimensional arrays of ionisation chambers, suffers from small spatial resolution. Polymer gels can be used only once and need considerable preparation. For these reasons, we think that our CCD system is well suited to the task of measuring the interplay effect.

Third, only 5 or 6 measurements have been taken per parameter combination. Naturally, the distribution of the statistical values with motion phase cannot be determined accurately by such a rather limited number of measurements. On the other hand, a comparison of the results from 5 and 10 measurements with re-scanning showed that the difference was not statistically significant. Moving on to practical issues, for both scaled and iso-layered re-scanning, there is a limit to the amount of re-scanning that can be applied. Scaled re-scanning is limited by low-weighted pencil beams because re-scanning these can introduce weights which are not deliverable. In addition, since the central and proximal parts of the target volume receive much dose from distally deposited pencil beams, the spot weights on the border of iso-energy layers are generally higher. For iso-layered re-scanning, decreasing the dose per spot per visit thus affects mainly the highly weighted spots. After a couple of re-scans, the low-weighted spots have been completely delivered, and will not be visited any more, whereas the time between visits to the higher weighted spots will be considerably reduced. Thus the full statistical effect of re-scanning cannot be exploited.

Another problem of re-scanning is the possibility that some spots are scanned with a similar frequency to the target motion so that interplay effects are only marginally affected [81, 110]. This is most likely the case for volumetric re-scanning, since one complete scan takes typically about 6 s, depending on the target volume, which is similar to the breathing frequency. Random pauses or varying the scanning path may solve this problem. For phase-controlled re-scanning (PCR), where the beam intensity is adjusted so that the re-scans of an energy slice just fit into one respiratory cycle (or gating window), the standard deviation of the dose decreases exponentially with a higher number of re-scans (not as the inverse square root as in conventional re-scanning) [37]. PCR is similar to the breath-sampling method [106], where the respiratory phase at the start of a re-scan is distributed over the whole respiratory cycle.

A potential disadvantage of re-scanning is the relatively large treatments time. For instance, short dwell times for iso-layered re-scanning can cause very long treatment times without substantially improving the homogeneity of the dose distributions. This might be improved by better distributing the re-scans of the highly weighted spots. Most of the increase in treatment time is due to the dead time in lateral scanning, i.e., the time it takes to reposition the beam. Therefore, continuous line scanning would be ideal for re-scanning, where the beam is not switched off between spots. The only dead time would arise from energy changes. However, the technical challenges to the implementation and verification of continuous line scanning are greater than for discrete spot scanning. The potential of continuous line scanning for motion mitigation is investigated in detail in chapter 7.

Although re-scanning can reduce interplay effects if the tumour motion is not too large, the planned target volume has to be large enough to cover all positions of the mobile tumour, leading to a potentially unnecessary irradiation of normal tissues. Hence, the combination of re-scanning with gating or breath hold to reduce this volume would be advantageous, even if such approaches would also lead to longer irradiation times [37, 188]. In addition, the ITV volume should also be designed to include the effects of range changes due to organ motion [189, 190, 191]. Although this may not be a big problem for liver cases, where most of the surrounding tissues and anatomy are quite homogeneous in density, the effectiveness of re-scanning for lung or oesophageal tumours can only be studied by realistically taking into account the effects of density changes due to motion, and in this case, the ITV volumes can become quite large [191].

Finally, in this work, the interplay effect, and the effectiveness of re-scanning, has been studied only assuming a single field and a single fraction. Typically however, proton plans consist of 2 to 4 fields and applying plans with multiple uniform fields can also be considered as a form of re-scanning [193]. In this case, the number of re-scans for each field of a multiple field plan could probably be reduced. In addition, 4D computed tomography (4D-CT) or 4D magnetic resonance imaging (4D-MRI) data may give insight into the main direction of motion for each treatment site and, for fields where the motion is mainly along the beam axis, the magnitude of re-scanning could perhaps be reduced. Fractionation is per se also a kind of re-scanning. Over the course of fractionated treatment, the interplay effects that show up in a single fraction are

expected to average out [81, 92] and variations in inter-fraction motion may provide an additional smearing effect.

5.4. Conclusion

The interplay effect between periodic tumour motion and discrete spot scanning has been investigated for a spherical mobile target in a homogeneous phantom for various motion parameters. Furthermore, the benefit of re-scanning has been experimentally assessed in terms of dose inhomogeneity through the analysis of dose distributions measured using a mobile CCD detector system. Dose inhomogeneity has been found to scale approximately linearly with the motion amplitude, with motion period only having a small influence on the resulting dose distributions. In addition, we have found that volumetric re-scanning of the iso-energy layers performed statistically significantly better than layered re-scanning for both studied techniques to distribute the spot weights among the re-scans, scaled and iso-layered re-scanning. Differences between layered and volumetric re-scanning were smaller for iso-layered re-scanning. Due to the higher number of energy changes in volumetric re-scanning, the treatment time for the same number of re-scans is up to 20 % larger for scaled re-scanning and up to 25 % larger for iso-layered re-scanning than for the layered re-scanning approach and thus, for systems with a slower energy change, layered, iso-layered re-scanning can still be recommended to mitigate the interplay effect for amplitudes up to 5 mm. However, our results suggest that even tumours moving up to 10 mm can still be treated with volumetric scaled re-scanning. Further studies are needed to corroborate these findings for different motion periods and target volumes and in an inhomogeneous phantom to include the effects of range changes. For larger motion, re-scanning should be combined with gating or breath-hold. This would also reduce the dose to normal tissue thanks to a reduction in the necessary ITV margins.

6. Experimental verification of gating for treating mobile targets with proton spot scanning

Gating in scanned charged particle therapy has been studied experimentally with radiochromic films in a single-energy layer at GSI [130] and with an array of pin-point ionisation chambers for a spherical target at NIRS [188], see also section 3.3. As discussed in section 3.2, phase-controlled re-scanning reduced residual motion effects in gated treatment [188].

In this chapter, we expand on this work by experimentally assessing the benefit of gating and re-scanning for proton spot scanning when applied not only to a mobile spherical target but also to a patient target and to realistic breathing patterns. While an array of ionisation chambers measures dose at a small set of single points, high resolution imaging detects even small hot and cold spots in dose distributions.

In the following, we want to answer these main questions:

- Can gating mitigate the interplay effect or is a combination with re-scanning necessary?
- How does gating perform on realistic, irregular target volumes and motion trajectories?
- What is the optimal combination of gating and re-scanning in terms of delivery time?

6.1. Outline of performed measurements

Gating was evaluated for different levels of reduction in motion amplitude, quantified by the duty cycle (DC). This is the fraction of the motion period that is spent in the gating window or, equivalently, the actual dose delivery time as a fraction of the total delivery time which would have been available for irradiation in a non-gating treatment.

The ability of gating to reduce the interplay effect was first tested on a regular $\cos^4$ motion trajectory [272] for two target volumes. The correspondence between DC and motion amplitude for this trajectory is given in table 6.1.

For the spherical target, 38 %, 43 %, 56 % and 100 % DC were investigated. As the results for the smallest two duty cycles were close to the static case, for the patient target, larger DCs were chosen: 43 % 47 %, 56 %, 64 % and 100 %.

Duty cycle [%]	Motion amplitude [mm]
38	1.0
43	1.5
47	2.0
56	3.5
64	5.0
100	10.0

Table 6.1.: Correspondence between duty cycle and peak-to-peak motion amplitude for a trajectory proportional to $\cos^4$.

Re-scanning was applied along with gating to further decrease the interplay effect for large DCs. The main question was whether scaled or iso-layered re-scanning would perform better. Therefore, for the spherical target, 6 times LS and LI with a dwell time of 4 ms were compared. With this dwell time, the highest weighted spots are re-scanned 6 times, which means that the two selected re-scanning methods were expected to perform similarly.

Only layered re-scanning was tested in this experiment because in gating, the various re-scans of each iso-energy layer are likely to be separated in time, at least for the layers that contain highly weighted spots. This is exactly the reason why volumetric re-scanning performs better than layered re-scanning in the context of re-scanning without gating. Therefore, if re-scanning is combined with gating, there should be little difference between layered and volumetric re-scanning. This assertion was tested separately in the next experiment.

Based on the results of the experiment on the spherical target, LI was favoured over LS. The next step was to check if gating combined with LI was also a good strategy for the patient target. As the delivery time of LI was much shorter than for LS, we could also afford comparing LI and VI (with a 4 ms dwell time).

The next goal was to find out if there is any difference in motion mitigation for regularly and irregularly breathing patients. To this end, gating on liver motion of a patient was tested for 33 %, 40 % and 100 % DC and for both the spherical and the patient target. In addition, gating was again combined with 6 times LS and LI with a dwell time of 4 ms. The DCs were smaller for the liver trajectory than for regular motion because, for a fixed residual motion amplitude, the irregular motion spent a smaller fraction of the time in the gating window.

Simulations were run for regular motion with different combinations of DCs and all four types of re-scanning, for both the spherical target and the patient target. For a description of the simulations, see sections 4.2 and 4.1. In the model of the timing of the treatment, the scanning speed and settling time of the sweeper magnets as well as the time for verification of the spot position was taken into account. The time for changing the energy by 3 MeV was assumed to be 80 ms and scaled linearly with the energy step.

The motion amplitude was always set to 1 cm, while the motion period was 6 s for the

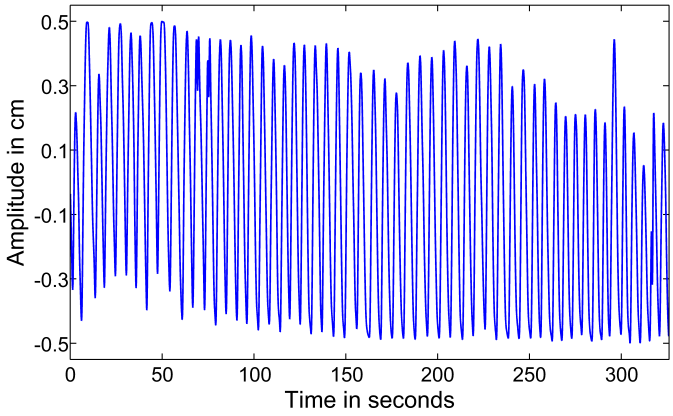

Figure 6.1.: Breathing motion trajectory extracted from 4D-MRI data of a volunteer [287].

regular motion and 6.2 s for the liver motion, see section 6.1.1. Simulations suggested that the motion period has only a small influence on the interplay effect for gating, so this motion parameter was not varied in the experiments.

Reference images without motion were recorded 3 times and averaged. Measurements with gating or re-scanning enabled were taken at least 5 times to start the treatment at several random motion phases. The variability of the dose distributions due to the motion starting phase was expected to be larger without any motion mitigation. Therefore, for measuring motion effects alone, 10 images were acquired.

6.1.1. Patient trajectory

Based on a 4D-MRI data set of a healthy volunteer [286, 67, 287], the motion of the centre of mass of the liver along the superior-inferior (SI) direction was smoothed and re-sampled from the original 3 Hz to the 100 Hz required by the respiratory motion platform. The resulting trajectory is plotted in figure 6.1. The periods of this trajectory were estimated by Fourier transforming the data and ranged from 4.7 s to 7.0 s with the most frequent period at 6.2 s. The trajectory was stretched to cover 10 mm of motion to match the regular trajectory. It corresponds to about 5 min of breathing, which is longer than any of the fields applied for the measurements presented here.

6.1.2. Target volumes

Measurements have been performed for both a spherical and a real target volume. For the first, the CTV was as a sphere with a radius of 3.5 cm. In addition, a more realistic, irregular CTV from a prostate patient has been studied. The CTV of the spherical target was expanded along the direction of motion by 5 mm on both sides, yielding an ITV of 199 ccm, see figure 4.2b. This simple recipe for the ITV is only valid for homogeneous tissue in the beam path. In the case of liver or lung treatment, for example, more

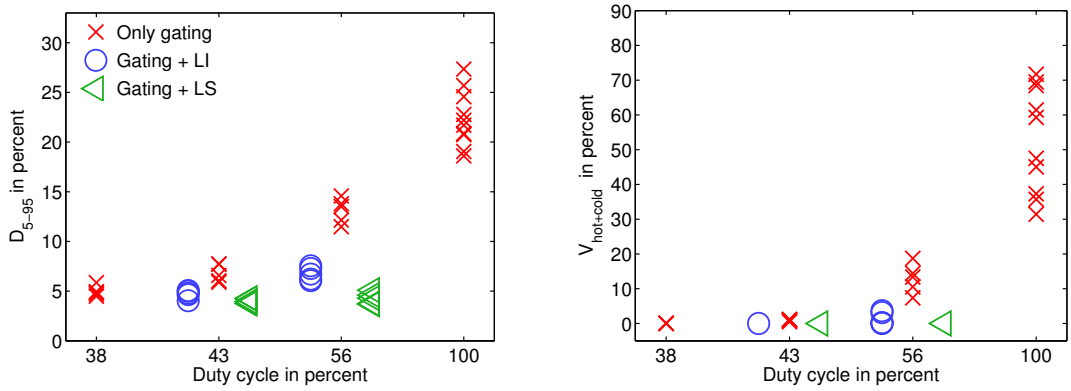

(a) (b)

Figure 6.2.: Interplay effect as a function of gating duty cycle in terms of (a) $D_{5\text{-}95}$ and (b) $V_{hot+cold}$ for 1 cm motion amplitude and the spherical target.

sophisticated approaches are necessary [190, 288, 191]. The ITV of the patient target had already been defined by a physician as an isotropic extension of the CTV by 1.5 cm, resulting in a volume of 99 cm. No planning target volume (PTV) was defined due to the precise set-up of the PMMA phantom. Both target volumes were centred at 10 cm WER.

6.2. Results

6.2.1. Regular breathing

In figure 6.2, the measured values of $D_{5\text{-}95}$ and $V_{hot+cold}$ for the spherical target and for gating alone are shown as the red crosses. As expected, both indices improve (decrease) as the DC decreases. $D_{5\text{-}95}$ dips below 10 % and $V_{hot+cold}$ is close to zero for the two smallest DCs measured.

A larger spread of values per DC was measured for the patient target, as shown in figure 6.3 (again plotted as red crosses), indicating a higher sensitivity to the motion starting phase for the patient target than for the spherical target. Indeed, although $D_{5\text{-}95}$ was generally below 10 % for all DCs, this was not true for some measurements in all but the smallest DC (43 %). Similarly, $V_{hot+cold}$ could be significantly reduced for most measurements, but was as high as 40 % in some cases and no clear correlation between the spread of the values and the DC could be identified. The exception was 43 % DC, where the cold and hot spots were completely washed out in all measurements. Nevertheless, dose homogeneity and cold and hot spots were significantly improved using gating in all cases.

Figure 6.2 (green triangles and blue circles) also shows $D_{5\text{-}95}$ and $V_{hot+cold}$ results for gating combined with both LI and LS re-scanning for the spherical target. From this, it can be seen that re-scanning reduced $D_{5\text{-}95}$ to below 10 % and $V_{hot+cold}$ to below 5 %,

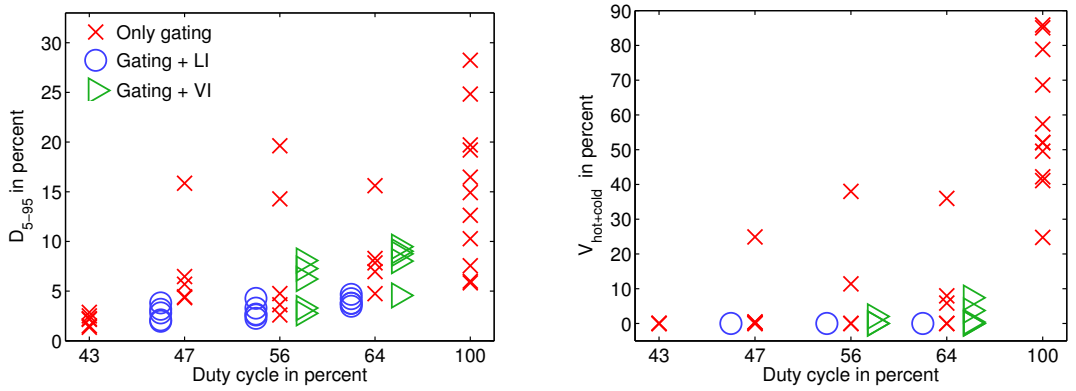

(a) (b)

Figure 6.3.: Interplay effect as a function of gating duty cycle in terms of (a) $D_{5\text{-}95}$ and (b) $V_{hot+cold}$ for 1 cm motion amplitude and the patient target.

even for the largest DC, and resulted in light output distributions comparable to those results from gating alone with the smallest DC. While the results were slightly worse for LI than for LS, it was found that LS took somewhat longer to apply than LI. Therefore, LI was selected for further investigation with the patient target volume. In addition, LI and VI (volumetric re-scanning) were also compared.

The results for gating and re-scanning combined for the patient target volume are shown in figure 6.3 (green triangles and blue circles). From these results, it can be seen that LI performed better than VI, with measured $D_{5\text{-}95}$ values being decreased below 5 % for LI for all tested DCs, and $V_{hot+cold}$ being reduced to close to zero. In contrast, VI reduced $D_{5\text{-}95}$ only to about 10 %, while $V_{hot+cold}$ was also as high as 10 % for the largest DC (64 %). However, if the outliers were removed in the data for gating only, the results would be very similar to gating with VI. In this sense, VI only limited the spread of $D_{5\text{-}95}$ and $V_{hot+cold}$, but not the mean.

6.2.2. Irregular breathing

Figure 6.4 shows the results of $D_{5\text{-}95}$ and $V_{hot+cold}$, again for the spherical target, but this time under conditions of irregular motion using a realistic motion pattern extracted from 4D-MRI data of the liver, as described in section 6.1.1. Interestingly, without re-scanning, $D_{5\text{-}95}$ is more than double for the irregular trajectory than for the regular trajectory at comparable DCs. In addition, there were many cold and hot spots remaining even for the smaller DC (33 %). These were completely blurred for both DCs when combining gating with LS re-scanning, whereas for LI re-scanning, only the smaller DC led to acceptable $V_{hot+cold}$ values below 1.5 %. In addition, the treatment time increased by about 30 % with respect to the regular motion trajectory for equal residual motion.

Figure 6.5 shows the results of the $D_{5\text{-}95}$ and $V_{hot+cold}$ values for the patient target and irregular motion. Motion effects without gating or re-scanning were on average about

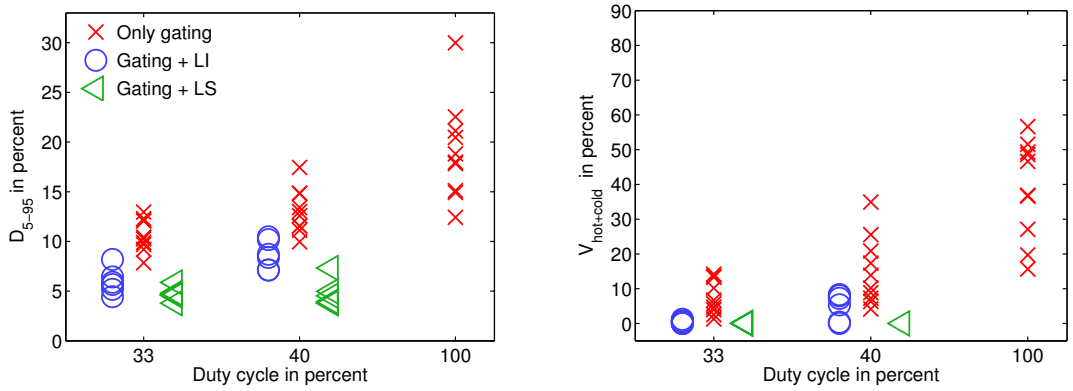

(a) (b)

Figure 6.4.: Interplay effect as a function of gating duty cycle in terms of (a) $D_{5\text{-}95}$ and (b) $V_{hot+cold}$ for liver motion and the spherical target.

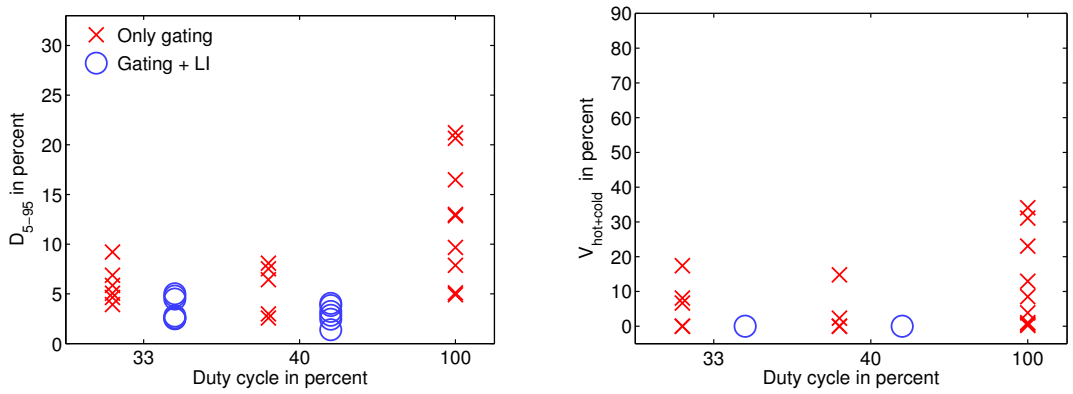

(a) (b)

Figure 6.5.: Interplay effect as a function of gating duty cycle in terms of (a) $D_{5\text{-}95}$ and (b) $V_{hot+cold}$ for liver motion and the patient target.

10 % smaller than for the spherical target volume. However, in line with the results for the spherical target, for gating without re-scanning and at comparable DCs, $D_{5\text{-}95}$ was larger for the irregular trajectory than for regular motion. LI re-scanning recovered the $D_{5\text{-}95}$ to below 5 % and $V_{hot+cold}$ was reduced to zero. No difference between the results for 33 % and 40 % DC were found.

6.2.3. Influence of duty cycle and re-scanning

One of the potential advantages of combining gating and re-scanning is to reduce the overall treatment time. To investigate this, extensive simulations have been performed to study the relationship of dose homogeneity to treatment time for both target volumes

and for the DCs used in the measurements. Only regular motion was taken into account. The dwell time was varied between 0.4 ms and 4 ms for LI and VI, while the number of re-scans was in the range between 2 and 13 for LS and VS.

The results for the spherical target are shown in figure 6.6 for regular motion and DCs of 43 % and 56 %. The results for the patient target were very similar and are not plotted. By drawing horizontal lines, plans with equivalent interplay effect, quantified by $D_{5\text{-}95}$, achieved by different combinations of re-scanning and DC can be identified. Plans on the left of the plot are preferable because it takes less time to apply them. No error bars were displayed for the sake of clarity. In fact, minimum-maximum bands are rather wide for DCs above 60 % due to the increasing influence of the motion starting phase. The horizontal grey line shows the value of $D_{5\text{-}95}$ in the case of no motion.

Figure 6.6a illustrates that for a DC of 56 %, LI is clearly superior to LS, reaching lower values of $D_{5\text{-}95}$ in less time. However, for 43 %, these two methods perform very similarly. It can be seen that reducing the DC is a much better strategy than increasing the number of re-scans for LS, while for LI, both approaches are possible, with a small advantage in favour of lowering the DC.

VI and VS re-scanning are compared in figure 6.6b. In general, these two re-scanning methods lead to similar values for $D_{5\text{-}95}$. For 56 % DC, VI performed slightly worse than LI, while VS lead to lower values of $D_{5\text{-}95}$ than LS at the cost of longer treatment times. For certain numbers of re-scans of VS, large spikes occur. Again, lowering the DC is the better choice, but this advantage is lost for a high enough number of re-scans, starting at about 200 s of delivery time.

6.3. Discussion

The effectiveness of gating and re-scanning in mitigating the interplay between beam scanning and tumour motion has been investigated for a spherical and a patient target volume by experiment. Both a regular and a liver motion trajectory from a patient were applied.

Gating without re-scanning only led to clinically acceptable results for the spherical target, for a regular motion trajectory and for a small enough duty cycle. Therefore, gating should be combined with re-scanning. Although gating alone was not very efficient at reducing the interplay effect for the patient target, together with re-scanning, results comparable to the case without motion could be achieved. For liver motion, the interplay effect was even larger than for regular motion. As a result, re-scanning was also necessary for both target volumes.

Based on simulations of regular motion, it was found that reducing the DC is a better strategy than increasing the amount of re-scanning, on the grounds that treatment time is smaller for the same dose homogeneity. A DC of 43 % and LS re-scanning with a dwell time of 4 ms seemed to be a good choice for both studied target volumes. Little improvement could be achieved by choosing a smaller DC or by applying more re-scans. As expected, using VS instead of LS and VI instead of LI was not beneficial and just increased treatment time due to the higher number of energy changes, which is the

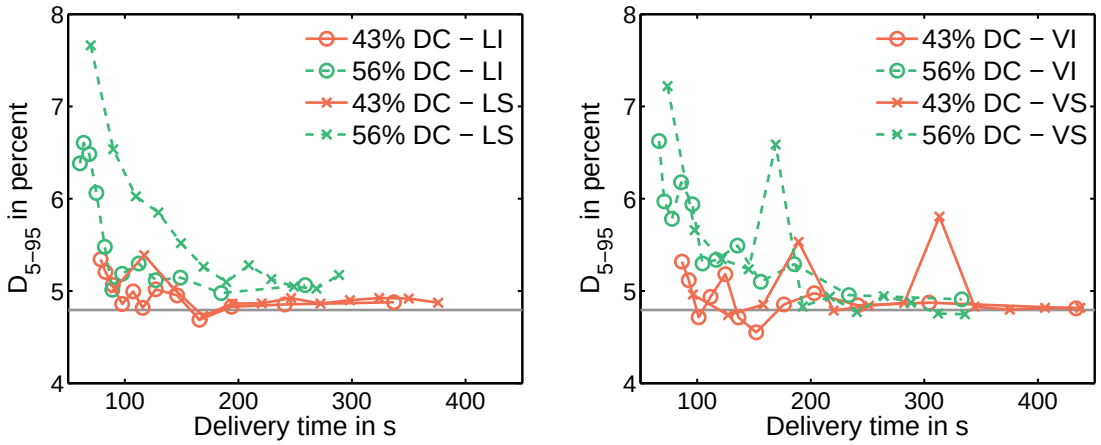

(a) LI vs LS (b) VI vs VS

Figure 6.6.: Simulated $D_{5\text{-}95}$ as a function of the application time. For the spherical target, different re-scanning methods are compared. On the plots, from left to right along the lines, the markers represent dwell times ranging from 4 ms to 0.4 ms and numbers of re-scans from 2 to 13. The grey line indicates $D_{5\text{-}95}$ for the case without motion. The plotted data is the mean from 36 different motion starting phases.

slowest scanning axis of almost all proton therapy systems.

As discussed in section 5.3, the spikes in the simulated $D_{5\text{-}95}$ values for certain numbers of VS re-scans are due to the interference between periodic motion and scanning of the target volume at a similar frequency. This effect was much less prominent in the experiments than predicted by the simulations, see section 5.2.2.

It is important to test gating efficiency with realistic motion trajectories and target volumes. Otherwise, motion effects are severely underestimated. In principle, tumour motion trajectories could be extracted from 4D-CT or 4D-MRI and then applied to the respiratory motion platform for a couple of DCs before the first treatment fraction. This would help choose an appropriate DC. On the other hand, this type of quality assurance would consume a lot of beam time and manpower.

LI re-scanning should be combined with gating because it does not increase the treatment time so much as with volumetric or scaled re-scanning. For 6 times scaled re-scanning, VS takes about 10 % longer than LS, depending on the DC, while for iso-layered with 4 ms dwell time, VI increased the treatment time by about 7 % as compared with LI. These values depend slightly on the DC. The fact that scaled re-scanning lead to better measured dose homogeneity than iso-layered re-scanning is mainly due to the selection of the number of re-scans and the dwell time, respectively, specific to this experiment. For a dwell time of 4 ms, the most highly weighted spots of the spherical target were re-scanned 6 times for iso-layered re-scanning. Lower weighted spots were re-scanned less, which is in contrast to scaled re-scanning, where all spots were re-scanned 6 times,

irrespective of their weight.

In principle, very small DCs could be chosen to improve the results for gating without re-scanning. First, this would result in long treatment times, especially for realistic, irregular motion. Second, no motion surrogate is as accurate as in our simple set-up. A small DC would in this case increase the chance of a complete miss of the tumour. For this reason, a small duty cycle might not even be feasible.

The main purpose of volumetric re-scanning is to make sure that the motion state for the re-scans of a spot is always different so that no hot or cold spots can be formed. This purpose is served by gating as a side effect unless the duration to scan an energy layer once matches the duration of the gating window. In this case, if the scan path is reversed after a re-scan, on every other re-scan a spot is applied to the same position in the target, which probably is not the intended spot position. If the motion is not regular, the gating windows have a varying duration, so this interplay is highly unlikely. Generally, the only difference between gating with layered re-scanning and gating with volumetric re-scanning is the higher fraction of the gating window allotted to the energy change. Further investigation might find that the apparent disadvantage of VI over LI re-scanning for the patient target is due to the low statistics of the measurements presented here. Simulations suggested that it depends on the DC if one or the other is better.

For larger target volumes and several field directions, the treatment will take longer than for our measurements. In this case, the baseline of the motion will drift in time [286] and also the organs themselves will undergo deformations [171]. The motion surrogate also does not allow the determination of the target volume position as accurately as in the simple set-up of this study.

The measurements presented in this work should be repeated for various motion trajectories and targets taken from real patients. Preferably, data at several depths would be acquired, as motion effects generally increase from the proximal end to the distal end of the target volume.

It would also be interesting to investigate experimentally the optimal amount of re-scanning as a trade-off between treatment time and motion mitigation.

6.4. Conclusion

The effectiveness of mitigating the interplay effect by gating has been evaluated for a proton spot scanning treatment in a homogeneous phantom. While gating alone was effective in the simple case of a spherical target volume and regular motion, gating efficiency dropped for a patient target volume and a realistic patient motion trajectory. In general, re-scanning is necessary for a safe and robust application of gating. In terms of treatment time, it is better to reduce the duty cycle, i.e., the size of the gating window. However, in real patient treatments, there is likely a lower limit to the duty cycle, so increasing the amount of re-scanning is a more robust option to control motion effects. Layered re-scanning performed slightly better than volumetric re-scanning, although simulations predicted a dependency on the duty cycle. When combined with gating,

iso-layered re-scanning is preferable over scaled re-scanning because it achieves the same dose homogeneity in less time. The reduction in treatment time depends on the duty cycle. For small duty cycles, this benefit is small.

7. First experimental results of motion mitigation by continuous line scanning

The major factor in increasing treatment time in the case of re-scanning is the dead time of beam scanning, where no dose is applied to the patient. Two factors contribute to this dead time: first, the time that is needed to laterally advance the beam to the next spot, and second, the delay in adjusting the beam energy. A different beam delivery approach cancels the first contribution to the dead time by continuously scanning the beam along lines in iso-energy layers.

It has been shown *in silico* that re-scanning with continuous line scanning is superior to discrete spot scanning in terms of motion mitigation and treatment time [110]. First experimental results on the feasibility of this approach have been obtained on Gantry 2 in the context of simulated scattering [44].

In this chapter, we expand on this theoretical and experimental work and address the following questions:

- Can identical dose distributions be achieved with continuous line scanning as with discrete spot scanning?
- Is it advantageous to use continuous line scanning or simulated scattering instead of discrete spot scanning to mitigate motion effects by re-scanning?
- Is there a difference between evaluating re-scanning on a geometric and a realistic target volume?

7.1. Outline of performed measurements

For all measurements, the motion trajectory was proportional to the function $\cos^4$ [272] with a peak-to-peak amplitude of 1 cm.

A prescribed dose of 1 Gy was used throughout the measurements. The spacing between adjacent lines in the lateral plane was 0.5 cm, which matches the lateral spot spacing. In depth, a fixed separation of the iso-energy layers of 0.45 cm was used.

Three reference images without motion were taken and averaged for each experiment. The experiments with motion were conducted 6 times for the spherical target, randomly sampling the motion starting phase. For the liver target and for simulated scattering, motion without re-scanning was sampled 10 times.

7.1.1. Continuous line scanning

The dose delivered by continuous line scanning was checked against discrete spot scanning at the central lateral plane of a cubic target of 10 cm side length. It was assumed that the system had already been calibrated properly for spot scanning, meaning that for a spot scanning plan, the measured dose should be equal to the planned dose within a small error of, e.g., 1 %. Instead of comparing absolute dose at single points with an ionisation chamber, the light output of the scintillating screen measured by the CCD camera was taken as a surrogate. Equal light output for spot and line scanning implies equal dose. This method yields high-resolution two-dimensional data.

Different numbers of re-scans for line scanning were compared. The result is given in terms of the mean and standard deviation of the difference to spot scanning without re-scanning. The values are scaled by the median value in the analysis region for spot scanning. The analysis region was defined as the target contour minus a margin of 1 cm to avoid any dose gradients at the edges of the target volume.

A single, homogeneous energy layer of 128 MeV was applied with spot and line scanning at the iso-centre in air to compare the penumbra to the theoretical prediction, based on a summation of narrowly spaced Gaussian curves, and the value obtained by the dose calculation, which approximates pieces of line segments as the superposition of two error functions, as explained in section 4.1.6. The Gaussian beam width for this set-up was 3.2 mm.

The effectiveness of line scanning for alleviating the interplay effect by volumetric scaled re-scanning was tested on two target volumes. The first target volume was a spherical CTV with radius 3.5 cm. In the direction of motion, the CTV was extended by a margin of 5 mm to an ITV with a volume of 199 ccm. No PTV was added, assuming perfect patient set-up and machine precision. Second, a target volume from a liver patient was selected with a CTV of 122 ccm. A physician had already added an isotropic margin of 1.5 cm to the CTV, defining a PTV with a volume of 439 ccm. This PTV was taken to cover the CTV in any motion phase. Both target volumes were centred at 13 cm WER.

For the spherical target volume, the breathing period was set to 6 s. In order to have more realistic measurements, this was changed to 4 s for the liver target. The two targets figure as two different patients, who are likely to breathe differently.

Furthermore, line scanning was compared with spot scanning for the spherical target volume. All of these measurements were taken at a WER of 13 cm and with a motion period of 4 s. The number of re-scans was set to (1, 6, 8, 10, 12) for discrete spot scanning and (1, 6, 10, 15, 20) for continuous line scanning. Please note that here re-scanning once means scanning once through the target, not twice.

7.1.2. Simulated scattering

For all measurements with simulated scattering, the target volume was a sphere with radius 3.5 cm, centred at a WER of 12 cm. The collimator and compensator have been described in detail in another work of our group [24]. The collimator is made of copper

and blocks all protons. PMMA was used in the construction of the compensator. No dedicated ITV was included in the design of the collimator and compensator. Therefore, we decided to define the outer 5 mm of the sphere as the ITV. The CTV thus becomes a sphere with radius 3 cm.

The correctness of the delivered dose was measured similarly to what has been described in section 7.1.1 for continuous line scanning. However, the target volume was a sphere. Because no compensator is required to shape a cubic target volume, this case was not studied here. Apart from the collimator, simulated scattering is equivalent to continuous line scanning for cubic targets.

The measurements were first performed without re-scanning and with combined re-scanning, with and without an expanded scanning area. For the expanded scanning area, no additional dose was applied, but for each line, scanning started 1 cm before dose delivery and ended 1 cm after dose delivery. The idea behind this is that the sweeper magnets, which are used for scanning the beam in the lateral plane, need some time to reach the maximum scanning speed. For a large number of re-scans, the magnets are scanning close to or at the maximum scanning speed. Therefore, it was expected that the lateral expansion of the scanning area could help reduce the penumbra and dose inhomogeneity at the edges of the target volume. The analysis was performed in a circular ROI with radius 3 cm. This ROI was located at a WER of 12 cm, at the centre of the target volume.

The penumbra for simulated scattering was determined at a WER of 10 cm. The influence of an expanded scanning volume was also determined. In this experiment, the penumbra of the full target volume was assessed after passing through considerable amounts of PMMA, in contrast to the experiment for line scanning, where the penumbra was measured at a single energy and in air. This is because the compensator changes the range of the protons that make up an iso-energy layer. The size of this range shift depends on the lateral position. In our case, where the purpose of the compensator is to shape the iso-energy layers so that they generate a spherical target volume, the range of the protons after their passage through the compensator would be maximal in the centre and decrease with increasing distance from the centre. Since the signal in the scintillating screen depends on the stopping power and, hence, on the range of the protons, the measured distribution would be highly inhomogeneous.

Motion effects and the influence of re-scanning were measured at 12 cm and 13.5 cm WER. The analysis ROIs at these two depths are termed *central* and *distal* ROI, respectively. Re-scanning for simulated scattering has been implemented as a combination of scaled and iso-layered re-scanning [44]. This is a type of mixed re-scanning as introduced in section 3.2 where the field is first scaled re-scanned, yielding a certain number of identical copies of the original field with a correspondingly lower weight. Each of these copies is now iso-layered re-scanned. On top of this, volumetric re-scanning is applied so that the energy is changed after each scan of an iso-energy layer. This type of re-scanning will be referred to as *combined re-scanning*. Figure 7.1 shows the variation of the beam energy with time for combined re-scanning. This may clarify the order of delivery of the re-scanned iso-energy layers.

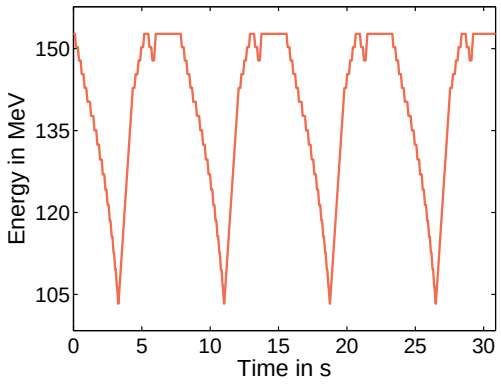

Figure 7.1.: Beam energy sequence as a function of the delivery time. Combined re-scanning is applied to the spherical target volume, delivered with simulated scattering. In this example of combined re-scanning, volumetric iso-layered re-scanning is repeated four times.

Motion mitigation was assessed for combined re-scanning, where iso-layered re-scanning with a dwell time of 0.4 ms was repeated four times, resulting in a total number of re-scans of about 50 for the most distal iso-energy layer. The influence of the lateral expansion of the scanning area was evaluated for the central ROI.

7.2. Results

7.2.1. Dosimetry

Continuous line scanning

On average, the light output was higher for line scanning than for spot scanning by about 0.5 % for up to 20 re-scans, as shown in figure 7.2a. For 50 re-scans, however, the mean error increased to about 2 %. The standard deviation over all the evaluated pixels grew larger with the number of re-scans. To put these values into perspective, if the same dose distribution is applied and captured several times, the measurements are not exactly identical. This is due to noise in the read-out of the CCD camera, fluctuations in amount and position of the delivered dose, leading to a standard deviation of 0.3 %. This statistical error is of the same order as the mean systematic error reported above for the difference between spot and line scanning. The homogeneity of the dose distributions was about 1 % for all measurements, except for 50 re-scans, where it was about 0.9 %.

The results for the penumbra measurements are given in table 7.1. As expected, the penumbra for spot scanning is almost the same both parallel and perpendicular to the primary scanning direction. The penumbra for line scanning differs from spot scanning only parallel to the primary scanning direction, where an increase of 16 % was measured. The measured penumbrae reproduced the theoretical values for spot scanning parallel to the primary scanning direction. In the other cases, the deviations stayed below 0.2 mm.

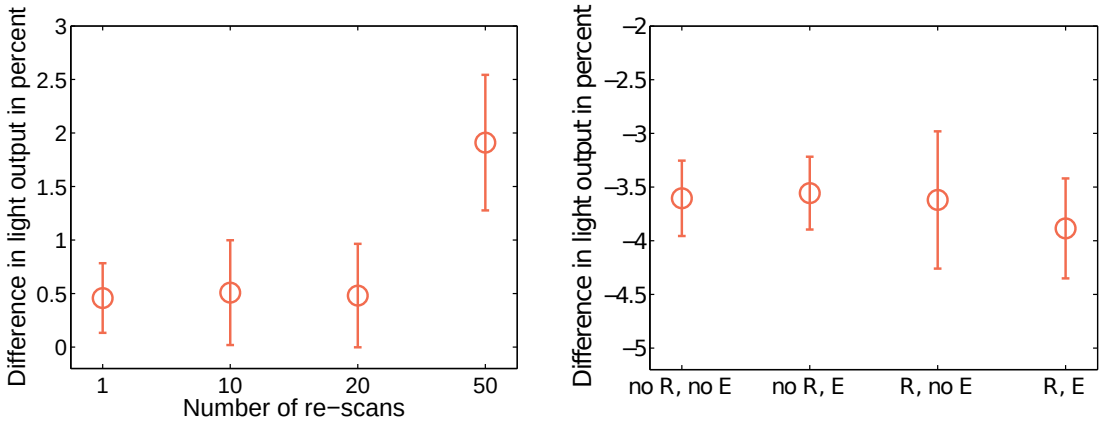

(a) (b)

Figure 7.2.: Mean difference in light output to spot scanning as a function of the number of re-scans for (a) continuous line scanning and for different combinations of no re-scanning (no R), combined re-scanning (R), no lateral expansion of the scanning area (no E) and lateral expansion (E) for (b) simulated scattering. No re-scanning is applied to spot scanning. Spot scanning is considered to be the gold standard, i.e., it is assumed that for planned dose of 1 Gy, exactly 1 Gy is measured. The plotted value is the average difference over all evaluated pixels. The error bars indicate one standard deviation.

The error on the measured values is purely statistical and arises from averaging the penumbra along the edges of the rectangular dose distribution. For the dose calculations a finer dose grid gave results closer to the theoretical penumbra width.

Dose profiles and penumbrae for spot and line scanning are plotted in figure 7.3. Note that the penumbra for 50 re-scans is smaller along the primary scanning direction. This is due to the overshoot of the actual beam intensity, introduced by the control loop, for step changes in the nominal beam intensity. This leads to edge enhancement and a smaller penumbra since these steps occur mainly at the edge of the target volume.

Simulated scattering

The average light output was 3.5-4 % lower for simulated scattering than for spot scanning, as presented in figure 7.2b. Without re-scanning, the variation within the ROI was comparable to the results from line scanning. Lateral expansion of the scanning area only had a small effect. For combined re-scanning, both the mean difference and the standard deviation increased. Here, lateral expansion slightly reduced the standard deviation at the expense of a larger mean difference in light output.

The penumbra along the central profiles is listed in table 7.2 without and with lateral expansion of the scanning area. Two values are reported for each measurement. These correspond to the penumbrae of each of the two opposing edges of the dose distribution.

Method	Penumbra [mm]	
	Parallel to scanning	Perpendicular to scanning
	Discrete spot scanning	
Theory	4.72	4.72
DC on 1 mm grid	4.66	4.66
DC on 2 mm grid	4.64	4.64
Measurement	4.68 ± 0.11	4.88 ± 0.08
	Continuous line scanning	
Theory	5.32	4.72
DC on 1 mm grid	5.30	4.66
DC on 2 mm grid	5.26	4.66
Measurement	5.43 ± 0.09	4.82 ± 0.07

Table 7.1.: Penumbra of a single-energy layer parallel and perpendicular to the faster, primary scanning direction for discrete spot scanning and continuous line scanning. Measured values are compared with the theoretical prediction and the dose calculation (DC) on two dose grids with different grid spacing.

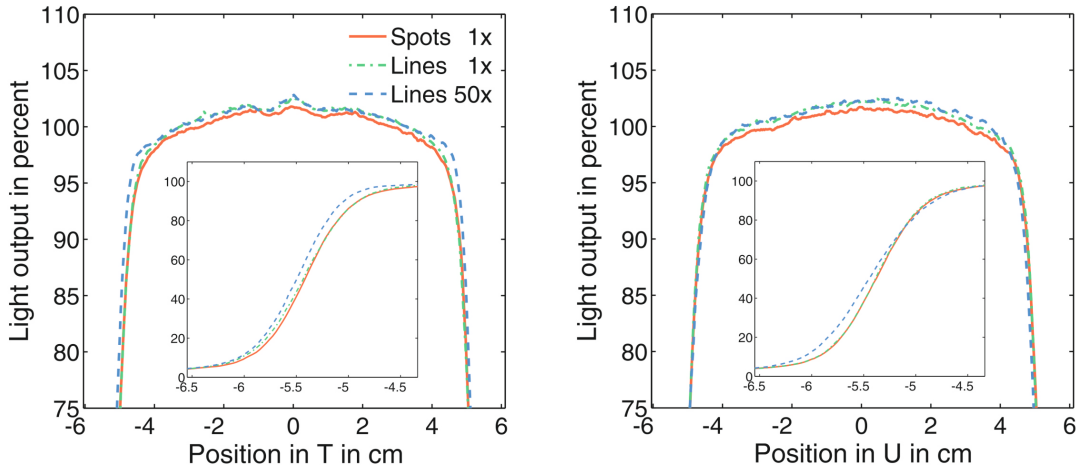

(a) (b)

Figure 7.3.: Profiles along (a) T and (b) U for single-scan discrete spot scanning and continuous line scanning with 1 and 50 scans. Inset is the left penumbra. Plotted is the light output relative to the median light output of a uniform cubic field applied by spot scanning.

Method	Penumbra [mm]	
	Parallel to scanning	Perpendicular to scanning
	No re-scanning	
Spots	8.8/9.1	9.1/8.9
Lines w/o expansion	8.9/9.2	9.2/8.9
Lines w/ expansion	8.9/9.2	9.2/8.9
	Combined re-scanning	
Lines w/o expansion	8.6/8.1	9.0/8.9
Lines w/ expansion	8.8/8.7	9.1/9.0

Table 7.2.: Penumbra of the central profiles parallel and perpendicular to scanning. The measurements were taken at the central plane at a water-equivalent depth of 10 cm. Two values are given for each measurement for both opposing edges of the dose distribution, i.e., left/right edge and upper/lower edge. Shown are the results for simulated scattering without and with lateral expansion of the scanning area. Combined re-scanning was applied as explained in the text. In addition, discrete spot scanning was compared, also applied with the collimator and compensator. The error in measuring the penumbra is about 0.1 mm.

As a comparison, the penumbra of the field applied by spot scanning is also given. Without re-scanning, the penumbra for line scanning is within 0.1 mm of the penumbra for spot scanning. The only measurable difference occurred for combined re-scanning along the primary scanning direction T, perpendicular to motion. Here, the penumbra recovered by 0.6 mm when the scanning area was expanded.

7.2.2. Re-scanning

Continuous line scanning

As presented in figure 7.4, 10 times re-scanning reduced $D_{5\text{-}95}$ to below 5 % for both targets. More re-scans did not improve this value. For the spherical target and 20 re-scans, some measurements had $D_{5\text{-}95}$ above 5 %. The same happened also for the liver target and 15 re-scans. Generally, the spread in $D_{5\text{-}95}$ was very small for 10 or more re-scans. The results for $V_{\text{hot+cold}}$ are analogous: 10 re-scans removed all hot and cold spots for both targets. However, for more re-scans, up to 5 % $V_{\text{hot+cold}}$ was measured. The median light output, compared to the light output distributions without motion, was very stable for the liver target, irrespective of the number of re-scans. By contrast, a linear increase in median light output was observed for the spherical target, culminating in a small over-dosage of about 1.5 % for 20 re-scans.

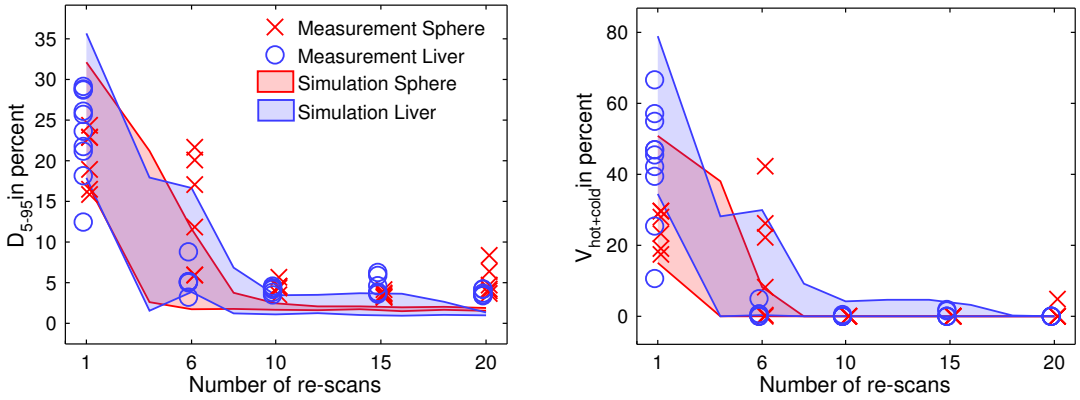

(a) (b)

Figure 7.4.: $D_{5\text{-}95}$ (a) and $V_{hot+cold}$ (b) as a function of the number of re-scans for 1 cm motion amplitude. Results for both a spherical target and a liver target are shown. The fields have been applied with continuous line scanning. For the simulations, the area between the minimum and maximum values out of 36 different starting phases was shaded, restricted to the two-dimensional region of interest of the measurement.

Comparison of continuous line scanning and discrete spot scanning

Spot scanning and line scanning lead to very similar results for the spherical target. These results are shown in figure 7.5. $D_{5\text{-}95}$ was below 5 % for 10 and more re-scans and no hot or cold spots were seen for 8 and more re-scans. $D_{5\text{-}95}$ and $V_{hot+cold}$ were overlapping for both methods. The simulations predicted that for spot scanning, the light output distributions would become worse between 6 and 8 re-scans and then dramatically improve between 8 and 10 re-scans. This behaviour could not be verified by measurements.

For no re-scanning, the treatment time for line scanning was less than 55 % of the one for spot scanning. For more re-scans, line scanning grew more efficient up to 10 re-scans, where the ratio attained its minimum at 30 %, see figure 7.6.

7.2.3. Simulated scattering

From figure 7.7 it is clearly visible that re-scanning applied by simulated scattering reduced both the spread and average value of $V_{hot+cold}$. However, only for the central ROI were all hot and cold spots removed. For the distal ROI, hot and cold spots amounted to not more than 2 % in one case and were averaged out in all other cases. $D_{5\text{-}95}$ was below 5 % for both the central and the distal ROI. For both statistics, there is a trend for worse values with WER of the analysis ROI. The median light output was 1.7 % lower in the distal ROI than in the central ROI. This difference boils down to quenching of the light output in the scintillating screen, see section 4.3.2. The value predicted by simulations was 1.6 %.

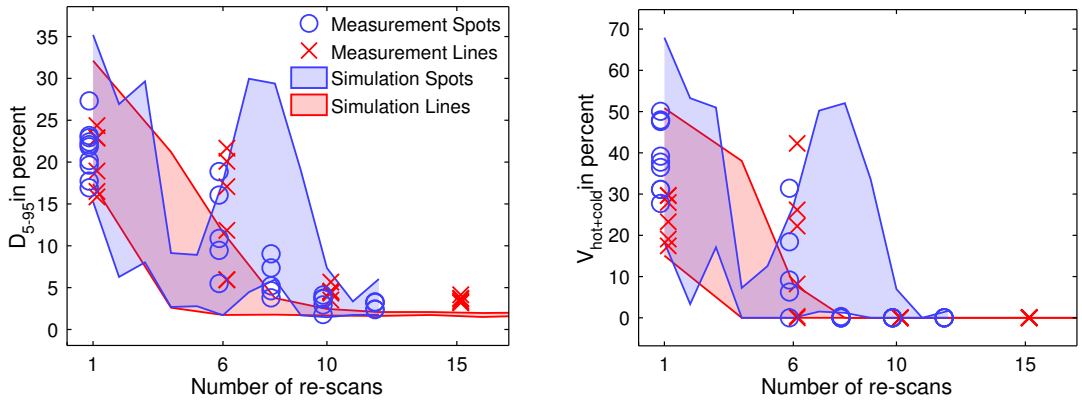

(a) (b)

Figure 7.5.: $D_{5\text{-}95}$ (a) and $V_{hot+cold}$ (b) as a function of the number of re-scans for 1 cm motion amplitude. Results for both discrete spot scanning and continuous line scanning are shown. For the simulations, the area between the minimum and maximum values out of 36 different starting phases was shaded, restricted to the two-dimensional region of interest of the measurement.

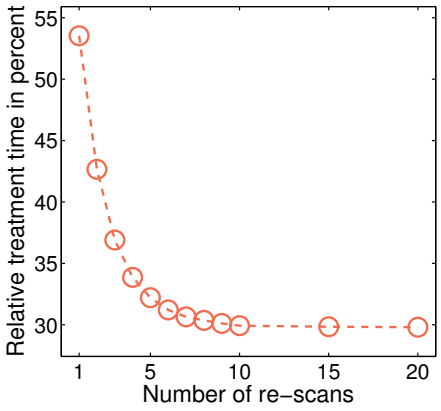

Figure 7.6.: Treatment time for continuous line scanning as a percentage of the treatment time for discrete spot scanning. All values are according to simulations.

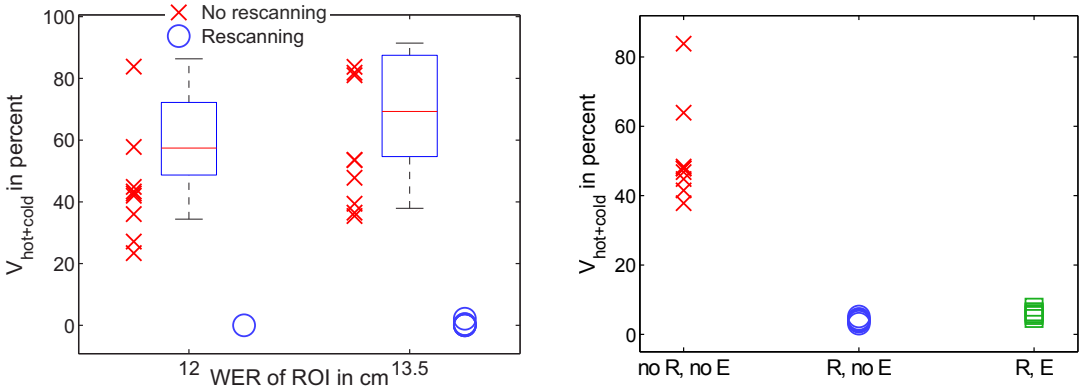

(a) (b)

Figure 7.7.: Interplay effect for simulated scattering and combined re-scanning in terms of $V_{hot+cold}$ for (a) two different depths and for (b) no re-scanning and no lateral extension of the scanning area (no R, no E), combined re-scanning and no extension (R, no E) and combined re-scanning and extension (R, E). The motion was set to an amplitude of 1 cm and a period of 4 s. Each marker represents a single measurement. The box plots in (a) shows the simulated data for 36 equally distributed motion phases. For re-scanning, the simulation predicts zero $V_{hot+cold}$. This data is omitted.

Laterally expanding the scanning area improved the dose distributions only modestly, as shown in figure 7.7b. Based on a central ROI encompassing the collimator opening, i.e., a circle with radius 4 cm, $D_{5\text{-}95}$ was lowered merely by 0.5 %. A slightly larger improvement was measured for $V_{hot+cold}$, where the lateral expansion resulted in a value lower by 1.8 %. Finally, median light output increased by 0.8 %.

7.3. Discussion

The efficiency of re-scanning to mitigate the interplay effect has been verified for continuous line scanning on two target volumes and compared with re-scanning for discrete spot scanning for the spherical target volume. In addition, motion mitigation by simulated scattering has been investigated.

Agreement in average dose between spot and line scanning within 1 % was achieved. For both targets, 10 times volumetric re-scanning was able to mitigate the interplay effect for a motion amplitude of 1 cm. A slight increase in median light output with the number of re-scans was found for the spherical target. For 10 re-scans, it was negligible. No difference between spot and line scanning considering their power to mitigate motion effects was seen for the spherical target.

The fact that the average dose was slightly larger for line scanning than for spot scanning can be explained by the sensitivity of the absolute dose to the air temperature and pressure in the dose monitor. At the moment, this correction is applied on-line for

spot scanning, but for line scanning this happens during treatment planning because line scanning is still under development. If the conditions change between treatment planning and application on the gantry, the absolute dose will be off. As a rule of thumb, a difference of 1 % in absolute temperature or pressure causes a change of 1 % in the dose. This rule is based on the fact that the amount of charge collected by an ionisation chamber is proportional to the gas density in the sensitive volume of the chamber.

The larger error in average dose for 50 re-scans is likely due to the performance of the deflector plate. For such a large number of re-scans, the speed of the beam is at its maximum, while the beam intensity is reduced. During the time it takes for the control loop to adjust the beam intensity, which is about 1 ms, a large distance is covered by the beam and spreads the dose error over a large part of the target. Reducing the maximum scanning speed would help, but this would also increase the treatment time. However, such a high number of re-scans will probably never be used in practice because it does not seem to be necessary for mitigating moderate motion. An exception is simulated scattering.

The deviations of the measured penumbra to the calculated values are probably due to the uncertainty on the beam width that has been used for the theoretical and the dose calculations and imperfections in the beam delivery. What is more, spots are not perfect Gaussian curves and are not rotationally symmetric as assumed by the calculations. Although using a higher resolution of the dose grid yielded values closing in on the theoretical penumbra, this would also come at the cost of longer calculation time. The observed difference is most likely insignificant in practice even for a 2 mm dose grid.

The average dose for simulated scattering showed a relevant shift of up to 4 % with respect to spot scanning. This could be a problem of variable pressure and temperature in the treatment room, as this had to be corrected offline for simulated scattering. However, this is probably not enough to explain all of the observed discrepancy. Another cause could be the use of a compensator. First, it leads to a different energy distribution of the protons that deposit dose in the measurement plane. Because the quenching effect depends on the energy, this alters the light output that is generated in the scintillating screen. Second, the beam width at the measurement plane is larger than for measurements without a compensator. This is because there is an air gap between the compensator and the PMMA blocks in the set-up of our experiment. Protons that are scattered in the compensator, most importantly due to multiple Coulomb scattering, drift away from their initial lateral position in the air gap.

When using a collimator and a compensator, the penumbra is the same for both spot and line scanning, except for combined re-scanning in the scanning direction. In this case, laterally expanding the scanning area, while keeping the dose delivery untouched, recovers the penumbra in the scanning direction.

The penumbra for the spherical target, measured at 10 cm WER, was about twice as large as for the single-energy layer, which was measured in air. The fact that the penumbra differed between one side of the target volume and the other side indicates that the treatment field was not perfectly centred with respect to the collimator and

compensator.

As motion mitigation performance was comparable for spot and line scanning in our set-up, the advantage of the latter is a treatment time as small as 30 % of the time for spot scanning for 10 and more re-scans. On the other hand, only one target and one motion trajectory has been checked. Simulations have indicated that line scanning mitigates the interplay effect even better than spot scanning for the same number of re-scans [110], depending on the target volume. For the target size chosen in this work, this effect was not predicted. A possible explanation is that a typical iso-energy layer is re-scanned in less than 300 ms by line scanning. Since motion on this time scale is small, each iso-energy layer is homogeneous. These layers are still shifted with respect to each other but the overall dose homogeneity is better than if the layers themselves were in addition inhomogeneous.

For both the geometric spherical target volume and the realistic liver target volume, the motion mitigation performance of re-scanning was very similar. Therefore, the results on line scanning should not depend on the shape and size of the target volume of a patient.

It is known from simulations that if beam scanning and tumour motion have a similar period, the interplay effect is enhanced for certain re-scan parameters, especially for volumetric re-scanning [110, 289]. This resonance effect was predicted by our simulations only for spot scanning, probably because the time to apply one re-scan of the whole target volume was closer to the motion period for spot scanning than for line scanning. In the measurement results, however, this effect could not be reproduced. Because the motion period varied with a standard deviation of 300-400 ms, the interplay between motion and scanning was not perfectly reproducible from re-scan to re-scan, as it was assumed by the simulation program.

The selected re-scanning approach for simulated scattering was almost sufficient for alleviating the interplay effect for the spherical target. A very small amount of cold and hot spots remained for 1 cm motion amplitude. Although it is technically possible to choose an even higher number of re-scans for simulated scattering, it is not safe to say that this would result in more homogeneous dose distributions. What is more, in the application of such re-scanning the beam intensity would have to be reduced because the sweeper magnets could not scan the beam faster. In turn, this would limit the efficiency in beam usage. Another option is the introduction of an ITV to cover the motion by a margin. To this end, a new set of collimator and compensator would have to be produced. More interesting, though, would be the combination of re-scanning and gating. The lateral expansion of the scanning area did not show large benefits in terms of penumbra and dose homogeneity. The drawback of this approach is a slightly increased time for field delivery.

In the future, better conformity of the dose distribution to the target may be achieved by scanning along the contours of the target volume. Typically, in the central part of the target volume, spot weights are smaller because several distal spots contribute to the dose at this position. When scanning along straight lines, the beam intensity can be very dynamic. This is a challenging situation for the deflector plate. Contour scanning may

be a better solution, where the beam follows the contour of the target volume. Because the iso-dose lines are often also parallel to the target contour, the beam intensity would be almost constant.

At the moment, there is no on-line verification in place for line scanning. Verification of the applied dose during scanning is a major challenge because the beam covers up to $2\,{}^{\mathrm{cm}}/_{\mathrm{ms}}$. Fast detectors and electronics are required. As a first step, verification will probably take place after the application of each line. One advantage of re-scanning is that if the applied dose profile in a re-scan does not match the requested dose profile, it could be corrected in the subsequent re-scan.

7.4. Conclusion

Continuous line scanning was shown to mitigate the interplay effect by re-scanning for motion of up to 1 cm. The results were consistent between the two target volumes checked. The average dose and the penumbra were in sufficient agreement with the values obtained by discrete spot scanning. Dose homogeneity as a function of the number of re-scans decreased in a similar fashion as for discrete spot scanning. Treatment time was shortened by a factor of 3 for 10 and more re-scans.

Simulated scattering was shown by experiment to be able to deliver dose distributions comparable with spot scanning, except for a shift in average dose of about 4 %. This needs more investigation. Even when many volumetric re-scans were applied, up to 50 re-scans for the most distal iso-energy layer, the dose distributions were sufficiently homogeneous. Re-scanning clearly reduced the amplitude and spread of motion effects for a motion amplitude of 1 cm and nearly all cold and hot spots could be averaged out.

Further improvement in motion mitigation or an application to larger motion amplitudes should be based on a combination of gating and re-scanning. Since the measurements have been performed in a homogeneous phantom, care has to be taken in transferring to clinical cases the results presented here.

8. Conclusion and Outlook

In the preceding sections, experimental evidence has been gathered to assess the effectiveness of re-scanning and gating in the treatment of tumours by scanned proton therapy in the presence of organ motion in a homogeneous phantom.

It has been shown by direct measurements using discrete spot scanning that re-scanning is able to mitigate motion of up to 10 mm for a spherical target. Volumetric scaled re-scanning turned out to be the best method, whereby the beam is scanned through the whole target volume in each re-scan (volumetric) and the weights of the re-scanned spots are calculated by dividing the original weights by the number of re-scans (scaled).

For proton therapy facilities which cannot rely on fast energy modulation, volumetric re-scanning is not feasible as it would lead to very long treatment times. For motion amplitudes of up to 5 mm, layered, iso-layered re-scanning is recommended, where all re-scans of an iso-energy layer are applied directly after each other (layered) and the dose per spot is constant for all re-scans (iso-layered).

Gating performed satisfactorily for a spherical target volume and regular, periodic motion. In less academic circumstances, re-scanning was necessary to reliably achieve acceptable dose distributions. To this end, iso-layered re-scanning should be favoured, as the treatment time, which is already stretched due to gating, does not increase as much as with scaled re-scanning. There is no benefit of volumetric re-scanning as gating already introduces large enough shifts in motion phase between subsequent re-scans of iso-energy layers.

Continuous line scanning has been shown to be a promising technology to overcome an existing limitation of discrete spot scanning, the inherent dead time due to scanning the beam from spot to spot, especially in the context of re-scanning. The outcome was consistent for both a regular spherical target volume and an irregular liver target volume. The treatment time could be reduced by up to 70 % with respect to spot scanning. The larger the number of re-scans, the higher was the reduction in treatment time. The maximum reduction was achieved at about 10 re-scans and remained at that level for more re-scans.

Scattering proton therapy was simulated on Gantry 2 by applying line scanning with a high number of re-scans to a collimator and a compensator. Even if the control of the absolute dose is still an issue, motion of 1 cm amplitude could be mitigated by this simulated scattering.

The effect of re-scanning on the dose distributions is reasonably predictable by simulations in a homogeneous phantom. It still has to be verified if this assertion also holds in realistic patient geometries, where the time-dependent variations in proton range modulate the interplay effect and complicate the definition of ITVs. For this purpose, we

initiated the development of an anthropomorphic respiratory phantom with a view to fulfil as many community requests to such a phantom as possible. The most recent prototype is very close to these requests, as presented in appendix A. This advanced 4D phantom could be turned into a commercial product in the near future.

In order to grow more confident in the results presented in this thesis, measurements with many more patient target volumes and on a wide variety of realistic motion trajectories are required. Ideally, these measurements will be conducted on our anthropomorphic phantom. The influence of multiple fields per fraction on the interplay effect should be studied as well, especially its interaction with re-scanning. Specifically, it would be of interest to find out how many fields correspond to how many re-scans. Such studies could in principle also be carried out with the CCD system. The major complication is the fact that in the current implementation, the system is only able to move horizontally. Therefore, the simple cuboid plexiglas stack would have to be replaced by a more complicated arrangement for beam irradiation from other directions than vertical.

The gating signal in our measurements was directly based on the true motion of the respiratory platform. In reality, gating signals are almost always based on an indirect measure of the tumour position. A more realistic evaluation of motion mitigation by gating is possible with a dynamic anthropomorphic phantom, where either the phantom surface or X-ray imaging of the diaphragm or implanted markers would be used as surrogates of tumour motion.

Apart from breath-hold, which in a way is very similar to gating, a prominent absence among the motion mitigation techniques tested here is tracking. One reason for this is the large effort of implementation and the open question of quality assurance. PET imaging during or right after treatment might solve the latter problem in the future. Tracking could be combined with re-scanning or gating. The first step in this direction would be slow tracking, whereby the baseline drift of tumour motion is corrected by the treatment table or the scanned beam. The offset could be determined by BEV imaging every 30 s, for example. With this approach, motion in the beam direction is both difficult to detect and difficult to correct. Motion detection based on BEV imaging has to rely on a correlation model, which might become inaccurate in the case of baseline drift anyway. Correction is performed by a shift in beam energy, which is only possible with a major overhaul of the control system of Gantry 2. At any rate, the relationship between motion in beam direction and changes in range is not at all straightforward. Depending on the circumstances, range changes are possible without motion along the beam and vice versa.

For our CCD system, quenching of the light output of the scintillating screen is a major obstacle for direct relation of the measured distributions to dose distributions, which clinically used plan evaluation criteria are based on. In principle, it is possible to conceive a scintillating material not exhibiting quenching, e.g., by carefully mixing two different scintillating powders, where the elevated light output of one of the powders for large stopping powers is compensating for the quenching of the other powder [278].

At some point, the two strands of 4D dose calculations at PSI will be merged. The first strand has been described in this work. Dose distributions in water are calculated

for arbitrary target volumes. Parallel computation of a large set of motion and re-scanning parameters is possible with relatively little effort by running the calculations on a computer cluster. The fact that computing time is linear in the number of re-scans is not a concern because the full parameter space can be cut into appropriate pieces with comparable computing time. The motivation for this strand has also been fostered by the fact that no TPS had been available for Gantry 2 for the better part of this thesis.

The second strand uses a modified, 4D version of the TPS for Gantry 1. While the beam model is the one of Gantry 1, the timing of treatment delivery is modelled on Gantry 2. The patient geometry is provided either by 4D-CT data sets or by 3D-CT images which are deformed in time according to the motion model derived from 4D-MRI data [287]. A certain automation of covering the parameter space of motion and re-scanning has been achieved, but improvements here are paramount to further progress. In a recent student project, the dose calculation has been ported to massively parallel computation on a graphics processing unit (GPU), yielding a speed-up of up to 100 times [290].

The merging of these two strands would combine dose calculation on full 4D patient data on a fast GPU with full automation of covering the parameter space. This could attain the shape of a fork of the Gantry 2 TPS, a stand-alone application or a plug-in to the TPS.

The benefits of continuous line scanning and the broad, uncovered area for research on this topic seems to be evident. Even so, quality assurance and on-line verification of the delivered dose has not been implemented yet. Improvements are also possible in the modulation of the dose rate. Two factors are worth mentioning here. First, the control loop, with a feed-forward part (the look-up table) and a feed-back part (the integral error), should be optimised. Second, the delay in adjusting the power supplies which generate the voltage of the deflector plate should be minimised. This would also help improve the performance of the control loop because the difference in MU rate due to this delay would sum up to a smaller integral error, hence oscillations and over-shoots in the MU rate would be subdued.

In section 3.2, we saw that the drawback of scaled re-scanning is the inefficiency of the approach when facing very small spot weights. This is not a purely academic problem, but so far, with re-scanning not being applied clinically, it has just not been a serious problem. While small spot weights can be suppressed in the plan optimisation procedure to some extent, for a large enough number of re-scans, a satisfactory trade-off between dose homogeneity and minimum spot weight is rendered difficult.

The method of mixed re-scanning, which was proposed in section 3.2, applied scaled re-scanning as long as the weights of the re-scanned spots are sufficiently large. As soon as these weights drop below a threshold, the algorithm switches to iso-layered re-scanning. The method works in terms of applicability on Gantry 2, but motion mitigation is worse than for both scaled and iso-layered re-scanning. More research into mixed re-scanning might resolve this issue.

For Gantry 2, increasing the overlap between neighbouring spots by increasing the beam size or by decreasing the spot grid spacing did not show clear benefits in a sim-

ulation study as part of a student project [291]. One reason is that the motion offset changes only slowly while applying a few rows of spots as long as the spots are not highly weighted. Thus, the particular distribution of the spots might have only a small influence on the interplay effect. More important are motion offsets between neighbouring spots that are located in different iso-energy layers. Decreasing the energy spacing should provide improved dose distributions, although the effect was only noticeable for layered re-scanning. In the best case, these methods of motion mitigation could be as effective as re-scanning. On the other hand, changing the beam size would go along with a considerable effort of machine calibration, and spot grids with small spacing would introduce much longer delivery times, which would grow quadratically with the scaling factor of the grid spacing.

In summary, we have demonstrated in this work that rescanning in combination with gating can be an effective method of mitigating organ motion in scanned proton therapy. The increase in treatment time can be countered by changing the scanning mode from discrete spot scanning to continuous line scanning. However, our conclusions have to be confirmed in more realistic phantoms, and over a larger range of target volumes and shapes, before these results can be generalised. Such work is currently being planned and performed using a dedicated 4D anthropomorphic phantom, the details of which are described in appendix A.

A. An anthropomorphic respiratory phantom

The major limitations of the measurements in this thesis were the restriction to a homogeneous phantom and one-dimensional motion. The ultimate goal in 4D dosimetry is a phantom that approaches as closely as possible the anatomical and physiological features of a human. The effect of density heterogeneities is especially important in proton therapy [292, 293, 78], including range changes of the proton beam and the degradation of the Bragg peaks.

The development of such an anthropomorphic phantom faces challenges in a way that compromises are unavoidable. Dose distributions should be measured with high precision and in three dimensions without disturbing the motion of the phantom and the dose distributions themselves. If the detector is taken out of the phantom for read-out, it should be possible to put it back at the exact same location and with the same orientation. In the case where the detector is permanently placed in the phantom, the data has to be transmitted out of the phantom without disturbing the motion and the dose distributions.

As part of this PhD project, and in close collaboration with colleagues in the 4D research group at PSI, a list of specifications has been worked out on the basis of community needs specific to charged particle therapy [294]. Several prototypes have been realised by the company *Centre Suisse d'Electronique et de Microtechnique* (CSEM) [295]. The current prototype is shown in figures A.1 and A.2.

The phantom consists of the abdominal part of an artificial skeleton, including the rib cage. The skeleton is mounted with non-metallic parts on a wooden board. Lungs made of foam are mounted in the rib cage so that they can be easily exchanged. The ribs provide mobile density heterogeneities. The space between the ribs is filled in with artificial muscular tissue. When the beam passes through a rib, its range is diminished compared with passing through muscular tissue. Besides a silicon heart, no other organs are modelled. Adding a liver is planned for a future prototype.

The skeleton is covered in a mould of artificial skin. This is vital to achieving a sufficiently large WER of the tumour. In addition, it facilitates surface imaging for set-up, gating and tracking. Both male and female skin moulds are available.

The Hounsfield units and densities of the materials by and large correspond to their human counterparts, except for lung tissue, which only has a density of $30\,\mathrm{kg}/m^3$. This is about 10 % of the value for human lung tissue. Research is ongoing into increasing the density of the phantom lung tissue, while retaining its flexibility and permeability with respect to air.

Three-dimensional motion is achieved by active inflation and deflation of the artificial

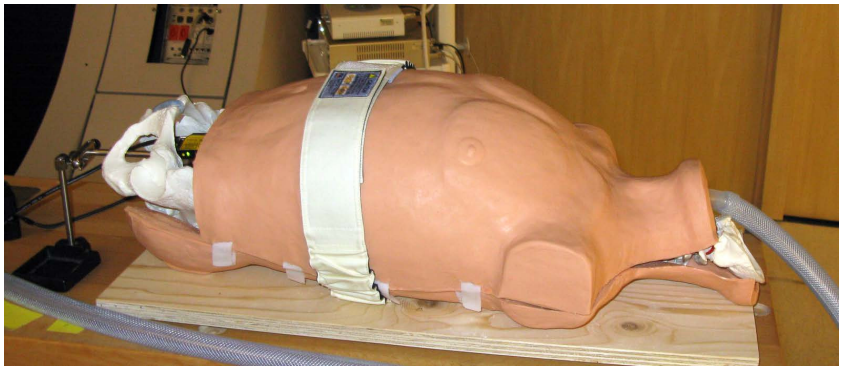

Figure A.1.: Anthropomorphic respiratory phantom. Motion is induced by inflation and deflation of the lung cavities by way of the pipe visible at the cranial end of the phantom. The actual extent of the motion is measured in the SI direction by an optical distance sensor. In the AP direction, this is achieved by placing a belt equipped with a pressure sensor around the abdomen.

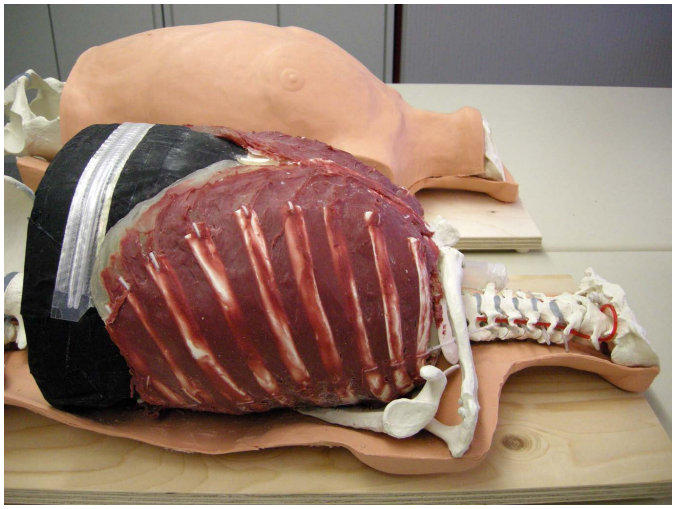

Figure A.2.: The top part of the skin mould has been removed for the phantom in front. The red muscular tissue filling the gaps between the ribs is visible as well as the black air-tight coating of the lungs. Tumours can be inserted by opening the air-tight zipper.

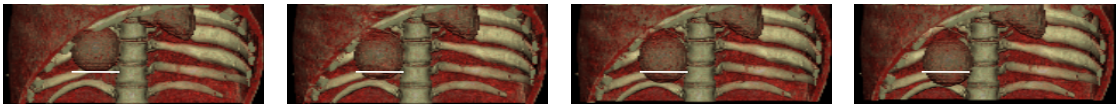

Figure A.3.: 4D-CT images showing the rib cage, the tumour and the heart in different phases of the breathing cycle. The sequence starts with the leftmost image at end-inhalation (0 %) and continues up to the rightmost image at end-exhalation (100 %). The white bar indicates the lower edge of the tumour in the end-inhalation phase.

lungs. Air pressure is taken as a surrogate of the motion amplitude. Motion along the three axes is necessarily correlated, as it is in humans. Arbitrary pressure curves, i.e., motion trajectories, can be applied. Air pressure is measured at the connection between phantom and regulated by a feed-back loop. However, the relation between pressure and three-dimensional motion is not straightforward. Figure A.3 shows 4D-CT images of the phantom in different phases of the breathing cycle.

The specifications of phantom motion are listed below. Amplitudes for the current prototype are not yet on the required level. Reproducibility can still be improved, especially after replacing the tumour or exchanging the lungs.

- amplitude of chest wall motion: $> 10\,\text{mm}$ in AP
- amplitude of tumour motion: $> 20\,\text{mm}$ in SI
- amplitude accuracy and reproducibility: $< 0.5\,\text{mm}$
- range of periods for regular motion: 1-15 s
- support of irregular, programmable motion patterns

The air ventilation and the electronics are well separated from the phantom, which contains no metallic parts. This renders the system CT and MRI compatible. For instance, deformable registration algorithms can be verified on an MRI. Such algorithms are important, for instance, for the calculation of 4D-CT data based on a single 3D-CT image and 4D-MRI imaging. Furthermore, these properties helps establish a correlation model between tumour and surface motion by 4D-MRI, as used in gating and tracking. For on-line tracking, our X-ray beam's eye view (BEV) can either track the diaphragm of the phantom or markers placed in or near the tumour. 3D motion can then be derived from the 2D images using a patient-specific model based on Principle Component Analysis of motion extracted from 4D-MRI data sets [296].

Dose distributions are captured by radio-chromic films inserted into slits of the silicon or wooden tumour and also into pockets in the breasts of the female skin. This approach is clearly not ideal in terms of reproducibility and efficiency because after each irradiation, the films have to be retrieved from the tumour, new films have to be inserted and

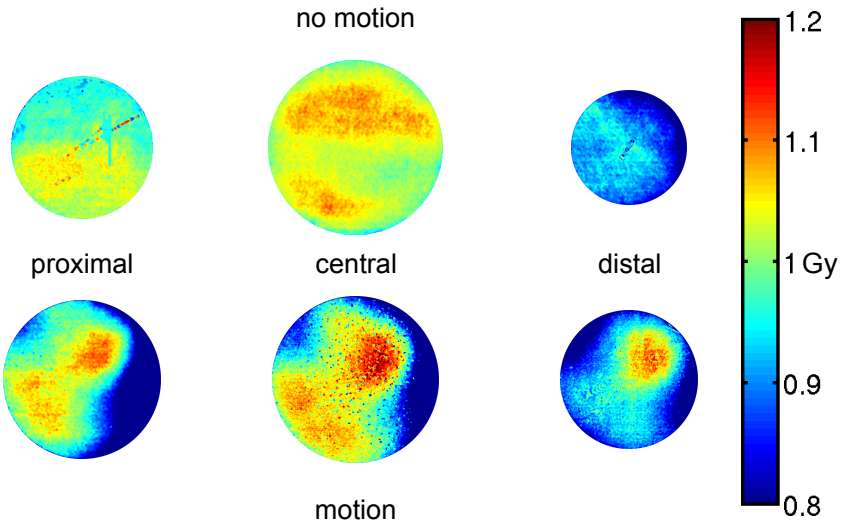

Figure A.4.: Interplay effect due to regular organ motion in the anthropomorphic respiratory phantom. Radiochromic films were inserted at three different positions inside the tumour, orthogonal to the incident beam. The motion amplitude was 1 cm in SI direction, corresponding to the horizontal axis on the plots, and the breathing period was 4 s.

	proximal	central	distal
static	1.00 ± 0.03	1.01 ± 0.03	1.00 ± 0.03
motion 1 cm	0.85 ± 0.13	0.89 ± 0.11	0.93 ± 0.06
motion 2 cm	0.84 ± 0.06	0.77 ± 0.06	0.68 ± 0.07

Table A.1.: Mean and standard deviation of the dose in Gy for the proximal, central and distal ROI for different motion scenarios. Because the ROIs for 2 cm motion amplitude extended into the ITV, the mean dose was lower than for 1 cm.

the tumour put back to its former position and orientation. Alternatively, point doses are measured by an ionisation chamber inserted into the tumour. Tumours of different shapes and sizes are available for placement into one of the lungs.

First measurements carried out on Gantry 1 clearly showed the interplay effect, as illustrated in figure A.4. Radio-chromic films were inserted into the tumour at three different depths. A single field with a prescribed dose of 1 Gy was applied and the beam axis was perpendicular to the films. The evaluation of the film measurements are summarised in table A.1.

In summary, the interplay effect in spot scanning due to organ motion has been demonstrated in an anthropomorphic, breathing phantom and research on Gantry 2 has started with this phantom with a view to verifying different motion mitigation techniques for scanned proton therapy.

Bibliography

[1] Particle Therapy Co-Operative Group, `http://ptcog.web.psi.ch`, last accessed: 4 November 2013.

[2] Engelsman M, Schwarz M and Dong L, *Physics Controversies in Proton Therapy*, Semin Radiat Oncol, 23(2):88, 2013.

[3] Flanz J and Bortfeld T, *Evolution of Technology to Optimize the Delivery of Proton Therapy: The Third Generation*, Semin Radiat Oncol, 23(2):142, 2013.

[4] Combs S E, Laperriere N and Brada M, *Clinical Controversies: Proton Radiation Therapy for Brain and Skull Base Tumors*, Semin Radiat Oncol, 23(2):120, 2013.

[5] Miralbell R, Cella L, Weber D and Lomax A, *Optimizing radiotherapy of orbital and paraorbital tumors: intensity-modulated X-ray beams vs. intensity-modulated proton beams*, Int J Rad Oncol Biol Phys, 47(4):1111, 2000.

[6] Fokas E, Kraft G, An H and Engenhart-Cabillic R, *Ion beam radiobiology and cancer: time to update ourselves*, Biochim Biophys Acta, 1796(2):216, 2009.

[7] Beringer J, Arguin J, Barnett R M, Copic K, Dahl O, Groom D E, Lin C et al., *Review of Particle Physics*, Phys Rev D, 86(1):010001, 2012.

[8] Bragg W H and Kleeman R, *LXXIV. On the ionization curves of radium*, Philos Mag, 8(48):726, 1904.

[9] Brown A and Suit H, *The centenary of the discovery of the Bragg peak*, Radiother Oncol, 73(3):265, 2004.

[10] Pedroni E, Scheib S, Böhringer T, Coray A, Grossmann M, Lin S and Lomax A, *Experimental characterization and physical modeling of the dose distribution of scanned proton pencil beams*, Phys Med Biol, 50(3):541, 2005.

[11] Bortfeld T and Schlegel W, *An analytical approximation of depth - dose distributions for therapeutic proton beams*, Phys Med Biol, 41(8):1331, 1996.

[12] Jette D and Chen W, *Creating a spread-out Bragg peak in proton beams*, Phys Med Biol, 56(11):N131, 2011.

[13] Zhang M, Westerly D C and Mackie T R, *Introducing an on-line adaptive procedure for prostate image guided intensity modulate proton therapy*, Phys Med Biol, 56(15):4947, 2011.

[14] Paganetti H and van Luijk P, *Biological Considerations When Comparing Proton Therapy With Photon Therapy*, Semin Radiat Oncol, 23(2):77, 2013.

[15] Biaggi M, Ballarini F, Burkard W, Egger E, Ferrari A and Ottolenghi A, *Physical and biophysical characteristics of a fully modulated 72 MeV therapeutic proton beam: model predictions and experimental data*, Nucl Instr Meth Phys A, 159:89, 1999.

[16] Carabe A, Moteabbed M, Depauw N, Schuemann J and Paganetti H, *Range uncertainty in proton therapy due to variable biological effectiveness*, Phys Med Biol, 57(5):1159, 2012.

[17] Scholz M, Kellerer A M, Kraft-Weyrather W and Kraft G, *Computation of cell survival in heavy ion beams for therapy*, Radiat Environ Biophys, 36(1):59, 1997.

[18] Goitein M, *Radiation Oncology: A Physicist's-Eye View*, New York: Springer, 2008.

[19] Kanai T, Kawachi K, Kumamoto Y, Ogawa H, Yamada T, Matsuzawa H and Inada T, *Spot scanning system for proton radiotherapy*, Med Phys, 7(4):365, 1980.

[20] Haberer T, Becher W, Schardt D and Kraft G, *Magnetic scanning system for heavy ion therapy*, Nucl Instr Meth Phys A, 330(1-2):296, 1993.

[21] Pedroni E, Bacher R, Blattman H, Böhringer T, Coray A, Lomax A, Lin S et al., *The 200-MeV proton therapy project at Paul Scherrer Institute Conceptual design and practical realization*, Med Phys, 22(1):37, 1995.

[22] Koehler A M, Schneider R J and Sisterson J M, *Flattening of proton dose distributions for large-field radiotherapy*, Med Phys, 4:297, 1977.

[23] Chu W T, Ludewigt B A and Renner T R, *Instrumentation for treatment of cancer using proton and light ion beams*, Rev Sci Instrum, 64(8):2055, 1993.

[24] Zenklusen S, *Exploring the potential of advanced pencil beam scanning for treating moving targets with the new Gantry 2 at PSI*, Ph.D. thesis, ETH Zürich, 2010.

[25] Kanai T, Kamematsu N, Minohara S, Komori M, Torikoshi M, Asakura N, Ikeda N et al., *Commissioning of conformal irradiation system for heavy-ion radiotherapy using a layer-stacking method*, Med Phys, 33:2989, 2006.

[26] Farr J B, Mascia A E, Hsi W, Allgower C E, Jesseph F, Schreuder A N, Wolanski M et al., *Clinical characterization of a proton beam continuous uniform scanning system with dose layer stacking*, Med Phys, 35(11):4945, 2008.

[27] Kanai T, Kawachi K, Matsuzawa H and Inada T, *Broad beam three-dimensional irradiation for proton radiotherapy*, Med Phys, 10(3):344, 1983.

[28] Torikoshi M, Minohara S, Kanematsu N, Komori M, Kanazawa M, Noda K, Miyahara N et al., *Irradiation System for HIMAC*, J Radiat Res, 48(Suppl.A):A15, 2007.

[29] Daartz J, Bangert M, Bussière M R and Engelsman H M M Kooy, *Characterization of a mini-multileaf collimator in a proton beamline*, Med Phys, 36(5):1886, 2009.

[30] Diffenderfer E S, Ainsley C G, Kirk M L, McDonough J E and Maughan R L, *Comparison of secondary neutron dose in proton therapy resulting from the use of a tungsten alloy MLC or a brass collimator system*, Med Phys, 38(11):6248, 2011.

[31] Moskvin V, Cheng C and Das I J, *Pitfalls of tungsten multileaf collimator in proton beam therapy*, Med Phys, 38(12):6395, 2011.

[32] Gottschalk B, *Multileaf collimators, air gap, lateral penumbra, and range compensation in proton radiotherapy*, Med Phys, 38(11):i, 2011.

[33] Bues M, Newhauser W D, Titt U and Smith A R, *Therapeutic step and shoot proton beam spot-scanning with a multi-leaf collimator: a Monte Carlo study*, Radiat Prot Dosim, 115(1-4):164, 2005.

[34] Furukawa T, Inaniwa T, Sato S, Shirai T, Takei Y, Takeshita E, Mizushima K et al., *Performance of the NIRS fast scanning system for heavy-ion radiotherapy*, Med Phys, 37(11):5672, 2010.

[35] Inaniwa T, Furukawa T, Tomitani T, Sato S, Noda K and Kanai T, *Optimization for fast-scanning irradiation in particle therapy*, Med Phys, 34(8):3302, 2007.

[36] Weber U, Becher W and Kraft G, *Depth scanning for a conformal ion beam treatment of deep seated tumours*, Phys Med Biol, 45(12):3627, 2000.

[37] Furukawa T, Inaniwa T, Sato S, Tomitani T, Minohara S, Noda K and Kanai T, *Design study of a raster scanning system for moving target irradiation in heavy-ion radiotherapy*, Med Phys, 34(3):1085, 2007.

[38] Noda K, Furukawa T, Fujimoto T, Inaniwa T, Iwata Y, Kanai T, Kanazawa M et al., *New treatment facility for heavy-ion cancer therapy at HIMAC*, Nucl Instr Meth Phys B, 266:2182, 2008.

[39] Haberer T, Debus J, Eickhoff H, Jäkel O, Schulz-Ertner D and Weber U, *The Heidelberg Ion Therapy Center*, Radiother Oncol, 73:S186, 2004.

[40] Combs S E, Jäkel O, Haberer T and Debus J, *Particle therapy at the Heidelberg Ion Therapy Center (HIT) Integrated research-driven university-hospital-based radiation oncology service in Heidelberg, Germany*, Radiother Oncol, 95(1):41, 2010.

[41] Orecchia R, Fossati P and Rossi S, *The national center for oncological hadron therapy: status of the project and future clinical use of the facility*, Tumori, 95(2):169, 2009.

[42] Giordanengo S, Donetti M, Marchetto F, Ansarinejad A, Attili A, Bourhaleb F, Burini F et al., *Performances of the scanning system for the CNAO center of oncological hadron therapy*, Nucl Instr Meth Phys A, 613(2):317, 2010.

[43] Bäumer C and Farr J B, *Lateral dose profile characterization in scanning particle therapy*, Med Phys, 38(6):2904, 2011.

[44] Zenklusen S M, Pedroni E, Meer D, Bula C and Safai S, *Preliminary investigations for the option to use fast uniform scanning with compensators on a gantry designed for IMPT*, Med Phys, 38(9):5208, 2011.

[45] Pedroni E, Meer D, Bula C, Safai S and Zenklusen S, *Pencil beam characteristics of the next-generation proton scanning gantry of PSI: design issues and initial commissioning results*, Eur Phys J Plus, 126(7):66, 2011.

[46] Schippers J M, Dölling R, Duppich J, Goitein G, Jermann M, Mezger A, Pedroni E et al., *The SC cyclotron and beam lines of PSIs new protontherapy facility PROSCAN*, Nucl Instr Meth Phys B, 261(1-2):773, 2007.

[47] Rietzel E and Bert C, *Respiratory motion management in particle therapy*, Med Phys, 37(2):449, 2010.

[48] Bert C and Durante M, *Motion in radiotherapy: particle therapy*, Phys Med Biol, 56(16):R113, 2011.

[49] Korreman S, Persson G, Nygaard D, Brink C and Juhler-Nøttrup T, *Respiration-correlated image guidance is the most important radiotherapy motion management strategy for most lung cancer patients*, Int J Rad Oncol Biol Phys, 83(4):1338, 2012.

[50] Brahme A, Nyman P and Skatt B, *4D laser camera for accurate patient positioning, collision avoidance, image fusion and adaptive approaches during diagnostic and therapeutic procedures*, Med Phys, 35(5):1670, 2008.

[51] Seppenwoolde Y, Shirato H, Kitamura K, Shimizu S, van Herk M, Lebesque J V and Miyasaka K, *Precise and real-time measurement of 3D tumor motion in lung due to breathing and heartbeat, measured during radiotherapy*, Int J Rad Oncol Biol Phys, 53(4):822, 2002.

[52] Langen K and Jones D, *Organ motion and its management*, Int J Rad Oncol Biol Phys, 50(1):265, 2001.

[53] Shirato H, Shimizu S, Kunieda T, Kitamura K, van Herk M, Kagei K, Nishioka T et al., *Physical aspects of a real-time tumor-tracking system for gated radiotherapy*, Int J Rad Oncol Biol Phys, 48(4):1187, 2000.

[54] Den R B, Doemer A, Kubicek G, Bednarz G, Galvin J M, Keane W M, Xiao Y et al., *Daily Image Guidance With Cone-Beam Computed Tomography for Head-and-Neck Cancer Intensity-Modulated Radiotherapy: A Prospective Study*, Int J Rad Oncol Biol Phys, 76(5):1353, 2010.

[55] Shirato H, Suzuki K, Sharp G C, Fujita K, Onimaru R, Fujino M, Kato N et al., *Speed and amplitude of lung tumor motion precisely detected in four-dimensional setup and in real-time tumor-tracking radiotherapy*, Int J Rad Oncol Biol Phys, 64(4):1229, 2006.

[56] Mori S, Endo M, Komatsu S, Yashiro T, Kandatsu S and Baba M, *Four-dimensional measurement of lung tumor displacement using 256-multi-slice CT-scanner*, Lung Cancer, 56(1):59, 2007.

[57] Britton K R, Starkschall G, Tucker S L, Pan T, Nelson C, Chang J Y, Cox J D et al., *Assessment of Gross Tumor Volume Regression and Motion Changes During Radiotherapy for Non-Small-Cell Lung Cancer as Measured by Four-Dimensional Computed Tomography*, Int J Rad Oncol Biol Phys, 68(4):1036, 2007.

[58] Suh Y, Dieterich S, Cho B and Keall P J, *An analysis of thoracic and abdominal tumour motion for stereotactic body radiotherapy patients*, Phys Med Biol, 53(13):3623, 2008.

[59] Sonke J, Lebesque J and van Herk M, *Variability of Four-Dimensional Computed Tomography Patient Models*, Int J Rad Oncol Biol Phys, 70(2):590, 2008.

[60] Quirk S, Becker N and Smith W L, *External respiratory motion analysis and statistics for patients and volunteers*, J Appl Clin Med Phys, 14(2):90, 2013.

[61] Price G J, Sharrock P J, Marchant T E, Parkhurst J M, Burton D, Jain P, Price P et al., *An analysis of breast motion using high-frequency, dense surface points captured by an optical sensor during radiotherapy treatment delivery*, Phys Med Biol, 54(21):6515, 2009.

[62] Wysocka B, Kassam Z, Lockwood G, Brierley J, Dawson L A, Buckley C A, Jaffray D et al., *Interfraction and respiratory organ motion during conformal radiotherapy in gastric cancer*, Int J Rad Oncol Biol Phys, 77(1):53, 2010.

[63] Patel A A, Wolfgang J A, Niemierko A, Hong T S, Yock T and Choi N C, *Implications of Respiratory Motion as Measured by Four-Dimensional Computed Tomography for Radiation Treatment Planning of Esophageal Cancer*, Int J Rad Oncol Biol Phys, 74(1):290, 2009.

[64] Eccles C L, Patel R, Simeonov A K, Lockwood G, Haider M and Dawson L A, *Comparison of Liver Tumor Motion With and Without Abdominal Compression Using Cine-Magnetic Resonance Imaging*, Int J Rad Oncol Biol Phys, 79(2):602, 2011.

[65] Kitamura K, Shirato H, Seppenwoolde Y, Shimizu T, Kodama Y, Endo H, Onimaru R et al., *Tumor location, cirrhosis, and surgical history contribute to tumor movement in the liver, as measured during stereotactic irradiation using a real-time tumor-tracking radiotherapy system*, Int J Rad Oncol Biol Phys, 56(1):221, 2003.

[66] Bussels B, Goethals L, Feron M, Bielen D, Dymarkowski S, Suetens P and Haustermans K, *Respiration-induced movement of the upper abdominal organs: a pitfall for the three-dimensional conformal radiation treatment of pancreatic cancer*, Radiother Oncol, 68(1):69, 2003.

[67] von Siebenthal M, *Analysis and Modelling of Respiratory Liver Motion using 4DMRI*, Ph.D. thesis, ETH Zürich, 2008.

[68] Feng M, Balter J M, Normolle D, Adusumilli S, Cao Y, Chenevert T L and Ben-Josef E, *Characterization of Pancreatic Tumor Motion Using Cine- MRI: Surrogates for Tumor Position Should be Used with Caution*, Int J Rad Oncol Biol Phys, 74(3):884, 2009.

[69] Kerkhof E M, van der Put R W, Raaymakers B W, van der Heide U A, Jürgenliemk-Schulz I M and Lagendijk J J W, *Intrafraction motion in patients with cervical cancer: The benefit of soft tissue registration using MRI*, Radiother Oncol, 93(1):115, 2009.

[70] Collen C, Engels B, Duchateau M, Tournel K, Ridder M D, Bral S, Verellen D et al., *Volumetric imaging by megavoltage computed tomography for assessment of internal organ motion during radiotherapy for cervical cancer*, Int J Rad Oncol Biol Phys, 77(5):1590, 2010.

[71] Beadle B M, Jhingran A, Salehpour M, Sam M, Iyer R B and Eifel P J, *Cervix Regression and Motion During the Course of External Beam Chemoradiation for Cervical Cancer*, Int J Rad Oncol Biol Phys, 73(1):235, 2009.

[72] Mah D, Freedman G, Milestone B, Hanlon A, Palacio E, Richardson T, Movsas B et al., *Measurement of intrafractional prostate motion using magnetic resonance imaging*, Int J Rad Oncol Biol Phys, 54(2):568, 2002.

[73] Langen K M, Willoughby T R, Meeks S L, Santhanam A, Cunningham A, Levine L and Kupelian P A, *Observations on Real-Time Prostate Gland Motion Using Electromagnetic Tracking*, Int J Rad Oncol Biol Phys, 71(4):1084, 2008.

[74] Adamson J and Wu Q, *Prostate Intrafraction Motion Assessed by Simultaneous Kilovoltage Fluoroscopy at Megavoltage Delivery I: Clinical Observations and Pattern Analysis*, Int J Rad Oncol Biol Phys, 78(5):1563, 2010.

[75] Webb S, *Motion effects in (intensity modulated) radiation therapy: a review*, Phys Med Biol, 51(13):R403, 2006.

[76] Lomax A J, *Intensity modulated proton therapy and its sensitivity to treatment uncertainties 1: the potential effects of calculational uncertainties*, Phys Med Biol, 53(4):1027, 2008.

[77] Lomax A J, *Intensity modulated proton therapy and its sensitivity to treatment uncertainties 2: the potential effects of inter-fraction and inter-field motions*, Phys Med Biol, 53(4):1043, 2008.

[78] Urie M, Goitein M, Holley W R and Chen G T, *Degradation of the Bragg peak due to inhomogeneities*, Phys Med Biol, 31(1):1, 1986.

[79] Phillips M H, Pedroni E, Blattman H, Böhringer T, Coray A and Scheib S, *Effects of respiratory motion on dose uniformity with a charged particle scanning method*, Phys Med Biol, 37(1):223, 1992.

[80] Gueulette J, Blattmann H, Pedroni E, Coray A, Coster B M D, Mahy P, Wambersie A et al., *Relative biologic effectiveness determination in mouse intestine for scanning proton beam at Paul Scherrer Institute, Switzerland. Influence of motion*, Int J Rad Oncol Biol Phys, 62(3):838, 2005.

[81] Yu C X, Jaffray D A and Wong J W, *The effects of intra-fraction organ motion on the delivery of dynamic intensity modulation*, Phys Med Biol, 43(1):91, 1998.

[82] Chui C, Yorke E and Hong L, *The effects of intra-fraction organ motion on the delivery of intensity-modulated field with a multileaf collimator*, Med Phys, 30(7):1736, 2003.

[83] Jiang S B, Pope C, Jarrah K M A, Kung J H, Bortfeld T and Chen G T Y, *An experimental investigation on intra-fractional organ motion effects in lung IMRT treatments*, Phys Med Biol, 48(12):1773, 2003.

[84] Seco J, Sharp G C, Turcotte J, Gierga D, Bortfeld T and Paganetti H, *Effects of organ motion on IMRT treatments with segments of few monitor units*, Med Phys, 34(3):923, 2007.

[85] Sterpin E, Janssens G, Orban de Xivry J, Goossens S, Wanet M, Lee J A, Delor A et al., *Helical tomotherapy for SIB and hypo-fractionated treatments in lung carcinomas: A 4D Monte Carlo treatment planning study*, Radiother Oncol, 104(2):173, 2012.

[86] Belec J and Clark B G, *Monte Carlo calculation of VMAT and helical tomotherapy dose distributions for lung stereotactic treatments with intra-fraction motion*, Phys Med Biol, 58(9):2807, 2013.

[87] Ong C L, Verbakel W F A R, Cuijpers J P, Slotman B J and Senan S, *Dosimetric Impact of Interplay Effect on RapidArc Lung Stereotactic Treatment Delivery*, Int J Rad Oncol Biol Phys, 79(1):305, 2011.

[88] Rao M, Wu J, Cao D, Wong T, Mehta V, Shepard D and Ye J, *Dosimetric Impact of Breathing Motion in Lung Stereotactic Body Radiotherapy Treatment Using Image-Modulated Radiotherapy and Volumetric Modulated Arc Therapy*, Int J Rad Oncol Biol Phys, 83(2):e251, 2012.

[89] Ong C L, Dahele M, Cuijpers J P, Senan S, Slotman B J and Verbakel W F A R, *Dosimetric Impact of Intrafraction Motion During RapidArc Stereotactic Vertebral Radiation Therapy Using Flattened and Flattening Filter-Free Beams*, Int J Rad Oncol Biol Phys, 86(3):420, 2013.

[90] Ong C L, Dahele M, Slotman B J and Verbakel W F A R, *Dosimetric Impact of the Interplay Effect During Stereotactic Lung Radiation Therapy Delivery Using Flattening Filter-Free Beams and Volumetric Modulated Arc Therapy*, Int J Rad Oncol Biol Phys, 86(4):743, 2013.

[91] Stambaugh C, Nelms B E, Dilling T, Stevens C, Latifi K, Zhang G, Moros E et al., *Experimentally studied dynamic dose interplay does not meaningfully affect target dose in VMAT SBRT lung treatments*, Med Phys, 40(9):091710, 2013.

[92] Bortfeld T, Jokivarsi K, Goitein M, Kung J and Jiang S B, *Effects of intra-fraction motion on IMRT dose delivery: statistical analysis and simulation*, Phys Med Biol, 47(13):2203, 2002.

[93] Rineker Proton Therapy Center, `http://www.rptc.de/de/infobereich/aktuelle-meldungen/erfahrungsberichte/news-detail/article/erfahrungsbericht-zweiter-monat-klinischer-betrieb-rptc-mai-09.html`, last accessed: 4 November 2013.

[94] Richter D, *Treatment planning for tumors with residual motion in scanned ion beam therapy*, Ph.D. thesis, TU Darmstadt, 2012.

[95] Lambert J, Suchowerska N, McKenzie D and Jackson M, *Intrafractional motion during proton beam scanning*, Phys Med Biol, 50(20):4853, 2005.

[96] Moyers M F, Miller D W, Bush D A and Slater J D, *Methodologies and tools for proton beam design for lung tumors*, Int J Rad Oncol Biol Phys, 49(5):1429, 2001.

[97] Albertini F, Hug E B and Lomax A J, *Is it necessary to plan with safety margins for actively scanned proton therapy?*, Phys Med Biol, 56(14):4399, 2011.

[98] Pflugfelder D, Wilkens J J and Oelfke U, *Worst case optimization: a method to account for uncertainties in the optimization of intensity modulated proton therapy*, Phys Med Biol, 53(6):1689, 2008.

[99] Unkelbach J, Bortfeld T, Martin B C and Soukup M, *Reducing the sensitivity of IMPT treatment plans to setup errors and range uncertainties via probabilistic treatment planning*, Med Phys, 36(1):149, 2009.

[100] Albertini F, Hug E B and Lomax A J, *The influence of the optimization starting conditions on the robustness of intensity-modulated proton therapy plans*, Phys Med Biol, 55(10):2863, 2010.

[101] Inaniwa T, Kanematsu N, Furukawa T and Hasegawa A, *A robust algorithm of intensity modulated proton therapy for critical tissue sparing and target coverage*, Phys Med Biol, 56(15):4749, 2011.

[102] Chen W, Unkelbach J, Trofimov A, Madden T, Kooy H, Bortfeld T and Craft D, *Including robustness in multi-criteria optimization for intensity-modulated proton therapy*, Phys Med Biol, 57(3):591, 2012.

[103] Casiraghi M, Albertini F and Lomax A J, *Advantages and limitations of the worst case scenario approach in IMPT treatment planning*, Phys Med Biol, 58(5):1323, 2013.

[104] Liu W, Frank S J, Li X, Li Y, Zhu R X and Mohan R, *PTV-based IMPT optimization incorporating planning risk volumes vs robust optimization*, Med Phys, 40(2):021709, 2013.

[105] Bert C, Grözinger S and Rietzel E, *Quantification of interplay effects of scanned particle beams and moving targets*, Phys Med Biol, 53(9):2253, 2008.

[106] Seco J, Robertson D, Trofimov A and Paganetti H, *Breathing interplay effects during proton beam scanning: simulation and statistical analysis*, Phys Med Biol, 54(14):N283, 2009.

[107] Grassberger C, Dowdell S, Lomax A, Sharp G, Shackleford J, Choi N, Willers H et al., *Motion Interplay as a Function of Patient Parameters and Spot Size in Spot Scanning Proton Therapy for Lung Cancer*, Int J Rad Oncol Biol Phys, 86(2):380, 2013.

[108] Paganetti H, Jiang H and Trofimov A, *4D Monte Carlo simulation of proton beam scanning: modelling of variations in time and space to study the interplay between scanning pattern and time-dependent patient geometry*, Phys Med Biol, 50(5):983, 2005.

[109] Mori S, Asakura H, Kandatsu S, Kumagai M, Baba M and Endo M, *Magnitude of Residual Internal Anatomy Motion on Heavy Charged Particle Dose Distribution in Respiratory Gated Lung Therapy*, Int J Rad Oncol Biol Phys, 71(2):587, 2008.

[110] Zenklusen S M, Pedroni E and Meer D, *A study on repainting strategies for treating moderately moving targets with proton pencil beam scanning at the new Gantry 2 at PSI*, Phys Med Biol, 55(17):5103, 2010.

[111] Dowdell S, Grassberger C, Sharp G C and Paganetti H, *Interplay effects in proton scanning for lung: a 4D Monte Carlo study assessing the impact of tumor and beam delivery parameters*, Phys Med Biol, 58(12):4137, 2013.

[112] Grözinger S, Rietzel E, Li Q, Bert C, Haberer T and Kraft G, *Simulations to design an online motion compensation system for scanned particle beams*, Phys Med Biol, 51(14):3517, 2006.

[113] Mori S, Furukawa T, Inaniwa T, Zenklusen S, Nakao M, Shirai T and Noda K, *Systematic evaluation of four-dimensional hybrid depth scanning for carbon-ion lung therapy*, Med Phys, 40(3):031720, 2013.

[114] Kraus K M, Heath E and Oelfke U, *Dosimetric consequences of tumour motion due to respiration for a scanned proton beam*, Phys Med Biol, 56(20):6563, 2011.

[115] Evans P M, Coolens C and Nioutsikou E, *Effects of averaging over motion and the resulting systematic errors in radiation therapy*, Phys Med Biol, 51(1):N1, 2006.

[116] Mori S, Wolfgang J, Lu H, Schneider R, Choi N C and Chen G T Y, *Quantitative Assessment of Range Fluctuations in Charged Particle Lung Irradiation*, Int J Rad Oncol Biol Phys, 70(1):253, 2008.

[117] Su Z, Lopatiuk-Tirpak O, Zeidan O, Sruprisan S I, Meeks S L, Slopsema R, Flampouri S et al., *An experimental investigation into the effect of periodic motion on proton dosimetry using polymer gel dosimeters and a programmable motion platform*, Phys Med Biol, 57(3):649, 2012.

[118] Bert C, Saito N, Schmidt A, Chaudhri N, Schardt D and Rietzel E, *Target motion tracking with a scanned particle beam*, Med Phys, 34(12):4768, 2007.

[119] Grözinger S, Rietzel E, Bert C, Haberer T and Kraft G, *Motion compensation with a scanned ion beam: a technical feasibility study*, Radiat Oncol, 3:31, 2008.

[120] Benedict S H, Yenice K M, Followill D, Galvin J M, Hinson W, Kavanagh B, Keall P et al., *Stereotactic body radiation therapy: the report of AAPM Task Group 101*, Med Phys, 37(8):4078, 2010.

[121] Engelsman M, Sharp G C, Bortfeld T, Onimaru R and Shirato H, *How much margin reduction is possible through gating or breath hold?*, Phys Med Biol, 50(3):477, 2005.

[122] *Prescribing, Recording an Reporting Photon Beam Therapy*, in *ICRU Report 50*, Bethesda, MD: ICRU, 1993.

[123] *Prescribing, Recording an Reporting Photon Beam Therapy (supplement to ICRU Report 50)*, in *ICRU Report 62*, Bethesda, MD: ICRU, 1999.

[124] Paganetti H, Jiang H, Adams J A, Chen G T and Rietzel E, *Monte Carlo simulations with time-dependent geometries to investigate effects of organ motion with high temporal resolution*, Int J Rad Oncol Biol Phys, 60(3):942, 2004.

[125] Rietzel E, Chen G T Y, Choi N C and Willet C G, *Four-dimensional image-based treatment planning: Target volume segmentation and dose calculation in the presence of respiratory motion*, Int J Rad Oncol Biol Phys, 61(5):1535, 2005.

[126] Dinkel J, Hintze C, Tetzlaff R, Huber P E, Herfarth K, Debus J, Kauczor H U et al., *4D-MRI analysis of lung tumor motion in patients with hemidiaphragmatic paralysis*, Radiother Oncol, 91(3):449, 2009.

[127] Jin J, Ajlouni M, Kong F S, Ryu S, Chetty I J and Movsas B, *Utilize target motion to cover clinical target volume (ctv) - a novel and practical treatment planning approach to manage respiratory motion*, Radiother Oncol, 89(3):292, 2009.

[128] Keall P, Kini V, Vedam S and Mohan R, *Motion adapted x-ray therapy: a feasibility study*, Phys Med Biol, 46:1, 2001.

[129] Ozhasoglu C and Murphy M J, *Issues in respiratory motion compensation during external-beam radiotherapy*, Int J Rad Oncol Biol Phys, 52(5):1389, 2002.

[130] Bert C, Gemmel A, Saito N and Rietzel E, *Gated irradiation with scanned particle beams*, Int J Rad Oncol Biol Phys, 73(4):1270, 2009.

[131] Vedam S S, Keall P J, Kini V R and Mohan R, *Determining parameters for respiration-gated radiotherapy*, Med Phys, 28(10):2139, 2001.

[132] Chang Z, Liu T, Cai J, Chen Q, Wang Z and Yin F, *Evaluation of integrated respiratory gating systems on a Novalis Tx system*, J Appl Clin Med Phys, 12(3):71, 2011.

[133] Xia J and Siochi R A, *A real-time respiratory motion monitoring system using KINECT: Proof of concept*, Med Phys, 39(5):2682, 2012.

[134] Peng Y, Vedam S, Gao S and Balter P, *A new respiratory monitoring and processing system based on Wii remote: Proof of principle*, Med Phys, 40(7):071712, 2013.

[135] Kanoulas E, Aslam J A, Sharp G C, Berbeco R I, Nishioka S, Shirato H and Jiang S B, *Derivation of the tumor position from external respiratory surrogates with periodical updating of the internal/external correlation*, Phys Med Biol, 52(17):5443, 2007.

[136] Wu H, Zhao Q, Berbeco R I, Nishioka S, Shirato H and Jiang S B, *Gating based on internal/external signals with dynamic correlation updates*, Phys Med Biol, 53(24):7137, 2008.

[137] Malinowski K, McAvoy T J, George R, Dieterich S and D'Souza W D, *Maintaining tumor targeting accuracy in real-time motion compensation systems for respiration-induced tumor motion*, Med Phys, 40(7):071709, 2013.

[138] Willoughby T R, Forbes A R, Buchholz D, Langen K M, Wagner T H, Zeidan O A, Kupelian P A et al., *Evaluation of an infrared camera and x-ray system using implanted fiducials in patients with lung tumors for gated radiation therapy*, Int J Rad Oncol Biol Phys, 66(2):568, 2006.

[139] Berbeco R I, Nishioka S, Shirato H, Chen G T Y and Jiang S B, *Residual motion of lung tumours in gated radiotherapy with external respiratory surrogates*, Phys Med Biol, 50(16):3655, 2005.

[140] Cui Y, Dy J G, Sharp G C, Alexander B and Jiang S B, *Multiple template-based fluoroscopic tracking of lung tumor mass without implanted fiducial markers*, Phys Med Biol, 52(20):6229, 2007.

[141] Li R, Lewis J H, no L I C and Jiang S B, *A feasibility study of markerless fluoroscopic gating for lung cancer radiotherapy using 4DCT templates*, Phys Med Biol, 54(20):N489, 2009.

[142] Cui Y, Dy J G, Alexander B and Jiang S B, *Fluoroscopic gating without implanted fiducial markers for lung cancer radiotherapy based on support vector machines*, Phys Med Biol, 53(16):N315, 2008.

[143] Moser T, Biederer J, Nill S, Remmert G and Bendl R, *Detection of respiratory motion in fluoroscopic images for adaptive radiotherapy*, Phys Med Biol, 53(12):3129, 2008.

[144] Xu Q, Hamilton R J, Schowengerdt R A, Alexander B and Jiang S B, *Lung tumor tracking in fluoroscopic video based on optical flow*, Med Phys, 35(12):5351, 2008.

[145] Lin T, no L I C, Tang X, Vasconcelos N and Jiang S B, *Fluoroscopic tumor tracking for image-guided lung cancer radiotherapy*, Phys Med Biol, 54(4):981, 2009.

[146] Lewis J H, Li R, Watkins W T, Lawson J D, Segars W P, no L I C, Song W Y et al., *Markerless lung tumor tracking and trajectory reconstruction using rotational cone-beam projections: a feasibility study*, Phys Med Biol, 55(9):2505, 2010.

[147] Fu D, Kahn R, Wang B, Wang H, Mu Z, Park J, Kuduvalli G et al., *Xsight Lung Tracking System: A Fiducial-Less Method for Respiratory Motion Tracking*, in H C U Jr, J J Kresl, J D Luketich, L Papiez, R D Timmerman and R A Schulz, editors, *Treating Tumors that Move with Respiration*, pages 265–282, Springer Berlin Heidelberg, 2007.

[148] Bibault J E, Prevost B, Dansin E, Mirabel X, Lacornerie T, Dubus F and Lartigau E, *Stereotactic radiotherapy for lung cancer: Non-invasive real-time tumor tracking*, Cancer Radiother, 14(8):690, 2010, PMID: 20674448.

[149] Bahig H, Campeau M, Vu T, Doucet R, Béliveau Nadeau D, Fortin B, Roberge D et al., *Predictive Parameters of CyberKnife Fiducial-less (XSight Lung) Applicability for Treatment of Early Non-Small Cell Lung Cancer: A Single-Center Experience*, Int J Rad Oncol Biol Phys.

[150] Yan H, Li H, Liu Z, Nath R and Liu W, *Hybrid MV-kV 3D respiratory motion tracking during radiation therapy with low imaging dose*, Phys Med Biol, 57(24):8455, 2012.

[151] Keall P J, Cattell H, Pokhrel D, Dieterich S, Wong K H, Murphy M J, Vedam S S et al., *Geometric accuracy of a real-time target tracking system with dynamic multileaf collimator tracking system*, Int J Rad Oncol Biol Phys, 56:1579, 2006.

[152] Lu H, Brett R, Sharp G, Safai S, Jiang S, Flanz J and Kooy H, *A respiratory-gated treatment system for proton therapy*, Med Phys, 34(8):3273, 2007.

[153] Korreman S S, Juhler-Nøttrup T and Boyer A L, *Respiratory gated beam delivery cannot facilitate margin reduction, unless combined with respiratory correlated image guidance*, Radiother Oncol, 86(1):61, 2008.

[154] Ono T, Takegawa H, Ageishi T, Takashina M, Numasaki H, Matsumoto M and Teshima T, *Respiratory monitoring with an acceleration sensor*, Phys Med Biol, 56(19):6279, 2011.

[155] Cherpak A J, Cygler J E, Andrusyk S, Pantarotto J, MacRae R and Perry G, *Clinical use of a novel in vivo 4D monitoring system for simultaneous patient motion and dose measurements*, Radiother Oncol, 102(2):290, 2012.

[156] Yan H, Yin F, Zhu G, Ajlouni M and Kim J H, *The correlation evaluation of a tumor tracking system using multiple external markers*, Med Phys, 33(11):4073, 2006.

[157] Chang K H, Ho M C, Yeh C C, Chen Y C, Lian F L, Lin W L, Yen J Y et al., *Effectiveness of external respiratory surrogates for in vivo liver motion estimation*, Med Phys, 39(8):5293, 2012.

[158] Killoran J H, Allen A M, Kann B H and Lyatskaya Y, *Inter fractional variability of breathing phase definition as determined by fiducial location*, Med Phys, 35(2):753, 2008.

[159] Fayad H, Pan T, Pradier O and Visvikis D, *Patient specific respiratory motion modeling using a 3D patient's external surface*, Med Phys, 39(6):3386, 2012.

[160] Hoisak J D P, Sixel K E, Tirona R, Cheung P C F and Pignol J, *Prediction of lung tumour position based on spirometry and on abdominal displacement: Accuracy and reproducibility*, Radiother Oncol, 78(3):339, 2006.

[161] McClelland J R, Hawkes D J, Schaeffter T and King A P, *Respiratory motion models: A review*, Med Image Anal, 17(1):19, 2013.

[162] Minohara S, Kanai T, Endo M, Noda K and Kanazawa M, *Respiratory gated irradiation system for heavy-ion radiotherapy*, Int J Rad Oncol Biol Phys, 47(4):1097, 2000.

[163] Chen Q, Weinhous M S, Deibel F C, Ciezki J P and Macklis R M, *Fluoroscopic study of tumor motion due to breathing: Facilitating precise radiation therapy for lung cancer patients*, Med Phys, 28(9):1850, 2001.

[164] Hoisak J D P, Sixel K E, Tirona R, Cheung P C F and Pignol J P, *Correlation of lung tumor motion with external surrogate indicators of respiration*, Int J Rad Oncol Biol Phys, 60(4):1298, 2004, PMID: 15519803.

[165] Chi P C M, Balter P, Luo D, Mohan R and Pan T, *Relation of external surface to internal tumor motion studied with cine CT*, Med Phys, 33(9):3116, 2006.

[166] Redmond K J, Song D Y, Fox J L, Zhou J, Rosenzweig C N and Ford E, *Respiratory Motion Changes of Lung Tumors Over the Course of Radiation Therapy Based on Respiration-Correlated Four-Dimensional Computed Tomography Scans*, Int J Rad Oncol Biol Phys, 75(5):1605, 2009.

[167] Vedam S S, Kini V R, Keall P J, Ramakrishnan V, Mostafavi H and Mohan R, *Quantifying the predictability of diaphragm motion during respiration with a noninvasive external marker*, Med Phys, 30(4):505, 2003.

[168] Nishioka S, Nishioka T, Kawahara M, Tanaka S, Hiromura T, Tomita K and Shirato H, *Exhale fluctuation in respiratory-gated radiotherapy of the lung: A pitfall of respiratory gating shown in a synchronized internal/external marker recording study*, Radiother Oncol, 86(1):69, 2008.

[169] Gierga D P, Brewer J, Sharp G C, Betke M, Willett C G and Chen G T Y, *The correlation between internal and external markers for abdominal tumors: Implications for respiratory gating*, Int J Rad Oncol Biol Phys, 61(5):1551, 2005.

[170] Koch N, Liu H H, Starkschall G, Jacobson M, Forster K, Liao Z, Komaki R et al., *Evaluation of internal lung motion for respiratory-gated radiotherapy using MRI: Part I - correlating internal lung motion with skin fiducial motion*, Int J Rad Oncol Biol Phys, 60(5):1459, 2004.

[171] von Siebenthal M, Szekely G, Lomax A J and Cattin P C, *Systematic errors in respiratory gating due to intrafraction deformations of the liver*, Med Phys, 34(9):3620, 2007.

[172] Ohara K, Okumura T, Akisada M, Inada T, Mori T, Yokota H and Calaguas M J B, *Irradiation synchronized with respiration gate*, Int J Rad Oncol Biol Phys, 17(4):853, 1989.

[173] Otani Y, Fukuda I, Tsukamoto N, Kumazaki Y, Sekine H, Imabayashi E, Kawaguchi O et al., *A comparison of the respiratory signals acquired by different respiratory monitoring systems used in respiratory gated radiotherapy*, Med Phys, 37(12):6178, 2010.

[174] Bert C, Metheany K G, Doppke K and Chen G T Y, *A phantom evaluation of a stereo-vision surface imaging system for radiotherapy patient setup*, Med Phys, 32(9):2753, 2005.

[175] Hughes S, McClelland J, Tarte S, Lawrence D, Ahmad S, Hawkes D and Landau D, *Assessment of two novel ventilatory surrogates for use in the delivery of gated/tracked radiotherapy for non-small cell lung cancer*, Radiother Oncol, 91(3):336, 2009.

[176] Kauweloa K I, Ruan D, Park J C, Sandhu A, Kim G Y, Pawlicki T, Watkins W T et al., *GateCT surface tracking system for respiratory signal reconstruction in 4DCT imaging*, Med Phys, 39(1):492, 2012.

[177] Schaller C, Penne J and Hornegger J, *Time-of-flight sensor for respiratory motion gating*, Med Phys, 35(7):3090, 2008.

[178] Placht S, Stancanello J, Schaller C, Balda M and Angelopoulou E, *Fast time-of-flight camera based surface registration for radiotherapy patient positioning*, Med Phys, 39(1):4, 2012.

[179] Kubo H D and Hill B C, *Respiration gated radiotherapy treatment: a technical study*, Phys Med Biol, 41(1):83, 1996.

[180] Zhang T, Keller H, O'Brien M J, Mackie T R and Paliwal B, *Application of the spirometer in respiratory gated radiotherapy*, Med Phys, 30(12):3165, 2003.

[181] Ha J K, Perlow D B, Yi B Y and Yu C X, *On the sources of drift in a turbine-based spirometer*, Phys Med Biol, 53(16):4269, 2008.

[182] Werner R, White B, Handels H, Lu W and Low D A, *Technical Note: Development of a tidal volume surrogate that replaces spirometry for physiological breathing monitoring in 4D CT*, Med Phys, 37(2):615, 2010.

[183] Lu W, Low D A, Parikh P J, Nystrom M M, El Naqa I M, Wahab S H, Handoko M et al., *Comparison of spirometry and abdominal height as four-dimensional computed tomography metrics in lung*, Med Phys, 32(7):2351, 2005.

[184] Didierlaurent D, Ribes S, Caselles O, Jaudet C, Cazalet J, Batatia H and Courbon F, *A new respiratory gating device to improve 4D PET/CT*, Med Phys, 40(3):032501, 2013.

[185] Smith A, Gillin M, Bues M, Zhu X R, Suzuki K, Mohan R, Woo S et al., *The M. D. Anderson proton therapy system*, Med Phys, 36(9):4068, 2009.

[186] Kang J H, Wilkens J J and Oelfke U, *Demonstration of scan path optimization in proton therapy*, Med Phys, 34(9):3457, 2007.

[187] Pardo J, Donetti M, Bourhaleb F, Ansarinejad A, Attili A, Cirio R, Garella M A et al., *Heuristic optimization of the scanning path of particle therapy beams*, Med Phys, 36(6):2043, 2009.

[188] Furukawa T, Inaniwa T, Sato S, Shirai T, Mori S, Takeshita E, Mizushima K et al., *Moving target irradiation with fast rescanning and gating in particle therapy*, Med Phys, 37(9):4874, 2010.

[189] Engelsman M, Rietzel E and Kooy H M, *Four-dimensional proton treatment planning for lung tumors*, Int J Rad Oncol Biol Phys, 64(5):1589, 2006.

[190] Bert C and Rietzel E, *4D treatment planning for scanned ion beams*, Radiat Oncol, 2(1):24, 2007.

[191] Knopf A, Boye D, Lomax A and Mori S, *Adequate margin definition for scanned particle therapy in the incidence of intrafractional motion*, Phys Med Biol, 58(17):6079, 2013.

[192] Bert C, *Bestrahlungsplanung für bewegte Zielvolumina in der Tumortherapie mit gescanntem Kohlenstoffstrahl*, Ph.D. thesis, TU Darmstadt, 2006.

[193] Knopf A, Hong T S and Lomax A, *Scanned proton radiotherapy for mobile targets – the effectiveness of re-scanning in the context of different treatment planning approaches and for different motion characteristics*, Phys Med Biol, 56(22):7257, 2011.

[194] Smith E M, Smoak W M and MiBelli T, *Use of physiological triggers for dynamic and static Anger camera studies*, J Nucl Med, 10:436, 1969.

[195] DeLand F H and Mauderli W, *Gating Mechanism for Motion-Free Liver and Lung Scintigraphy*, J Nucl Med, 13(12):939, 1972, PMID: 5087167.

[196] Wong J W, Sharpe M B, Jaffray D A, Kini V R, Robertson J M, Stromberg J S and Martinez A A, *The use of active breathing control (ABC) to reduce margin for breathing motion*, Int J Rad Oncol Biol Phys, 44(4):911, 1999.

[197] Oshiro Y, Okumura T, Ishida M, Sugahara S, Mizumoto M, Hashimoto T, Yasuoka K et al., *Displacement of hepatic tumor at time to exposure in end-expiratory-triggered-pulse proton therapy*, Radiother Oncol, 99(2):124, 2011.

[198] Dietrich L, Tücking T, Nill S and Oelfke U, *Compensation for respiratory motion by gated radiotherapy: an experimental study*, Phys Med Biol, 50(10):2405, 2005.

[199] Butler L E, Forster K M, Stevens C W, Bloch C, Liu H H, Tucker S L, Komaki R et al., *Dosimetric benefits of respiratory gating: a preliminary study*, J Appl Clin Med Phys, 5(1):16, 2004.

[200] Hanley J, Debois M M, Mah D, Mageras G S, Raben A, Rosenzweig K, Mychalczak B et al., *Deep inspiration breath-hold technique for lung tumors: The potential value of target immobilization and reduced lung density in dose escalation*, Int J Rad Oncol Biol Phys, 45:603, 1999.

[201] Mihaylov I B, Fatyga M, Moros E G, Penagaricano J and Lerma F A, *Lung Dose for Minimally Moving Thoracic Lesions Treated With Respiration Gating*, Int J Rad Oncol Biol Phys, 77(1):285, 2010.

[202] Aristophanous M, Rottmann J, Park S, Nishioka S, Shirato H and Berbeco R I, *Image-guided adaptive gating of lung cancer radiotherapy: a computer simulation study*, Phys Med Biol, 55(15):4321, 2010.

[203] Fuji H, Asada Y, Numano M, Yamashita H, Nishimura T, Hashimoto T, Harada H et al., *Residual Motion and Duty Time in Respiratory Gating Radiotherapy Using Individualized or Population-Based Windows*, Int J Rad Oncol Biol Phys, 75(2):564, 2009.

[204] Minohara S, Endo M, Kanai T, Kato H and Tsujii H, *Estimating uncertainties of the geometrical range of particle radiotherapy during respiration*, Int J Rad Oncol Biol Phys, 56(1):121, 2003.

[205] Berbeco R I, Mostafavi H, Sharp G C and Jiang S B, *Towards fluoroscopic respiratory gating for lung tumours without radiopaque markers*, Phys Med Biol, 50(19):4481, 2005.

[206] Nelson C, Starkschall G, Balter P, Morice R C, Stevens C W and Chang J Y, *Assessment of lung tumor motion and setup uncertainties using implanted fiducials*, Int J Rad Oncol Biol Phys, 67(3):915, 2007.

[207] Mori S, Yanagi T, Hara R, Sharp G C, Asakura H, Kumagai M, Kishimoto R et al., *Comparison of Respiratory-Gated and Respiratory-Ungated Planning in Scattered Carbon Ion Beam Treatment of the Pancreas Using Four-Dimensional Computed Tomography*, Int J Rad Oncol Biol Phys, 76(1):303, 2010.

[208] Mageras G S and Yorke E, *Deep inspiration breath hold and respiratory gating strategies for reducing organ motion in radiation treatment*, Semin Radiat Oncol, 14(1):65, 2004.

[209] Nelson C, Starkschall G, Balter P, Fitzpatrick M J, Antolak J A, Tolani N and Prado K, *Respiration-correlated treatment delivery using feedback-guided breath hold: A technical study*, Med Phys, 32(1):175, 2005.

[210] Linthout N, Bral S, de Vondel I V, Verellen D, Tournel K, Gevaert T, Duchateau M et al., *Treatment delivery time optimization of respiratory gated radiation therapy by application of audio-visual feedback*, Radiother Oncol, 91(3):330, 2009.

[211] Dawson L A, Brock K K, Kazanjian S, Fitch D, McGinn C J, Lawrence T S, Ten Haken R K et al., *The reproducibility of organ position using active breathing control (ABC) during liver radiotherapy*, Int J Rad Oncol Biol Phys, 51(5):1410, 2001.

[212] Balter J M, Brock K K, Litzenberg D W, McShan D L, Lawrence T S, Haken R T, McGinn C J et al., *Daily targeting of intrahepatic tumors for radiotherapy*, Int J Rad Oncol Biol Phys, 52(1):266, 2002.

[213] Remouchamps V M, Letts N, Vicini F A, Sharpe M B, Kestin L L, Chen P Y, Martinez A A et al., *Initial clinical experience with moderate deep-inspiration breath hold using an active breathing control device in the treatment of patients with left-sided breast cancer using external beam radiation therapy*, Int J Radiat Oncol Biol Phys, 56(3):704, 2003.

[214] Pedersen A N, Korreman S, Nystrom H and Specht L, *Breathing adapted radiotherapy of breast cancer: reduction of cardiac and pulmonary doses using voluntary inspiration breath-hold*, Radiother Oncol, 72(1):53, 2004.

[215] Koshani R, Balter J M, Hayman J A, Henning G T and van Herk M, *Short-term and long-term reproducibility of lung tumor position using active breathing control (ABC)*, Int J Rad Oncol Biol Phys, 65(5):1553, 2006.

[216] McNair H A, Brock J, Symonds-Tayler J R N, Ashley S, Eagle S, Evans P M, Kavanagh A et al., *Feasibility of the use of the Active Breathing Co ordinator(TM) (ABC) in patients receiving radical radiotherapy for non-small cell lung cancer (NSCLC)*, Radiother Oncol, 93(3):424, 2009.

[217] Wong V Y W, Tung S Y, Ng A W Y, Li F A S and Leung J O Y, *Real-time monitoring and control on deep inspiration breath-hold for lung cancer radiotherapy—Combination of ABC and external marker tracking*, Med Phys, 37(9):4673, 2010.

[218] Peng Y, Vedam S, Chang J Y, Gao S, Sadagopan R, Bues M and Balter P, *Implementation of Feedback-Guided Voluntary Breath-Hold Gating for Cone Beam CT-Based Stereotactic Body Radiotherapy*, Int J Rad Oncol Biol Phys, 80(3):909, 2011.

[219] Hu W, Xu A, Li G, Zhang Z, Housley D and Ye J, *A real-time respiration position based passive breath gating equipment for gated radiotherapy: A preclinical evaluation*, Med Phys, 39(3):1345, 2012.

[220] Zhong R, Wang J, Jiang X, He Y, Zhang H, Chen N, Bai S et al., *Hypofraction radiotherapy of liver tumor using cone beam computed tomography guidance combined with active breath control by long breath-holding*, Radiother Oncol, 104(3):379, 2012.

[221] Eccles C, Brock K K, Bissonnette J, Hawkins M and Dawson L A, *Reproducibility of liver position using active breathing coordinator for liver cancer radiotherapy*, Int J Rad Oncol Biol Phys, 64(3):751, 2006.

[222] Stock M, Kontrisova K, Dieckmann K, Bogner J, Poetter R and Georg D, *Development and application of a real-time monitoring and feedback system for deep inspiration breath hold based on external marker tracking*, Med Phys, 33(8):2868, 2006.

[223] Glide-Hurst C K, Gopan E and Hugo G D, *Anatomic and Pathologic Variability During Radiotherapy for a Hybrid Active Breath-Hold Gating Technique*, Int J Rad Oncol Biol Phys, 77(3):910, 2010.

[224] Starkschall G, Balter P, Britton K, McAleer M F, Cox J D and Mohan R, *Interfractional Reproducibility of Lung Tumor Location Using Various Methods of Respiratory Motion Mitigation*, Int J Rad Oncol Biol Phys, 79(2):596, 2010.

[225] Nakamura M, Shibuya K, Shiinoki T, Matsuo Y, Nakamura A, Nakata M, Sawada A et al., *Positional Reproducibility of Pancreatic Tumors Under End-Exhalation Breath-Hold Conditions Using a Visual Feedback Technique*, Int J Rad Oncol Biol Phys, 79(5):1565, 2011.

[226] Wang X, Zhong R, Bai S, Xu Q, Zhao Y, Wang J, Jiang X et al., *Lung tumor reproducibility with active breath control (ABC) in image-guided radiotherapy based on cone-beam computed tomography with two registration methods*, Radiother Oncol, 99(2):148, 2011.

[227] Keall P, Mageras G, Balter J, Emery R, Forster K, Jiang S, Kapatoes J et al., *The management of respiratory motion in radiation oncology report of AAPM Task Group 76*, Med Phys, 33(10):3874, 2006.

[228] Marks L B, Bentzen S M, Deasy J O, Kong F, Bradley J D, Vogelius I S, El Naqa I et al., *Radiation Dose-Volume Effects in the Lung*, Int J Rad Oncol Biol Phys, 76(3, Supplement):S70, 2010.

[229] Korreman S S, Pedersen A N, Jakobi Nøttrup T, Specht L and Nystrøm H, *Breathing adapted radiotherapy for breast cancer: Comparison of free breathing gating with the breath-hold technique*, Radiother Oncol, 76(3):311, 2005.

[230] Nakamura K, Shioyama Y, Nomoto S, Ohga S, Toba T, Yoshitake T, Anai S et al., *Reproducibility of The Abdominal and Chest Wall Position by Voluntary Breath-Hold Technique Using a Laser-Based Monitoring and Visual Feedback System*, Int J Rad Oncol Biol Phys, 68(1):267, 2007.

[231] Berson A M, Emery R, Rodriguez L, Richards G M, Ng T, Sanghavi S and Barsa J, *Clinical experience using respiratory gated radiation therapy: Comparison of free-breathing and breath-hold techniques*, Int J Rad Oncol Biol Phys, 60(2):419, 2004.

[232] Hunjan S, Starkschall G, Prado K, Dong L and Balter P, *Lack of Correlation Between External Fiducial Positions and Internal Tumor Positions During Breath-Hold CT*, Int J Rad Oncol Biol Phys, 76(5):1586, 2010.

[233] Cerviño L, Gupta S, Rose M A, Yashar C and Jiang S B, *Using surface imaging and visual coaching to improve the reproducibility and stability of deep-inspiration breath hold for left-breast-cancer radiotherapy*, Phys Med Biol, 54(22):6853, 2009.

[234] Alderliesten T, Sonke J, Betgen A, Honnef J, van Vliet-Vroegindeweij C and Remeijer P, *Accuracy Evaluation of a 3-Dimensional Surface Imaging System for Guidance in Deep-Inspiration Breath-Hold Radiation Therapy*, Int J Rad Oncol Biol Phys, 85(2):536, 2013.

[235] Betgen A, Alderliesten T, Sonke J J, van Vliet-Vroegindeweij C, Bartelink H and Remeijer P, *Assessment of set-up variability during deep inspiration breath hold radiotherapy for breast cancer patients by 3D-surface imaging*, Radiother Oncol, 106(2):225, 2013.

[236] Rosenzweig K E, Hanley J, Mah D, Mageras G, Hunt M, Toner S, Burman C et al., *The deep inspiration breath-hold technique in the treatment of inoperable non-small-cell lung cancer*, Int J Rad Oncol Biol Phys, 48:81, 2000.

[237] Murphy M J, *The accuracy of dose localization for an image-guided frameless radiosurgery system*, Med Phys, 23(12):2043, 1996.

[238] Krauss A, Nill S and Oelfke U, *The comparative performance of four respiratory motion predictors for real-time tumour tracking*, Phys Med Biol, 56(16):5303, 2011.

[239] Seregni M, Cerveri P, Riboldi M, Pella A and Baroni G, *Robustness of external/internal correlation models for real-time tumor tracking to breathing motion variations*, Phys Med Biol, 57(21):7053, 2012.

[240] Ernst F, Dürichen R, Schlaefer A and Schweikard A, *Evaluating and comparing algorithms for respiratory motion prediction*, Phys Med Biol, 58(11):3911, 2013.

[241] Pollock S, Lee D, Keall P and Kim T, *Audiovisual biofeedback improves motion prediction accuracy*, Med Phys, 40(4):041705, 2013.

[242] D'Souza W D and McAvoy T J, *An analysis of the treatment couch and control system dynamics for respiration-induced motion compensation*, Med Phys, 33(12):4701, 2006.

[243] Qiu P, D'Souza W, McAvoy T and Liu K, *Inferential modeling and predictive feedback control in real-time motion compensation using the treatment couch during radiotherapy*, Phys Med Biol, 52:5831, 2007.

[244] Wilbert J, Meyer J, Baier K, Guckenberger M, Herrmann C, Heß R, Janka C et al., *Tumor tracking and motion compensation with an adaptive tumor tracking system (ATTS): System description and prototype testing*, Med Phys, 35(9):3911, 2008.

[245] Hoogeman M, Prévost J, Nuyttens J, Pöll J, Levendag P and Heijmen B, *Clinical Accuracy of the Respiratory Tumor Tracking System of the CyberKnife: Assessment by Analysis of Log Files*, Int J Rad Oncol Biol Phys, 74(1):297, 2009.

[246] Saito N, Bert C, Chaudhri N, Gemmel A, Schardt D, Durante M and Rietzel E, *Speed and accuracy of a beam tracking system for treatment of moving targets with scanned ion beams*, Phys Med Biol, 54(16):4849, 2009.

[247] Buzurovic I, Huang K, Yu Y and Podder T K, *A robotic approach to 4D real-time tumor tracking for radiotherapy*, Phys Med Biol, 56(5):1299, 2011.

[248] Buzurovic I, Yu Y, Werner-Wasik M, Biswas T, Anne P R, Dicker A P and Podder T K, *Implementation and experimental results of 4D tumor tracking using robotic couch*, Med Phys, 39(11):6957, 2012.

[249] Haas O C L, Skworcow P, Paluszczyszyn D, Sahih A, Ruta M and Mills J A, *Couch-based motion compensation: modelling, simulation and real-time experiments*, Phys Med Biol, 57(18):5787, 2012.

[250] Lee S, Chang K H, Shim J B, Cao Y, Lee C K, Cho S J, Yang D S et al., *Evaluation of mechanical accuracy for couch-based tracking system (CBTS)*, J Appl Clin Med Phys, 13(6):157, 2012.

[251] Menten M J, Guckenberger M, Herrmann C, Krauss A, Nill S, Oelfke U and Wilbert J, *Comparison of a multileaf collimator tracking system and a robotic treatment couch tracking system for organ motion compensation during radiotherapy*, Med Phys, 39(11):7032, 2012.

[252] Seregni M, Kaderka R, Fattori G, Riboldi M, Pella A, Constantinescu A, Saito N et al., *Tumor tracking based on correlation models in scanned ion beam therapy: an experimental study*, Phys Med Biol, 58(13):4659, 2013.

[253] Wilbert J, Baier K, Hermann C, Flentje M and Guckenberger M, *Accuracy of Real-time Couch Tracking During 3-dimensional Conformal Radiation Therapy, Intensity Modulated Radiation Therapy, and Volumetric Modulated Arc Therapy for Prostate Cancer*, Int J Rad Oncol Biol Phys, 85(1):237, 2013.

[254] Knopf A and Lomax A, *In vivo proton range verification: a review*, Physics in Medicine and Biology, 58(15):R131, 2013.

[255] Li Q, Grözinger S, Haberer T, Rietzel E and Kraft G, *Online compensation for target motion with scanned particle beams: simulation environment*, Phys Med Biol, 49:3029, 2004.

[256] Bert C, Gemmel A, Saito N, Chaudhri N, Schardt D, Durante M, Kraft G et al., *Dosimetric precision of an ion beam tracking system*, Radiother Oncol, 5(1):61, 2010, PMID: 20591160.

[257] van de Water S, Kreuger R, Zenklusen S M, Hug E and Lomax A J, *Tumour tracking with scanned proton beams: assessing the accuracy and practicalities*, Phys Med Biol, 54:6549, 2009.

[258] Lüchtenborg R, Saito N, Durante M and Bert C, *Experimental verification of a real-time compensation functionality for dose changes due to target motion in scanned particle therapy*, Med Phys, 38(10):5448, 2011.

[259] Steidl P, Richter D, Schuy C, Schubert E, Haberer T, Durante M and Bert C, *A breathing thorax phantom with independently programmable 6D tumour motion for dosimetric measurements in radiation therapy*, Phys Med Biol, 57(8):2235, 2012.

[260] Wilbert J, Baier K, Richter A, Herrmann C, Ma L, Flentje M and Guckenberger M, *Influence of Continuous Table Motion on Patient Breathing Patterns*, Int J Rad Oncol Biol Phys, 77(2):622, 2010.

[261] Sweeney R A, Arnold W, Steixner E, Nevinny-Stickel M and Lukas P, *Compensating for Tumor Motion by a 6-Degree-of-Freedom Treatment Couch: Is Patient Tolerance an Issue?*, Int J Radiat Oncol Biol Phys, 74(1):168, 2009.

[262] D'Souza W D, Naqvi S A and Yu C X, *Real-time intra-fraction-motion tracking using the treatment couch: a feasibility study*, Phys Med Biol, 50(17):4021, 2005.

[263] McNamara J E, Regmi R, Michael Lovelock D, Yorke E D, Goodman K A, Rimner A, Mostafavi H et al., *Toward correcting drift in target position during radiotherapy via computer-controlled couch adjustments on a programmable Linac*, Med Phys, 40(5):051719, 2013.

[264] Krämer M and Scholz M, *Treatment planning for heavy-ion radiotherapy: calculation and optimization of biologically effective dose*, Phys Med Biol, 45(11):3319, 2000.

[265] Kang J H, Wilkens J J and Oelfke U, *Non-uniform depth scanning for proton therapy systems employing active energy variation*, Phys Med Biol, 53(9):N149, 2008.

[266] ICRU, *Prescribing, recording, and reporting Proton-Beam therapy (ICRU report 78)*, J ICRU, 7, 2007.

[267] Trofimov A and Bortfeld T, *Beam delivery sequencing for intensity modulated proton therapy*, Phys Med Biol, 48(10):1321, 2003.

[268] Safai S, *Developement of a dosimetric phantom*, Ph.D. thesis, ETH Zürich, 2005.

[269] Zhang R, Taddei P J, Fitzek M M and Newhauser W D, *Water equivalent thickness values of materials used in beams of protons, helium, carbon and iron ions*, Phys Med Biol, 55(9):2481, 2010.

[270] Gomà C, Andreo P and Sempau J, *Spencer–Attix water/medium stopping-power ratios for the dosimetry of proton pencil beams*, Phys Med Biol, 58(8):2509, 2013.

[271] Lomax A, *Intensity modulated methods for proton radiotherapy*, Phys Med Biol, 44:185, 1999.

[272] Lujan A E, Larsen E W, Balter J M and Ten Haken R K, *A method for incorporating organ motion due to breathing into 3D dose calculations*, Med Phys, 26(5):715, 1999.

[273] The HDF Group, *Hierarchical data format version 5, 2000-2010*, `http://www.hdfgroup.org/HDF5`, last accessed: 4 November 2013.

[274] Boon S N, van Luijk P, Schippers J M, Meertens H, Denis J M, Vynckier S, Medin J et al., *Fast 2D phantom dosimetry for scanning proton beams*, Med Phys, 25(4):464, 1998.

[275] Boon S N, van Luijk P, Böhringer T, Coray A, Lomax A J, Pedroni E, Schaffner B et al., *Performance of a fluorescent screen and CCD camera as a two dimensional dosimetry system for dynamic treatment techniques*, Med Phys, 27(10):2198, 2000.

[276] Mansuy C, Dujardin C, Mahiou R and Nedelec J M, *Characterization and scintillation properties of sol-gel derived Lu2SiO5:Ln3+ (Ln=Ce, Eu and Tb) powders*, Opt Mater, 31(9):1334, 2009.

[277] Shepherd J A, Tecotzky M, Gruner S M and Tate M W, *Study of afterglow in x-ray phosphors for use on fast-framing charge-coupled device detectors*, Opt Eng, 36(11):3212, 1997.

[278] Safai S, Lin S and Pedroni E, *Development of an inorganic scintillating mixture for proton beam verification dosimetry*, Phys Med Biol, 49:4637, 2004.

[279] Karger C P, Jäkel O, Palmans H and Kanai T, *Dosimetry for ion beam radiotherapy*, Phys Med Biol, 55(21):R193, 2010.

[280] Birks J B, *The theory and practice of scintillation counting*, Oxford: Pergamon Press, 1967.

[281] Kerr D A, *Derivation of the Cosine Fourth Law for Falloff of Illuminance Across a Camera Image*, `http://dougkerr.net/Pumpkin/articles/Cosine_Fourth_Falloff.pdf`, last accessed: 4 November 2013.

[282] Partridge M, Evans P M and Symonds-Tayler J R N, *Optical scattering in camera-based electronic portal imaging*, Phys Med Biol, 44(10):2381, 1999.

[283] Schätti A, Žákova M, Meer D and Lomax A J, *Experimental verification of motion mitigation of discrete proton spot scanning by re-scanning*, Phys Med Biol, 58:8555, 2013.

[284] Bernatowicz K, Lomax A J and Knopf A, *Comparative study of layered and volumetric re-scanning for different scanning speeds of proton beams in liver patients*, Phys Med Biol, 58(22):7905, 2013.

[285] Richter D, Schwarzkopf A, Trautmann J, Krämer M, Durante M, Jäkel O and Bert C, *Upgrade and benchmarking of a 4D treatment planning system for scanned ion beam therapy*, Med Phys, 40(5):051722, 2013.

[286] von Siebenthal M, Szekely G, Gamper U, Boesiger P, Lomax A and Cattin P, *4D MR imaging of respiratory organ motion and its variability*, Phys Med Biol, 52:1547, 2007.

[287] Boye D, Lomax T and Knopf A, *Mapping motion from 4D-MRI to 3D-CT for use in 4D dose calculations: A technical feasibility study*, Med Phys, 40(6):061702, 2013.

[288] Graeff C, Durante M and Bert C, *Motion mitigation in intensity modulated particle therapy by internal target volumes covering range changes*, Med Phys, 39(10):6004, 2012.

[289] Knopf A, Parodi K, Paganetti H, Bortfeld T, Daartz J, Engelsman M, Liebsch N et al., *Accuracy of Proton Beam Range Verification Using Post-Treatment Positron Emission Tomography/Computed Tomography as Function of Treatment Site*, Int J Rad Oncol Biol Phys, 79(1):297, 2011.

[290] Luescher F, *Effiziente parallele Dosisberechnung in Scala*, 2013, Bachelor thesis, School of Engineering, University of Applied Sciences Northwestern Switzerland.

[291] Rutar G, *Optimal spot grid and energy steps on Gantry 2*, 2012, Semester project within Master of Science in Physics, ETH Zürich, Switzerland.

[292] Goitein M, Chen G T Y, Ting J Y, Schneider R J and Sisterson J M, *Measurements and calculations of the influence of thin inhomogeneities on charged particle beams*, Med Phys, 5(4):265, 1978.

[293] Goitein M and Sisterson J M, *The Influence of Thick Inhomogeneities on Charged Particle Beams*, Radiat Res, 74(2):217, 1978.

[294] Knopf A, Bert C, Heath E, Nill S, Kraus K, Richter D, Hug E et al., *Special Report: Workshop on 4D-treatment planning in actively scanned particle therapy requirements and preliminary recommendations*, Med Phys, 37(9):4608, 2010.

[295] Tiefenauer R F, Parkel T C, Follonier S and Meyer E, *Dynamic Anatomical Respiring Humanoid Thorax Phantom for Proton Therapy Assessment*, 2012, Project work within Master of Science in Nanosciences, University of Basel, Switzerland.

[296] Zhang Y, Knopf A C, Tanner C, Boye D and Lomax A J, *Deformable motion reconstruction for scanned proton beam therapy using on-line x-ray imaging*, Accepted by Phys Med Biol, 2013.